

THE MECHANICS OF SUBDUCTION ZONE TREMOR AND TRANSIENT
SLIP IN JAPAN

A DISSERTATION

SUBMITTED TO THE DEPARTMENT OF GEOPHYSICS

AND THE COMMITTEE ON GRADUATE STUDIES

OF STANFORD UNIVERSITY

IN PARTIAL FULFILLMENT OF THE REQUIREMENTS FOR THE DEGREE OF

DOCTOR OF PHILOSOPHY

David R. Shelly

March 2007

UMI Number: 3253534

Copyright 2007 by
Shelly, David R.

All rights reserved.

INFORMATION TO USERS

The quality of this reproduction is dependent upon the quality of the copy submitted. Broken or indistinct print, colored or poor quality illustrations and photographs, print bleed-through, substandard margins, and improper alignment can adversely affect reproduction.

In the unlikely event that the author did not send a complete manuscript and there are missing pages, these will be noted. Also, if unauthorized copyright material had to be removed, a note will indicate the deletion.

UMI[®]

UMI Microform 3253534

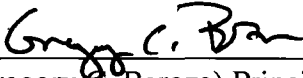
Copyright 2007 by ProQuest Information and Learning Company.

All rights reserved. This microform edition is protected against unauthorized copying under Title 17, United States Code.

ProQuest Information and Learning Company
300 North Zeeb Road
P.O. Box 1346
Ann Arbor, MI 48106-1346

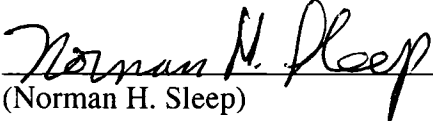
© Copyright by David R. Shelly 2007
All Rights Reserved

I certify that I have read this dissertation and that in my opinion it is fully adequate, in scope and quality, as dissertation for the degree of Doctor of Philosophy.



(Gregory C. Beroza) Principal Advisor

I certify that I have read this dissertation and that in my opinion it is fully adequate, in scope and quality, as dissertation for the degree of Doctor of Philosophy.



(Norman H. Sleep)

I certify that I have read this dissertation and that in my opinion it is fully adequate, in scope and quality, as dissertation for the degree of Doctor of Philosophy.



(Simon Klemperer)

Approved for the University Committee on Graduate Studies

ABSTRACT

Subduction zones produce a wide array of seismicity including the planet's largest earthquakes. Recently, modern geodetic instruments have illuminated transient slip events in subduction zones (and elsewhere) with durations ranging from days to years. These events appear to be relatively common on the portion of the plate interface downdip of the region that generates earthquakes. Such events are of particular interest because they likely increase the stress on the shallower more brittle portion of the fault and therefore could trigger a large earthquake. Although these slow events do not generate strong shaking, they are often accompanied by a weak semi-continuous seismic signal that has been termed non-volcanic tremor. A variety of mechanisms have been proposed to explain this tremor and its association with slow slip, often involving fluid flow. By utilizing seismic data from a dense borehole network in southwest Japan, I demonstrate that tremor is instead generated by a sequence of small shear failures on the plate interface. These failures likely occur under very low shear stresses and may be enabled by high pore fluid pressures interpreted to exist in this zone. Added together, these shear events form the semi-continuous tremor signal, usually during much larger-scale slow slip events. In addition, I present precise locations of tremor, obtained using a matched filter technique with previously recorded "template events," which allow slip to be tracked with unprecedented resolution. These locations reveal a complex evolution of slow slip, with smaller, shorter duration subevents exhibiting along-dip migration rates of 20-150 km/hour in repeated rupture episodes over the several-day course of an event. Tremor may be generated primarily at plate interface heterogeneities that stick and slip while driven to repeated failure by slip on neighboring portions of the fault.

ACKNOWLEDGMENTS

Many people contributed to making the research described in this thesis a reality. Without the support of many colleagues and friends, I would not have made it nearly this far.

I would first like to thank my advisor, Greg Beroza, for his positive influence and support over the years. Greg has taught me a great deal about seismology; perhaps more importantly, he has shown me how to approach scientific problems in new and creative ways. I have been amazed by his commitment to his students' research, demonstrated, for example, by his willingness to read drafts of papers at midnight or 5am. Despite this insomnia, Greg's comments are, as a rule, clear and focused, prompting great improvement in the final document.

Besides Greg, Satoshi Ide, of the University of Tokyo, had the biggest impact on my research. Satoshi's assistance with the Japanese seismic data was essential to this project, and I thank him for many hours spent answering my data-related questions. His scientific insights also added greatly to the work presented here, especially work led by him calculating the mechanism of low-frequency earthquakes and proposing a new scaling law for slow earthquakes. In addition, Satoshi served as my host during my participation in the Summer Institutes in Japan program, cosponsored by the National Science Foundation (NSF) and the Japan Society for Promotion of Science (JSPS). As part of this program, I spent two months as a visitor at the University of Tokyo in the Department of Earth and Planetary Science. The time I spent in Japan was extremely productive scientifically. I also very much enjoyed interacting with students and postdocs at the University of Tokyo including Sho Nakamura, Ryosuke Ando, Takahiko Uchide, Takanori Matsuzawa, and Takuji Yamada.

At Stanford, I have benefited enormously from interactions with talented fellow students and postdocs. Many of these interactions have been with other members of the earthquake seismology group including Seok Goo Song, Shuo Ma, Justin Rubinstein, Eva Zanker, Xyoli Perez-Campos, and Anu Venkataraman. I have benefited equally from the varying perspectives of students outside the group, including Bill Curry, Adam Pidlisecky, and Emily Desmarais, to name a few.

I also thank the friends at Stanford who accompanied me on various outdoor adventures and helped me maintain perspective and balance during graduate school. Frequent partners in exploration of California and beyond included Dave Wynn, Amie Lucier, Adam Pidlisecky, James Irving, Joe Colgan, and fellow instructors with the Outdoor Education Program.

Most of all, I would like to thank my family, especially my mom, my dad, and my sister Suzanne. Their unwavering enthusiasm and support helped get me through school at all levels – from pre-school and kindergarten to my upcoming graduation from the 23rd grade. Although the tables have turned somewhat (I find myself now teaching them as much they teach me), my family remains a critical partner in my education.

TABLE OF CONTENTS

List of figures.....	ix
1. Introduction.....	1
References.....	5
2. High-resolution subduction zone seismicity and velocity structure beneath Ibaraki Prefecture, Japan	7
Abstract.....	7
Introduction.....	8
Data and Results.....	12
Discussion.....	24
High Vp and Vs above subducting Pacific plate.....	24
Interplate seismicity.....	24
High Vp/Vs near top of subducting slab and in the mantle wedge.....	25
Conclusions.....	27
Acknowledgments.....	27
References.....	28
3. Low-frequency earthquakes in Shikoku, Japan, and their relationship to episodic tremor and slip.....	33
Methods	49
Acknowledgements	51
References.....	51
4. Non-Volcanic Tremor and Low Frequency Earthquake Swarms.....	56
Methods	75
Acknowledgements	78
References.....	78
5. The complex evolution of transient slip derived from precise tremor locations in western Shikoku, Japan	81

Abstract.....	81
Introduction.....	82
Methods.....	84
Results and Discussion.....	85
Migration of tremor and slip:.....	89
Relationship to Very Low Frequency Earthquakes.....	91
Tidal Triggering of Tremor and Slip.....	92
Implications for the mechanics of tremor and slip.....	94
Conclusions.....	95
References.....	109

LIST OF FIGURES

<i>Number</i>	<i>Page</i>
Figure 2.1. Tectonic map of the region.	10
Figure 2.2. Map of events and seismic stations used in this study	11
Figure 2.3. Characteristics of cross-correlation measurements as a function of event-pair separation distance.	14
Figure 2.4. Checkerboard test.....	16
Figure 2.5. Restoring resolution test.....	17
Figure 2.6. Comparison of catalog-determined and relocated hypocenters shown in map view and three different cross-sections	19
Figure 2.7. Close up view of plate interface events including focal mechanisms.....	20
Figure 2.8. Velocity inversion results	22
Figure 3.1. Comparison of temporal distribution of tremor activity and low- frequency earthquakes (LFEs) in western Shikoku.....	36
Figure 3.2. An extended period of tremor containing four identified LFEs.	38
Figure 3.3. Area map with events, stations, and velocity nodes used in the inversion.....	40
Figure 3.4. <i>S</i> -wave alignment for 172 correlated LFEs recorded at NIED Hi-net station N.KWBH, north component.	41
Figure 3.5. <i>P</i> -wave alignment for 70 correlated LFEs recorded at NIED Hi-net station N.KWBH, vertical component.....	42
Figure 3.6. An example of the correlation of a LFE with 45 regular earthquakes recorded at NIED Hi-net station N.KWBH, vertical component.....	43
Figure 3.7. Seismic velocities and relocated hypocenters along cross-section A-A'	45
Figure 4.1. Comparison of LFE, slow slip event, and megathrust earthquake mechanisms.	58
Figure 4.2. Comparison of Earthquake/LFE/Tremor Spectra.	59

Figure 4.3. Example of a detected LFE.....	61
Figure 4.4. Correlation sum functions and detection examples for two template LFEs during two tremor episodes.....	65
Figure 4.5. Synthetic test of LFE detection capability in the presence of noise and other events.	67
Figure 4.6. Detection of low-frequency earthquake swarms forming tremor.....	71
Figure 4.7. Animation showing detected events with time during non-volcanic tremor for the hour beginning September 2, 2005 at 19:00 (see enclosed CD for movie in Quicktime format).	72
Figure 4.8. Same as Supplementary Movie 1 but for the hour beginning August 29, 2005 at 17:00 (see enclosed CD for movie in Quicktime format).	73
Figure 5.1. Tectonic setting and location of study area.	86
Figure 5.2. The April 2006 tremor and slip event	88
Figures 5.3-5.16. Space-time progression of tremor during January 15-21, 2006 (5.3-5.9) and April 15-21, 2006 (5.10-5.16)	97
Figure 5.17. Animation showing detected events with time during non-volcanic tremor for 7 days, January 15-21, 2006 (see enclosed CD for movie in Quicktime format).	105
Figure 5.18. Same as Figure 5.17 but for April 15-21, 2006 (see enclosed CD for movie in Quicktime format).....	106
Figure 5.19. Evidence for tidal triggering of LFE activity.....	107
Figure 5.20. Histograms of LFE numbers versus phase angle, assuming a period of 12.4 hours (the average tidal period).	108

1. INTRODUCTION

Subduction zones, formed where two tectonic plates converge, are responsible for the bulk of the seismic energy released worldwide. Recently, episodic transient slip events have been discovered in subduction zones and elsewhere. Because these slip events happen much more slowly than regular earthquakes, they do not generate the strong shaking. However, such events are often associated with a weak semi-continuous seismic signal that has been termed non-volcanic tremor [Obara, 2002].

Although the association between slow slip downdip of the main seismogenic zone and tremor was recognized in both the Cascadia [Rogers and Dragert, 2003] and southwest Japan subduction zones [Obara et al., 2004], the exact relationship between these phenomena has remained unclear. Perhaps in analogy with volcanic tremor, which is thought to be generated by the movement of volcanic fluids, several authors proposed that the flow of fluids liberated from the subducting slab might be generating non-volcanic tremor.

In this thesis, I begin by examining subduction seismicity and velocity structure in northern Japan in Chapter 2. I then focus on non-volcanic tremor and episodic slow slip associated with subduction in southwest Japan in Chapters 3-5.

The second chapter uses the double difference tomography method in combination with waveform cross-correlation derived difference times to obtain high-precision hypocenter locations and a high-resolution tomographic image of the subduction zone at the complex intersection of three tectonic plates north of Tokyo, Japan [Shelly et al., 2006a]. Here I find a high Poisson's ratio within the subducting crust, which I interpret as evidence for high fluid pressure within this region, likely as a result of dehydration reactions taking place as the slab subducts and is subjected to increasingly high temperatures and pressures. The precise relocations allow me to distinguish between interplate and intraplate seismicity, highlighting the presence of interplate

seismicity down to 60 km depth. I hypothesize that this area may remain seismic to this depth in part because of a cooling influence from the unusual presence of a second subducting plate at this location. In order to most naturally account for the presence of the subducting slab and the most likely orientation of structure associated with this feature, I regularized the tomographic problem using a spatially variable method that applies the strongest regularization constraint along the dip of the slab, where it is present.

In chapter 3, I examine non-volcanic tremor beneath western Shikoku in southwest Japan [Shelly et al., 2006b]. Non-volcanic tremor was discovered in this area and subsequently found to correlate with slow slip events modeled to occur on the plate interface downdip of the main seismogenic zone. However, the mechanism of tremor and its exact relationship to slow slip remained unclear. One obstacle to understanding the phenomenon was that tremor locations were poorly constrained, especially in depth. Some portions of this tremor that are relatively strong and isolated have identifiable S-waves and occasionally also have P-wave observations. Such events are routinely included in the seismic event catalog, labeled as low-frequency earthquakes (LFEs). The catalog locations for these events, however, are relatively poorly constrained, especially in depth, due to the scarcity of P-wave observations and a difficulty in determining the exact S-wave onset time given the relatively low signal-to-noise ratios. I addressed both of these problems in this study. First, because the waveforms of different LFEs were found to be very similar, I could precisely measure the differential arrival times using cross-correlation of the waveforms. Secondly, even when no P-wave arrival time was given in the catalog, I was in many cases successful in determining a differential P-wave arrival time by cross-correlation. To do this, I cross-correlated waveforms in a window surrounding the theoretical P-wave arrival time, determined based on the S-wave arrival time and the estimated origin time. Using these cross-correlation measurements with the double-difference technique, I was able to obtain very precise locations for the LFEs and regular earthquakes, and the first LFE locations that were well constrained in depth. I found that the LFEs located

on a plane dipping with the expected dip of the plate interface. Therefore, I hypothesized that the LFEs occurred on the plate interface, coincident with the observed slow slip, and that LFEs therefore were probably generated by shear slip as part of the larger-scale slow slip event, rather than by fluid flow as previously proposed.

In chapter 4, I investigate the relationship between LFEs and tremor as a whole [Shelly et al., 2007]. First, I compare spectra of LFEs, tremor, and regular earthquakes. I find that the spectral shapes of LFEs and tremor are very similar, while clearly distinct from regular earthquakes. This indicates that the source processes of LFEs are probably the same as the rest of tremor, and prompted me to search for additional events similar to the previously recorded LFEs within continuous tremor. To do this, I utilized the waveforms of 677 LFEs that I located as part of the study presented in chapter 3. Using a matched filter technique with each LFE “template event” across all available stations simultaneously, I find a nearly continuous sequence of LFE detections during tremor. In other words, tremor is just the superposition of a swarm of individual LFEs. Additionally, this technique allows me to obtain precise locations of tremor with excellent temporal resolution. A study by Ide et al. [2007] examining stacked waveforms of LFEs further supports a plate-interface shear slip mechanism. In this study, mechanisms determined independently by P-wave first motions and an empirical moment tensor inversion using S-waves are both consistent with shear slip in the plate convergence direction. Combining these results, we can conclude that tremor itself is generated by shear slip on the plate interface and therefore tremor is a direct consequence of slow slip.

The implications of this result are profound. While we have recently begun to be able to monitor slow slip by surface-based geodetic measurements (such as GPS), these measurements do not constrain the temporal or spatial details of small slips at depth. However, combining this ability to precisely locate tremor with the new understanding of tremor as a direct signal of shear slip, we can begin to examine the details of how slow slip evolves, as I do in Chapter 5. Here, I find that contrary to common

assumption, slow slip does not evolve smoothly, but rather contains of a number of smaller-scale, shorter-duration subevents. Although slow slip has been seen to migrate along-strike at velocities around 10 km/day, I find instances of much more rapid migration along-dip at velocities of approximately 25-150 km/hr. I hypothesize that these regions of fast migration may be exhibiting stick slip behavior, driven to repeated failure by slip on surrounding portions of the fault.

Slip on this portion of the fault may increase stresses updip where large earthquakes occur; therefore, it is extremely important to monitor this slow slip. In the near future, the details of slow slip revealed by precise locations of tremor may contribute to a more accurate time-dependent seismic hazard evaluation.

Besides the fact that all chapters examine subduction in Japan, another unifying theme through this thesis is the use of cross-correlations between seismic waveforms. In particular, I employ the cross-correlation coefficient, which is a normalized measure of the level of correlation between two signals. The correlation coefficient ranges from -1 to 1 , and, for vectors x and y of length N is defined as

$$\frac{\sum_{i=1}^N [(x_i - \langle x \rangle)(y_i - \langle y \rangle)]}{\sqrt{\sum_{i=1}^N (x_i - \langle x \rangle)^2 \sum_{i=1}^N (y_i - \langle y \rangle)^2}},$$

where $\langle x \rangle$ and $\langle y \rangle$ are the expected values of x and y , respectively. In chapters 2 and 3, I use cross-correlation to determine very precise differential arrival times for different earthquakes at individual stations. By aligning waveforms based on the maximum correlation coefficient between them, I obtain very precise measurements of the differential arrival times of P and S-waves for events with similar waveforms. Waveforms tend to be most similar for nearby events with similar mechanisms; however, I have found that quality correlation-based differential time measurements can sometimes be made for events separated by up to 50 km and with a variety of source mechanisms. Besides using the maximum correlation to align waveforms, the

value of the correlation coefficient is also used to assess the quality of the data, which is then used to control the relative weighting each of these measurements receives during the inversion process. Chapters 4 and 5 utilize cross-correlation in a different context, in a matched filter technique for the problem of event detection. Here, similarity between the data stream and a known signal is measured by the sum of the correlation coefficients across all available channels of data.

Two related studies not included in this thesis were led by Dr. Satoshi Ide. These include the determination of low-frequency earthquake mechanisms [Ide et al., 2007a] and the proposal of a new scaling law unifying tremor/LFEs, very low frequency earthquakes, and slow slip events into a family of constant moment rate, shear slip events [Ide et al., 2007b].

REFERENCES

- Ide, S., D. R. Shelly, and G. C. Beroza (2007a), Mechanism of deep low frequency earthquakes: Further evidence that deep non-volcanic tremor is generated by shear slip on the plate interface, *Geophys. Res. Lett.*, 34, L03308, doi:10.1029/2006GL028890.
- Ide, S., G. C. Beroza, D. R. Shelly, and T. Uchide (2007b), A new scaling law for slow earthquakes, *Nature*, submitted.
- Obara, K. (2002) Nonvolcanic deep tremor associated with subduction in southwest Japan. *Science*, **296**, 1679.
- Obara, K., Hirose, H., Yamamizu, F. & Kasahara, K. (2004), Episodic slow slip events accompanied by non-volcanic tremors in southwest Japan subduction zone. *Geophys. Res. Lett.* **31**, doi:10.1029/2004GL020848.
- Rogers, G. & Dragert, H. (2003). Episodic tremor and slip on the Cascadia subduction zone: The chatter of silent slip. *Science* 300, 1942-1943.

Shelly, D. R., G. C. Beroza, H. Zhang, C. H. Thurber, S. Ide, and A. Hasegawa (2006a), High Resolution Subduction Zone Seismicity and Velocity Structure beneath Ibaraki, Japan, *J. Geophys. Res.*

Shelly, D. R., G. C. Beroza, S. Ide, and S. Nakamura (2006b), Low-frequency earthquakes in Shikoku, Japan and their relationship to episodic tremor and slip. *Nature* 442, 188-191.

Shelly, D. R., G. C. Beroza, and S. Ide (2007), Non-Volcanic Tremor and Low Frequency Earthquake Swarms, *Nature*, in press.

2. HIGH-RESOLUTION SUBDUCTION ZONE SEISMICITY AND VELOCITY STRUCTURE BENEATH IBARAKI PREFECTURE, JAPAN

ABSTRACT

We use double-difference tomography and waveform-derived cross-correlation differential times to estimate earthquake locations and P - and S -wave velocity structure in the subduction zone under Ibaraki and neighboring prefectures of north-central Honshu. We find evidence in both earthquake hypocenters and the velocity structure that the Philippine Sea plate, or perhaps a microplate fragment, may be caught between the subducting Pacific plate and overriding Okhotsk plate in this region. In the southern part of the study area, we find a zone of interplate events extending as deep as 60 km, forming a distinct lineation in cross-section. Focal mechanisms support the interpretation that these are low angle, subduction interface events. We infer that these events probably occur on the interface between the Pacific and Philippine Sea plates rather than between the Pacific and Okhotsk plates. In the upper part of the downgoing Pacific plate, we find a zone of high V_p/V_s ratio (~ 1.95), which may be explained by high pore-fluid pressures within the subducting crust. At a depth of 60-80 km, this region of high V_p/V_s appears to diffuse into the overlying mantle wedge, possibly indicating the upward release of fluids from the slab.

The material in this chapter has appeared in Shelly, D. R., G. C. Beroza, H. Zhang, C. H. Thurber, and S. Ide (2006), *J. Geophys. Res.*, 111, B06311, doi:10.1029/2005JB004081.

INTRODUCTION

Ibaraki Prefecture of north-central Honshu, Japan, lies in an area of complex tectonics, near the intersection of four tectonic plates. In northeastern Japan, the Pacific plate, an old and cold oceanic plate, is subducting beneath the Okhotsk plate (a fragment of the North American plate) at a rate of about 8-9 cm/yr to the west-northwest [Bird, 2003] (see Figure 2.1). To the south, the younger Philippine Sea plate is subducting beneath the Amur plate at a velocity of about 4.5 cm/yr to the northwest. The Philippine Sea plate also subducts beneath the Okhotsk plate to the north, along their short, common boundary, while the Pacific plate in turn subducts beneath both tectonic plates. Thus, within a zone just south of our study region, the Philippine Sea plate is known to be sandwiched between the subducting Pacific Plate and the overriding Okhotsk plate. Alternatively, *Toda et al.* [2005] have proposed the existence of a separate microplate in this region, which they interpret as a dislodged block of the Pacific plate.

For simplicity, we refer to our study area as the Ibaraki region; however besides the Ibaraki prefecture, our study area also encompasses parts of the Tochigi and Fukushima prefectures to the north and west (Figure 2.2). The seismicity in the Ibaraki region includes shallow crustal earthquakes, interplate thrusting events on the subduction interface, and a prominent double seismic zone of intermediate-depth earthquakes. Events in the double seismic zone are believed to rupture within the subducting plate, with the upper plane events occurring primarily within the subducting crust [Igarishi et al., 2001]. Nearly parallel and about 30 km deeper, a second plane of earthquakes is found within the subducting mantle lithosphere [Hasegawa et al., 1978]. Recent studies [i.e. Hacker et al., 2003] support the hypothesis that these intraplate events are enabled by the process of dehydration embrittlement [Kirby, 1995]. According to this hypothesis, as the plate subducts, increasing pressures and temperatures result in metamorphic reactions within the slab.

If the slab initially contains hydrous minerals, water may be released as a product of the metamorphic reaction, thus raising the pore-fluid pressure and reducing the effective normal stress, enabling brittle failure [Kirby, 1995]. While the precise mechanisms are still a matter of debate, the upper plane of seismicity may correspond to the dehydration of metabasalt and metagabbro during their transformation to eclogite, while serpentine dehydration has been proposed to enable the lower plane of seismicity [Peacock, 2001; Hacker *et al.*, 2003].

We examine the subduction zone beneath the Ibaraki region using a combination of double-difference tomography [Zhang and Thurber, 2003] and differential times determined by waveform cross-correlation. Double-difference tomography (tomoDD) extends the double-difference earthquake location technique (hypoDD) [Waldhauser and Ellsworth, 2000] to estimate earthquake locations and velocity structure. Like hypoDD, tomoDD uses differential times, calculated either from catalog phase picks or by cross-correlation of waveforms. TomoDD also includes absolute arrival time measurements. The combination of precise earthquake hypocenters and differential time measurements allows determination of higher resolution velocity-structure in the near-source region compared to that possible with conventional tomographic techniques (see Zhang and Thurber [2006] for a detailed analysis of the double-difference technique). Earthquake locations should improve compared with hypoDD (particularly the absolute locations) due to the estimation of 3D velocity structure and the inclusion of absolute travel times. In our analysis we use differential times calculated from catalog phase picks as well as those calculated by waveform cross-correlation. Cross-correlation measurements provide a set of very low noise measurements, since for similar waveforms the cross-correlation technique greatly reduces errors inherent in the arrival time picking process [e.g., Schaff *et al.*, 2004]. The need for waveform similarity, however, restricts the scale-length across which differential time measurements can be made using cross-correlation. Thus, cross-correlation measurements are most valuable for resolving short scale-length velocity structure and relative locations of closely spaced earthquakes.

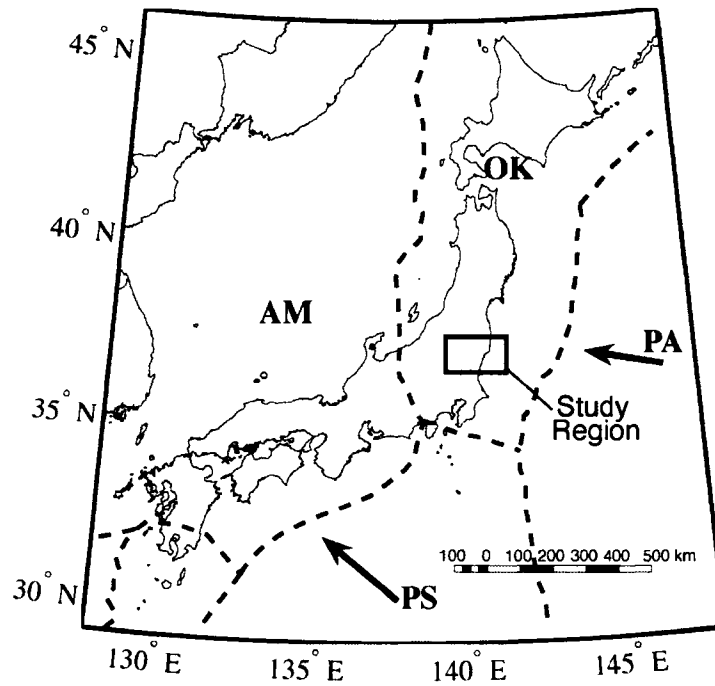


Figure 2.1. Tectonic map of the region. Dashed lines indicate plate boundaries. PA=Pacific plate, PS=Philippine Sea plate, OK=Okhotsk plate, AM=Amur plate. Plate model is PB2002 from Bird [2003].

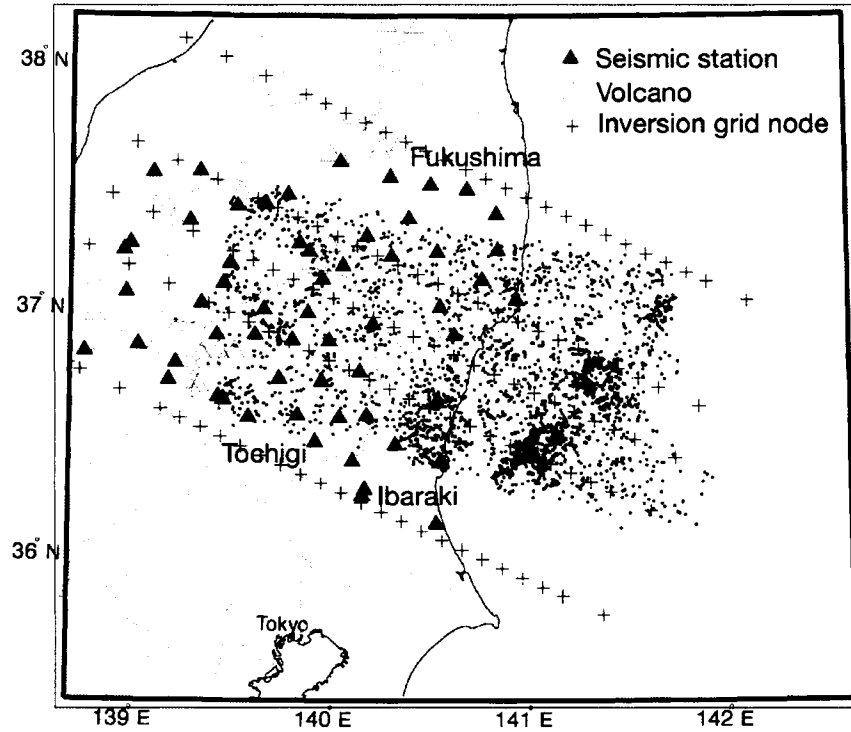


Figure 2.2. Map of events and seismic stations used in this study. Small dots indicate earthquakes, filled triangles represent seismic stations, open triangles denote volcanoes active in the Quaternary, and pluses show the locations of our velocity inversion nodes. Gray lines show prefectural boundaries with the prefectures in our central study area labeled.

DATA AND RESULTS

We relocate 3513 earthquakes, occurring between June 2002 and September 2003 in the Ibaraki region, with catalog locations between 36 and 37.5 degrees north latitude and 139.5 and 141.75 degrees east longitude as shown in Figure 2.2. We include all catalog events located deeper than 50 km. Due the high density of shallow events and in order to make the problem more computationally tractable, we select every third event (in time) for those shallower than 50 km. We use waveform data at 60 stations maintained by NIED, Japan Meteorological Agency (JMA), University of Tokyo, and Tohoku University. Of these stations, 34 are from the NIED Hi-net high-sensitivity borehole network [Obara, 2005]. Waveform cross-correlation measurements yield 1.1 million differential times (63% of which are *S*-wave measurements). We also use approximately 87,000 absolute arrival times (52% *S*) from the JMA catalog for these same stations. From these data we derive 4.4 million catalog differential times (53% *S*).

Because there are strong velocity variations in subduction zones, and because we are interested in resolving this velocity structure, we do not limit ourselves to closely spaced event-pairs as is commonly done to reduce velocity model dependence in double-difference earthquake relocation. Instead, we allow catalog differential times for some event-pairs up to 75 km apart and attempt cross-correlations for event separations of up to 50 km. This provides a large number of cross-slab differential times between the upper and lower limbs of the double seismic zone, giving us enhanced sensitivity to the internal velocity structure of the slab. For the cross-correlation measurements, we accept a differential time if the sum of the maximum cross-correlation coefficient and the mean coherence is greater than 1.30. Although we attempt correlations for event pairs up to 50 km apart (maximum horizontal separation 20 km), the number of successful correlations decreases with distance. Figure 2.3 shows histograms of the number of successful correlations versus event pair separation distance for *P*-waves (3a) and *S*-waves (3b). The greatest decrease occurs

from 0 to 5 km event separation. *S*-wave correlations exhibit a slightly sharper decline with increasing separation distance than do *P*-waves. Post-fit residuals for cross-correlation-based differential time measurements increase with separation distance (Figure 2.3, parts c and d), but this increase levels off at larger distances. The residuals remain relatively low, indicating that these data represent precise differential time measurements. The fitting of these differential times still allows the fitting of the absolute arrival times, as the mean of the magnitude of the absolute-time residuals decreases from 0.76 s to 0.18 s over the course of the inversion. Spatially, events along the subduction interface are more highly correlated than events within the subducting slab. This characteristic is likely due both to the higher density of events on the plate interface, as well as more consistent mechanisms for these events. Since intraplate events do not occur along a single fault, their source mechanisms are likely more diverse than interplate events.

In addition to the hypocentral relocations, we simultaneously solve for the *P*- and *S*-wave velocity structure at each grid node. In the central portion of our model we use a node spacing of 5 km vertically, 10 km horizontally along subduction dip, and 24 km horizontally along subduction strike. Velocities are interpolated linearly between grid nodes. The horizontal spacing of grid nodes is shown in Figure 2.2. Although our starting model contains a region of higher velocity where we expect the slab, tests performed using a simple 1-D starting model produce similar results.

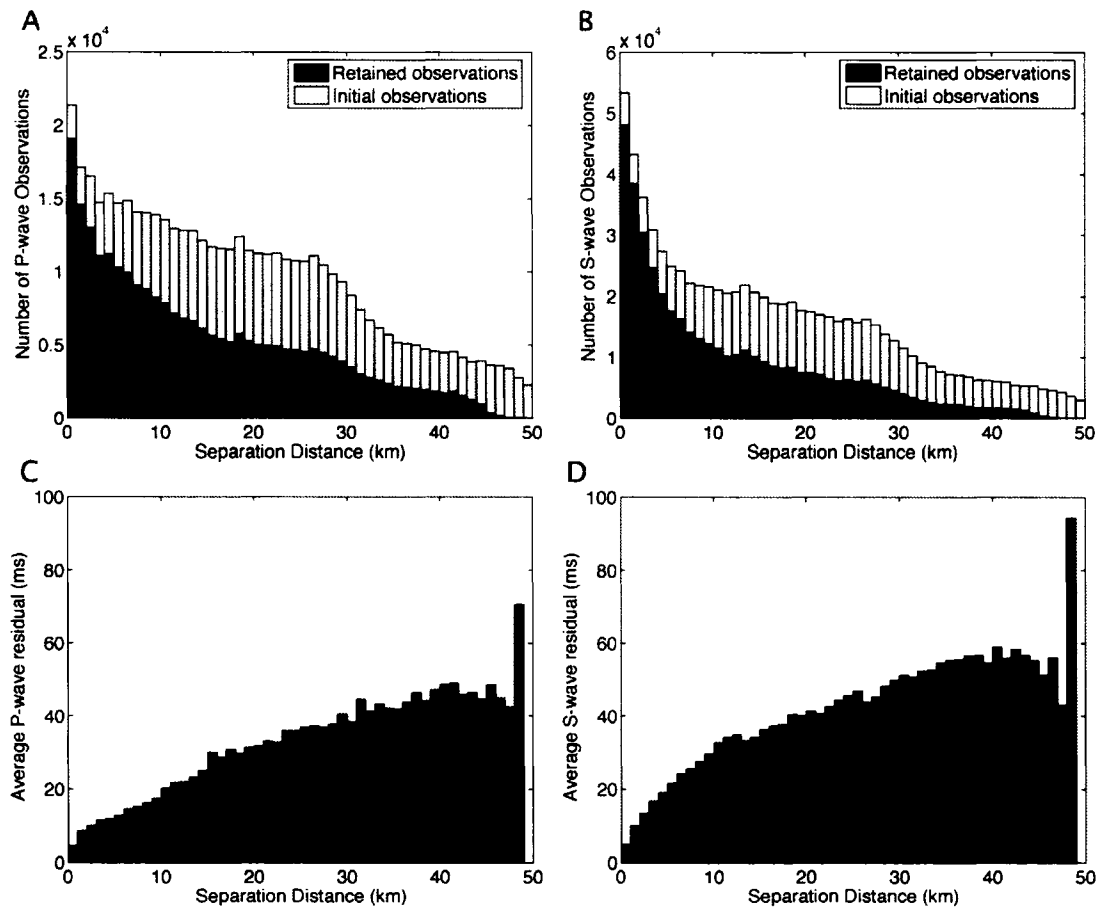


Figure 2.3 Characteristics of cross-correlation measurements as a function of event-pair separation distance. Parts (a) and (b) show the numbers of successful cross-correlations for *P*- and *S*-waves respectively, plotted in light gray. A successful correlation is defined as one where the sum of the maximum cross-correlation coefficient and mean coherence exceeds 1.30. Plotted in dark gray are the numbers of these measurements retained at the end of the inversion, after outliers have been removed. Parts (c) and (d) show the average residuals for these retained measurements as a function of separation distance for *P*- and *S*-wave correlations, respectively. The sharp peak in residuals near 49 km separation is due to the very small number of retained observations being averaged at this distance.

To optimize our model for the expected geological structure, we regularize the inverse problem using two different approaches. Since we anticipate the smallest variations in velocity along the dip of the slab, where it is present, and horizontally elsewhere, we can adapt our regularization to accommodate this expectation explicitly [Clapp, 2001]. To accomplish this, we first divide our model into two regions. Everywhere including and below the Wadati-Benioff zone seismicity is considered “slab” while everywhere above this is considered “not slab”. The dashed lines in Figure 2.4 (parts C and D) indicate the boundary between these two regions. Within the “slab”, we perform the primary regularization along the average dip of the slab, by minimizing the difference between slowness at diagonally adjacent nodes. The grid is arranged so that this diagonal step corresponds to the dip angle of the slab. Elsewhere, our primary regularization is horizontal. In either case, we constrain the L2-norm of the first difference between slowness perturbations at adjacent nodes. Using this technique, we can select the model (from the many that fit the data acceptably well) that has general structure most consistent with our geologic expectations. In addition to our primary geologically motivated regularization, we also perform a low-weighted secondary regularization in each coordinate direction.

In order to achieve a “minimum feature” model containing only features strongly determined by the data, we apply a substantial smoothing constraint in our inversion. To examine the resolution of our inversion and the effects of this smoothing, we perform two types of resolution tests: 1) a checkerboard test, which tests the ability to recover a model with alternating blocks of high and low velocities (Figures 2.4c and 2.4d) and 2) a restoring resolution test [Zhao *et al.*, 1992], which tests the ability to recover the model estimated from the inversion of the real data (Figure 2.5). For each test, we calculate synthetic travel-time observations, including only those travel-times and differential times for which we actually have data. We then add noise based on the estimated uncertainty of the real data. In this case, we add uniformly distributed random noise in the interval $[-0.025s, 0.025s]$ for P -wave observations and $[-0.05s, 0.05s]$ for S -wave observations. Additionally, we add a station noise term from the

uniform distribution $[-0.05s, 0.05s]$ to each observation; this noise term is the same for every observation at a given station. Finally we invert these data using the same procedure as our actual inversion, including the spatially variable regularization.

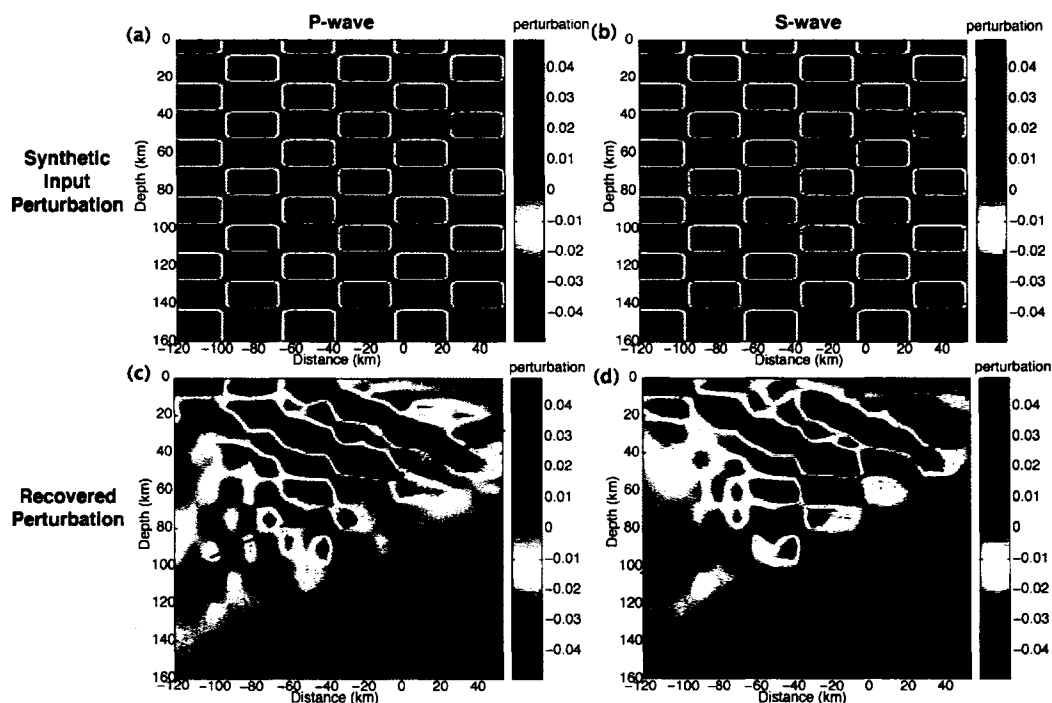


Figure 2.4 Checkerboard test. (a) The P -wave input velocity model, and (b) S -wave input velocity model for the checkerboard tests. Each consists of patches 15×30 km in dimension (3 nodes vertically and horizontally) with velocities $+5\%$ and -5% compared to the normal starting model. Parts (c) and (d) show the recovered P - and S -wave models, respectively, using the same parameters as the actual inversion. This test demonstrates that features of this spatial dimension and magnitude are well-resolved in the central part of the model, but not well resolved in the shallowest region offshore (where there are no seismic stations) and in the westernmost part of the slab and mantle wedge (where there are few crossing rays, especially for S -wave observations). The dashed lines in parts (c) and (d) indicate the boundary between the two different regularizations of our model.

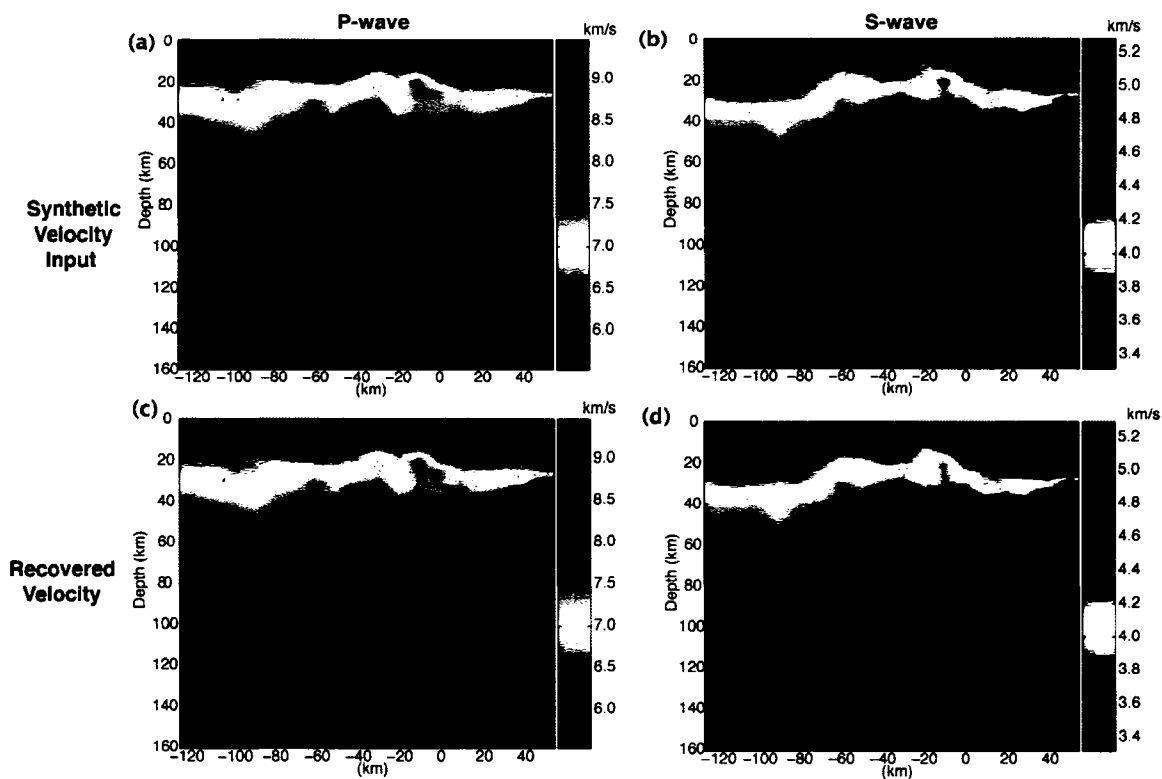


Figure 2.5. Restoring resolution test. Parts (a) and (b) show the input P - and S -wave velocity models, respectively. Parts (c) and (d) show the corresponding recovered velocity models. In this test, the input P - and S -wave models are well recovered in all parts of the model. The dashed lines indicate the boundary between the two different regularizations of our model.

The results of the checkerboard test are shown in Figures 2.4c and 2.4d. In this case, the large smoothing coefficient produces a model containing only features strongly determined by the data. With this constraint, *P*- and *S*-wave velocities are well resolved in the region between the lower limb of the double-seismic zone and the stations on land at the surface. We observe some smearing of velocities along the primary ray direction between the slab and stations on the surface to the west. One area not well resolved at this scale is the slab and mantle wedge west of -70 km where sparse seismicity and a lack of crossing rays hampers resolution, especially for *S*-wave structure. While the strong smoothing is sub-optimal for recovering the very oscillatory checkerboard pattern, it is much better suited to the recovery of a more geologically reasonable model. To demonstrate this, we perform the restoring resolution test, using the velocity structure obtained in the inversion of the real data as our synthetic model (Figure 2.5). In this case, the velocity structure recovered is almost identical to the input velocity structure.

A comparison of initial catalog locations and our relocations is shown in Figure 2.6 for each of three cross-sections. We see improved definition of the limbs of the double seismic zone when viewed in cross-section, as well as clear sharpening of many structures in map view. The most dramatic improvement in locations occurs with the events near the upper part of the slab between 35 and 60 km depth along cross-section C-C'. Figure 2.7 shows a zoom of the relocations in this area. At these depths, in the southernmost cross-section (C-C'), an area of intense seismicity appears diffuse in the catalog locations but collapses into a distinct and pronounced plane after relocation. We observe a dense cluster of seismicity from 35-45 km depth. Between 45 and 60 km depth the seismicity on this plane is less dense but still obvious. NIED CMT solution focal mechanisms, shown in Figure 2.7, support the interpretation that these are low angle, subduction-interface thrust events. As seen from the cross-sections shown in Figure 2.6, however, this well-defined plane is only present in the southern cross-section and the seismicity pattern farther north is somewhat more complex.

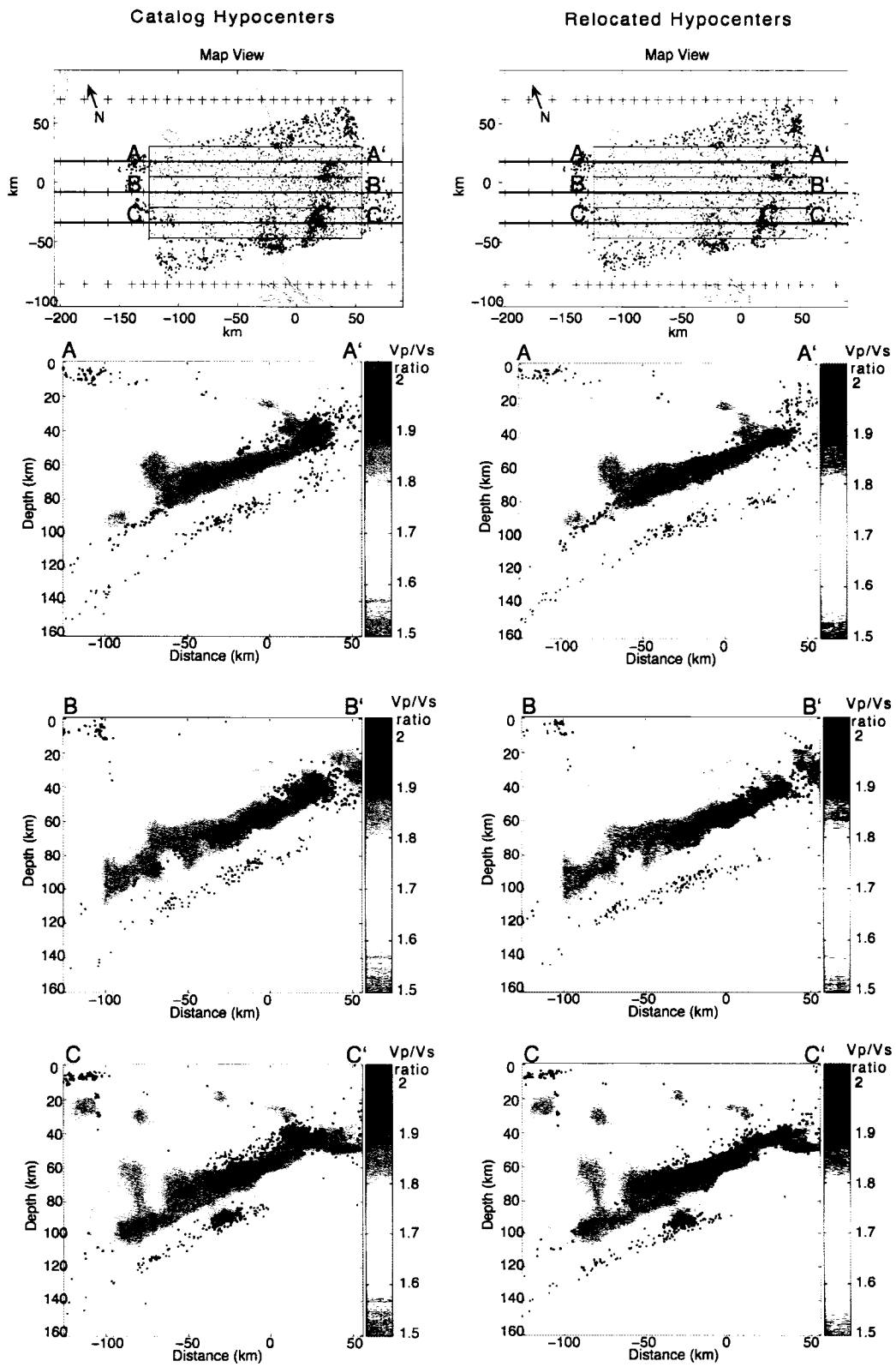


Figure 2.6. Comparison of catalog-determined (left column) and relocated hypocenters (right column) shown in map view (top) and three different cross-sections. Also plotted in the map view are the locations of velocity inversion nodes (red +) and the locations of cross-sections A-A', B-B', and C-C' (blue lines). Hypocenters shown in each cross-section are from the 24 km wide corridor along the cross-section as shown in map view. The V_p/V_s velocity structure corresponding to each cross-section is also shown for reference, but is faded to avoid obscuring hypocenters. The green outline in map view represents the coastline of Honshu.

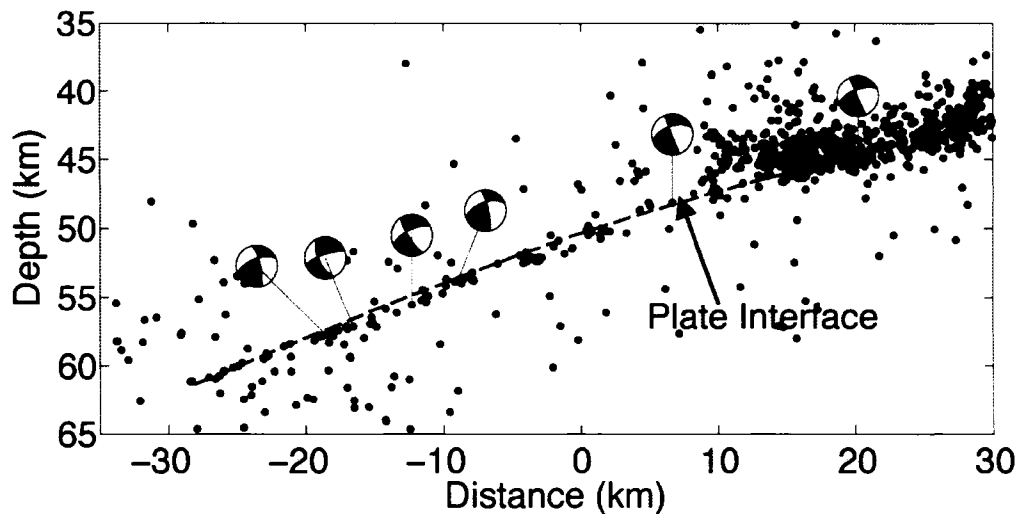


Figure 2.7. Close up view of plate interface events (cross-section C-C', Fig. 2.6), including focal mechanisms. NIED CMT solution focal mechanisms are plotted as a side view projected onto the cross-section. Locations and focal mechanisms are consistent with low-angle thrusting on the plate interface. The dashed line indicates the inferred location of the plate interface.

Figure 2.8 shows the P -wave, S -wave and V_p/V_s structures for cross-section C-C', along with all of the earthquake hypocenters used in the inversion. The faded areas indicate regions of poor resolution. We see a clear region of high V_p and V_s in the area of the downgoing slab. Although our initial velocity model includes a slab (initial $V_p=8.2$, $V_s=4.7$), high velocities are recovered in this region even when starting from a 1-D model. Velocities in the slab between the upper and lower limbs of seismicity are approximately $V_p=8.4$ km/s and $V_s=4.6$ km/s, with a V_p/V_s ratio of about 1.8. We also find region of high V_p and V_s above the subducting Pacific Plate, between 40 and 70 km depth and horizontal coordinate -70 and 0 . This feature is less pronounced in the north compared to the south where some seismicity can be seen corresponding to this region. The change in velocity is not merely a byproduct of variable resolution, as the resolution of this zone remains very good along the strike of the slab.

One of the most striking features of our velocity image is a region of very high V_p/V_s ratio (~ 1.95) in the upper part of the downgoing plate. This feature is most pronounced up to a depth of 70 km, where the region of high V_p/V_s ratio appears to begin to diffuse into the mantle wedge. In the slab below this depth, the V_p/V_s ratio decreases to about 1.85. This contrasts with a region of slightly lower than average V_p/V_s of ~ 1.7 associated with the lower limb of the double seismic zone, a feature that bears some similarity to that seen by *Zhang et al.* [2004] but is much less pronounced here.

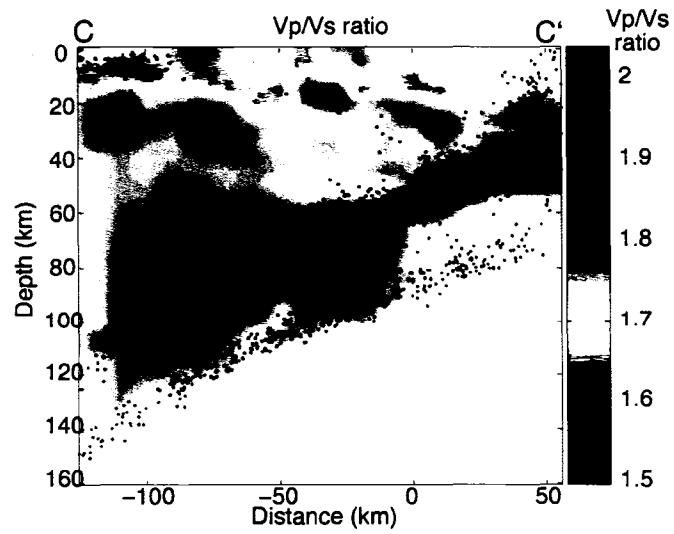
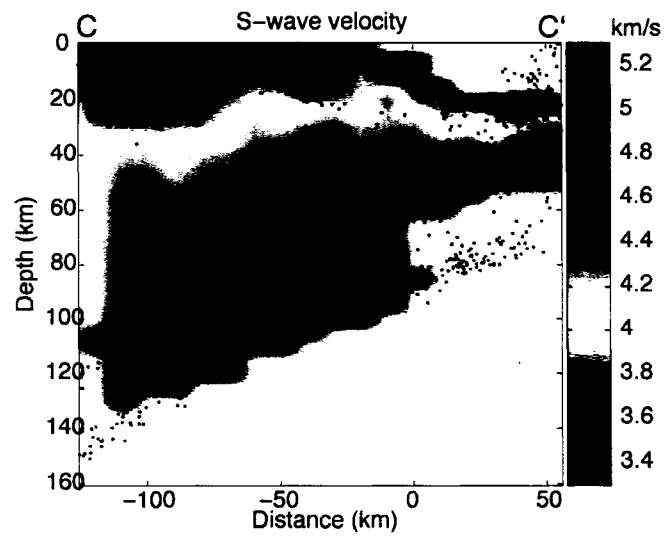
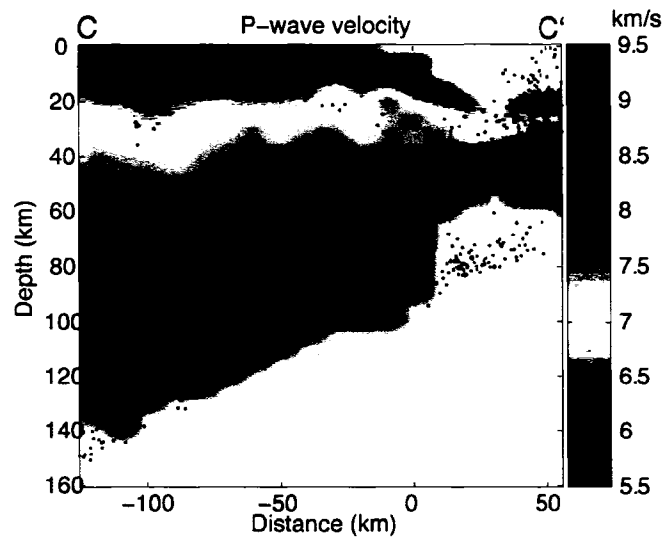


Figure 2.8. Velocity inversion results. Plots show P -wave velocities (top), S -wave velocities (middle), and V_p/V_s ratios (bottom), for cross-section C-C' (Figure 2.6). Relocated hypocenters for all earthquakes used in the inversion are also plotted. Faded areas represent zones of poor resolution, where the derivative weight sum (dws) value is less than 50.

DISCUSSION

HIGH V_p AND V_s ABOVE SUBDUCTING PACIFIC PLATE

As noted above, we find a region of high V_p and V_s above the subducting Pacific slab (Figure 2.8), which is most pronounced in the southern portion of our study area. Accompanying this feature is some anomalous-looking seismicity, occurring within what would normally be the mantle wedge. This seismicity can be seen around 55-65 km depth, between -40 and 10 km horizontal coordinate, a short distance above the subducting Pacific plate. Slightly to the south of our study area, similar seismicity has been interpreted as occurring within the Philippine Sea plate [Ohmi and Hurukawa, 1996; Sato *et al.*, 2005; Matsubara *et al.*, 2005]. This leads us to believe that this high V_p and V_s feature is actually the northern corner of the Philippine Sea Plate, sandwiched here between the Pacific Plate (below) and the Okhotsk plate (above). Alternatively, it could be a separate microplate fragment block dislodged from the Pacific slab, as proposed for this region by Toda [2005].

INTERPLATE SEISMICITY

The observed interplate events represent significantly deeper seismic coupling than the 37-43 km maximum depth reported for this area previously by Tichelaar and Ruff [1993], but they are consistent with the maximum depth of 50-70 km for low-angle thrust events found by Igarashi *et al.* [2001] farther to the north. Interestingly, the deepest interplate events are not extensive along subduction strike, but are limited to the southern portion of the study region. This, along with evidence for the presence of the Philippine Sea plate (or other microplate) above the slab, leads us to suggest that these events probably occur on the interface between the Pacific and Philippine Sea plates rather than between the Pacific and Okhotsk plates. We observe a distinct difference in the character of interplate seismicity between the southern 1/3 of the study region, which is continuously active to 60 km depth, and the northern 2/3, which

appears only sporadically active to about 50 km depth. This may indicate the northern boundary of the sandwiched plate. In the south, this third plate would cool the interface, possibly allowing seismic slip to persist to greater depths. These deeper interplate events may be a northern extension of what has been termed the Tsukuba-Chiba seismic belt [Ohmi and Hurukawa, 1996; Hurukawa and Imoto, 1990], a band of seismic activity extending in a north-south direction that consists of events believed to occur on the boundary of the Philippine Sea and Pacific plates.

HIGH V_p/V_s NEAR TOP OF SUBDUCTING SLAB AND IN THE MANTLE WEDGE

A region of high V_p/V_s can be located in the uppermost part of the subducting Pacific Plate by its position just beneath the interplate seismicity. This feature is robust in that it extends with large amplitude between 50 km and 70 km depth (-50 to 10 km horizontal coordinate) and is apparent in all three cross-sections of the region (Figure 2.4). Slightly to the south, Matsubara *et al.* [2005] imaged a similar region of high V_p/V_s within the upper part of the subducting Pacific slab, which was most pronounced between 70 and 90 km depth. An analogous area of high V_p/V_s has also been observed in the Nankai trough [Kodaira *et al.*, 2003], where it was interpreted to result from high pore-fluid pressures. In Cascadia, Bostock *et al.* [2002] and Nicholson *et al.* [2005] reported a comparable region of low S -wave velocities, based on scattered wave images. These authors interpret this zone as the subducting crust and associate it with the so-called E-reflection layer, whose location relative to the subducting slab has been a matter of significant debate. If the region we observe in Ibaraki is analogous, our work supports the conclusion that this feature in fact represents the subducting oceanic crust.

Below 70 km, the V_p/V_s ratio in the top of the slab decreases and we see a corresponding increase in V_p/V_s in the overlying mantle wedge to ~ 1.85 between 60 and 80 km depth (-90 to -50 km horizontal coordinate). This exchange of the high V_p/V_s region likely indicates water being released from the oceanic crust into the overlying mantle at this depth. It may be qualitatively similar to that seen in southern

Cascadia by *Bostock et al.* [2002] and *Brocher et al.* [2003], although the depth here is much greater than their observed depth of around 40 km. However, this discrepancy might be explained by a difference in thermal structures between the subduction zones. Subduction in northeast Japan is believed to occur under substantially cooler conditions than in Cascadia [*Hacker et al.*, 2003] because the Pacific plate is much older and is subducting more quickly than the Juan de Fuca plate in Cascadia. The possible presence of a third plate, whether the Philippine Sea or other microplate, sandwiched between the Okhotsk and Pacific plates, would act to lower temperatures further [*Iwamori*, 2000]. Therefore, similar processes may occur at greater depths in this region compared to Cascadia.

Bostock et al. [2002] as well as *Brocher et al.* [2003] interpreted the low *S*-wave velocities they image as serpentinization of the forearc wedge. In this case, we have evidence for the release of water from the slab crust, which in turn could allow serpentinization of the overlying mantle. *Christensen* [2004], however, argued that the observed V_p/V_s ratio of ~ 1.9 cannot be due to serpentinization alone since even pure antigorite (the form of serpentine stable under conditions of relatively high temperature and pressure) has a V_p/V_s ratio of only 1.85. He suggested high pore pressures and anisotropy in addition to serpentinization might be responsible for the high V_p/V_s ratio. Serpentine would generally be unstable at the temperatures and pressures at 70 km depth; however, as we argued above, the thermal structure of this area is likely to be much cooler than average. On the other hand, if the thermal effect of the Philippine Sea plate is limited and this zone is not sufficiently cool for serpentine stability, a small percentage of melt could also explain the observed V_p/V_s ratio. *Nakajima et al.* [2001] and *Zhang et al.* [2004] offered this interpretation for similar features they observed farther north. Recently active volcanoes located on the surface a short distance west of this feature might support this conclusion. As with the serpentine hypothesis, the release of water from the slab is key; in this case the water would lower the melting temperature in the mantle wedge sufficiently to allow the small percentage of melt.

CONCLUSIONS

Using waveform cross-correlation and double-difference tomography, we provide a detailed image of the seismicity and P - and S -wave velocity structure beneath the Ibaraki region that provides important constraints on the structure, petrology and fluid content of this subduction zone.

Precise hypocenter locations show three planes of seismicity in cross-section: a distinct plane of interplate events on the upper surface of the slab, a zone of intraplate events within the upper part of the slab, and a lower zone of intraplate events within the slab mantle. The nature of the interplate seismicity, however, varies considerably along strike; it is most active and extends deepest in the southern part but is shallower and more irregularly distributed to the north. A contributing factor to this difference may be the termination of the Philippine Sea plate above the downgoing Pacific slab and below the overriding Okhotsk plate in this region.

We observe a high V_p/V_s ratio of ~ 1.95 in the upper part of the downgoing slab between 50 and 70 km depth, which we interpret as evidence for high pore fluid pressures within the subducting slab crust of this region. Beginning around 70 km depth this zone appears to diffuse upward, likely related to water being released from the slab and migrating up into the overlying mantle wedge. A small percentage of melt or a combination of high pore-pressures and serpentinization may explain the observed high V_p/V_s ratio in the mantle wedge.

ACKNOWLEDGMENTS

We thank Kelin Wang, Toru Matsuzawa, and an anonymous reviewer for detailed and constructive comments that substantially improved this manuscript. This material is based upon work supported by the National Science Foundation grant Nos. EAR-

0409917 (Stanford) and EAR-0337495 (UW). All data were obtained from the NIED Hi-net data server.

REFERENCES

- Abers, G. A. (1996), Plate structure and the origin of double seismic zones, edited by G. Bebout, D. Scholl, and S. Kirby, in *Subduction Top to Bottom, Geophys. Monogr.*, vol. 96, edited by G. Bebout, D. Scholl, and S. Kirby, pp. 223-228, AGU, Washington, D.C.
- Bird, P. (2003), An updated digital model of plate boundaries, *Geochem. Geophys. Geosyst.*, 4(3), 1027, doi:10.1029/2001GC000252.
- Bostock, M. G., R. D. Hyndman, S. Rondenay, and S. M. Peacock (2002), An inverted continental Moho and serpentinization of the forearc mantle, *Nature*, 417, 536-538.
- Brocher, T.M., T. Parsons, A.M. Tréhu, C.M. Snelson, and M.A. Fisher (2003), Seismic evidence for widespread serpentinized forearc upper mantle along the Cascadia margin, *Geology*, 31, 267 - 270.
- Christensen, N.I. (1984), Pore pressure and oceanic crustal seismic structure, *Geophys. J. Roy. Astron. Soc.*, 79, 411.
- Christensen, N.I. (2004), Serpentinites, peridotites, and seismology, *International Geology Review*, 46, 795-816.
- Clapp, R.G. (2001), Geologically constrained migration velocity analysis, Ph.D. Thesis, Stanford University, Stanford, California.
- Hacker, B. R., S. M. Peacock, G. A. Abers, and S. D. Holloway (2003), Subduction Factory 2. Are intermediate-depth earthquakes in subducting slabs linked to

metamorphic dehydration reactions? *J. Geophys. Res.*, *108*, B1, 2030, doi: 10.1029/2001JB001129.

Hasegawa, A., N. Umino, and A. Takagi (1978), Double-planed deep seismic zone and upper-mantle structure in the northeastern Japan arc, *Geophys. J. Roy. Astron. Soc.*, *54*, 281-296.

Hurukawa, N. and M. Imoto (1990), Fine structure of an underground boundary between the Philippine Sea and Pacific plates beneath the Kanto district, Japan, *J. Seismol. Soc. Jpn., Ser. 2*, *43*: 413-429 (in Japanese with English abstract).

Igarashi, T., T. Matsuzawa, N. Umino, and A. Hasegawa (2001), Spatial distribution of focal mechanisms for interplate and intraplate earthquakes associated with the subducting Pacific plate beneath the northeastern Japan arc: a triple-planed deep seismic zone, *J. Geophys. Res.*, *106*, 2177-2191.

Iwamori, H. (2000), Deep subduction of H₂O and deflection of volcanic chain towards backarc near triple junction due to lower temperature, *Earth and Planetary Science Letters*, *181*, 41-46.

Kerrick, D.M. and J.A.D. Connolly (2001), Metamorphic devolatilization of subducted oceanic metabasalts: implications for seismicity, arc magmatism and volatile recycling, *Earth and Planetary Science Letters*, *189*, 19-29.

Kirby, S. (1995), Intraslab earthquakes and phase changes in subducting lithosphere, *Rev. Geophys., Suppl.*, 287-297.

Kirby, S.H., E.R. Engdahl, and R. Denlinger (1996), Intermediate-depth intraslab earthquakes and arc volcanism as physical expressions of crustal and uppermost mantle metamorphism in subducting slabs, in *Subduction Top to Bottom*, *Geophys. Monogr.*, vol. 96, edited by G. Bebout, D. Scholl, and S. Kirby, pp. 195-214, AGU, Washington, D.C.

- Kodaira, S., T. Iidaka, A. Kato, J. Park, T. Iwasaki, and Y. Kaneda (2003), High pore fluid pressure may cause silent slip in the Nankai Trough, *Science*, *304*, 1295-1298.
- Matsubara, M., H. Hayashi, K. Obara, and K. Kasahara (2005), Low-velocity oceanic crust at the top of the Philippine Sea and Pacific plates beneath the Kanto region, central Japan, imaged by seismic tomography, *J. Geophys. Res.*, *110*, doi:10.1029/2005JB003673.
- Matsuzawa, T., T. Kono, A. Hasegawa, and A. Takagi (1986), Upper mantle velocity structure estimated from *PS*-converted wave beneath the northeastern Japan arc, *Geophys. J. R. Astron. Soc.*, *86*, 767-787.
- Nakajima, J., T. Matsuzawa, A. Hasegawa, and D. Zhao (2001), Three-dimensional structure of V_p , V_s , and V_p/V_s beneath northeastern Japan: Implications for arc magmatism and fluids, *J. Geophys. Res.*, *106*, 21843-21857.
- Nicholson, T., M. Bostock, and J.F. Cassidy (2005), New constraints on subduction zone structure in northern Cascadia, *Geophys. J. Int.*, *161*, 849-859, doi: 10.1111/j.1365-246X.2005.02605.x.
- Obara, K., K. Kasahara, S. Hori and Y. Okada, (2005), A densely distributed high-sensitivity seismograph network in Japan: Hi-net by National Research Institute for Earth Science and Disaster Prevention, *Review of Scientific Instruments*, *76*, 021301-doi:10.1063/1.1854197.
- Ohmi, S. and N. Hasegawa (1996), Detection of the subducting crust of oceanic plates beneath the Kanto district, Japan, *Tectonophysics*, *261*, 249-276.
- Peacock, S. (2001), Are the lower planes of double seismic zones caused by serpentine dehydration in subducting oceanic mantle? *Geology*, *29*, 299-302.

- Peacock, S. and K. Wang (1999), Seismic consequences of warm versus cool subduction metamorphism: examples from southwest and northeast Japan, *Science*, 286, 937-939.
- Sato, H, N. Hirata, K. Koketsu, D. Okaya, S. Abe, R. Kobayashi, M. Matsubara, T. Iwasaki, T. Ito, T. Ikawa, T. Kawanaka, K. Kasahara, S. Harder (2005), Earthquake Source Fault Beneath Tokyo, *Science*, 309, 462-464.
- Schaff, D. P., G. H. R. Bokelmann, W. L. Ellsworth, E. Zankerka, F. Waldhauser, and G. C. Beroza (2004), Optimizing correlation techniques for improved earthquake location, *Bull. Seismol. Soc. Am.*, 94, 705-721.
- Sekiguchi, S. (2001), A new configuration and an aseismic slab of the descending Philippine Sea plate revealed by seismic tomography, *Tectonophysics*, 341, 19-32.
- Smith, W. H. F., and D. T. Sandwell (1997), Global seafloor topography from satellite altimetry and ship depth soundings, *Science*, 277, p. 1957-1962.
- Tichelaar, B. W., and L. J. Ruff (1993), Depth of seismic coupling along subduction zones, *J. Geophys. Res.*, 98(B2), 2017-2038.
- Toda, S., R. S. Stein, S. B. Bozkurt, R. Nakamura (2005), A dislodged block wedged beneath Tokyo, and implications for the enigmatic 1855 Ansei-Edo earthquake, *Eos Trans. AGU*, 86 (52), Fall Meet. Suppl., Abstract S21A-0199.
- Waldhauser, F. and W. L. Ellsworth (2000), A double-difference earthquake location algorithm: Method and application to the northern Hayward fault, *Bull. Seismol. Soc. Am.*, 90, 1353-1368.
- Zhang, H., and C.H. Thurber (2003), Double-difference tomography: The method and its application to the Hayward fault, California, *Bull. Seismol. Soc. Am.*, 93, 1875-1889.

Zhang, H., and C.H. Thurber (2006), Development and applications of double-difference seismic tomography, *Pure Appl. Geophys.*, doi: 10.1007/s00024-005-0021-y, in press.

Zhang, H., C. H. Thurber, D. Shelly, S. Ide, G. C. Beroza, and A. Hasegawa (2004), High-resolution subducting-slab structure beneath northern Honshu, Japan, revealed by double-difference tomography, *Geology*, 32, 361-364, doi: 10.1130/G20261.1.

Zhao, D., A. Hasegawa, and S. Horiuchi (1992), Tomographic imaging of *P* and *S* wave velocity structure beneath northeastern Japan, *J. Geophys. Res.*, 97, 19,909-19,928.

3. LOW-FREQUENCY EARTHQUAKES IN SHIKOKU, JAPAN, AND THEIR RELATIONSHIP TO EPISODIC TREMOR AND SLIP

Non-volcanic seismic tremor was discovered in the Nankai trough subduction zone in southwest Japan [Obara, 2002] and subsequently identified in the Cascadia subduction zone [Rogers and Dragert, 2003]. In both locations, tremor is observed to coincide temporally with large slow slip events on the plate interface downdip of the seismogenic zone [Rodgers and Dragert, 2003; Dragert *et al.*, 2001; Miller *et al.*, 2002; Obara *et al.*, 2004; Hirose and Obara, 2005; Obara and Hirose, 2006]; however, the relationship between tremor and aseismic slip remains uncertain, largely due to difficulty in constraining the source depth of tremor. In southwest Japan, a high quality, borehole seismic network allows identification of coherent *S*-wave (and sometimes *P*-wave) arrivals within the tremor, whose sources are classified as low-frequency earthquakes (LFEs). Since LFEs comprise at least a portion of tremor, understanding their mechanism is critical to understanding tremor as a whole. Here we provide strong evidence that these LFEs occur on the plate interface, coincident with the inferred zone of slow slip. The locations and characteristics of these events suggest that they are generated by shear slip during otherwise aseismic transients, rather than by fluid flow. High pore fluid pressure in the immediate vicinity, as implied by our estimates of seismic *P*- and *S*-wave speeds, may act to promote this transient mode of failure. LFEs could potentially contribute to seismic hazard forecasting by providing a new means to monitor slow slip at depth.

The material in this chapter has appeared in Shelly, D. R., G. C. Beroza, S. Ide, and S. Nakamura (2006), Low-frequency earthquakes in Shikoku, Japan and their relationship to episodic tremor and slip, *Nature*, 442, 188-191, doi:10.1038/nature04931.

A key to understanding the mechanism of deep non-volcanic tremor is determining exactly where it is generated; however, tremor is very difficult to locate due to its small amplitude and scarcity of coherent impulsive wave arrivals of the sort used to locate ordinary earthquakes. Epicentral locations based on seismogram envelope cross-correlation constrain tremor to lie within a belt that follows the strike of the subducting plate². At these locations the depth of the plate interface is 30-45 km, but the depth of the tremor source is less certain.

At least two hypotheses might explain the observed tremor signals. One is that tremor is generated by the movement of fluids at depth, either by hydraulic fracturing [Obara, 2002; Seno and Yamasaki, 2003] or by coupling between the rock and fluid flow [Katsumata and Kamaya, 2003]. In this model, tremor might be analogous to much shallower volcanic tremor, which is thought to arise from the coupling of fluid flow to the solid Earth in volcanic systems [Chouet, 1988, Julian, 1994]. The correlation between tremor and aseismic slip could be explained if the slip is triggered by the same fluid movement that generates the tremor or, alternatively, if the fluid flow is a response to changes in stress and strain induced by slip [Kao *et al.*, 2005].

A second possibility is that tremor is generated directly by slow shear slip on the plate interface [Obara and Hirose, 2006]. Under this hypothesis, tremor is the weak seismological signature of slip that is otherwise too slow to generate detectable seismic waves. In this scenario, tremor could be generated during aseismic transients as slip locally accelerates due to the effects of geometric or physical irregularities on the plate interface. Fluids might play an auxiliary role, altering the conditions on the plate interface to enable transient slip events, without generating seismic waves directly.

Since 1999, the Japan Meteorological Agency (JMA) has differentiated a new class of events denoted as low-frequency earthquakes (LFEs) in their seismicity catalogue. These events occur almost exclusively as part of an extended duration tremor signal [Obara and Hirose, 2006; Kasumata and Kamaya, 2003] (Fig. 3.1). They therefore

correlate strongly with observed slow slip events. The LFEs and extended tremor also locate in the approximately the same region [Obara, 2002; Hirose and Obara, 2005; Obara and Hirose, 2006; Seno and Yamasaki, 2003; Katsumata and Kamaya, 2003] and exhibit similar migration behaviour along strike [Obara, 2002; Obara et al., 2004; Hirose and Obara, 2005; Obara and Hirose, 2006]. While it's uncertain whether or not LFEs and extended duration tremor represent a single phenomenon, their close association means that their mechanisms are likely intertwined. Fig. 3.2 shows waveform records of a long-duration tremor sequence containing several LFEs. The visible arrivals from these events are primarily *S*-waves, and if arrivals from the same source are distinguished at enough stations, the event is included in the JMA seismic catalogue. For such events, usually only the *S*-wave arrival time is reported. Due to the lack of *P*-wave measurements and because the *S*-wave arrival is often emergent, catalogue locations of these events have large uncertainties, especially in depth.

To improve this situation, we use a combination of waveform cross-correlation and double-difference tomography [Zhang and Thurber, 2003; Zhang et al., 2004] to relocate these LFEs in the western Shikoku region of the Nankai trough. We also obtain high-resolution velocity structure and precise locations of ordinary earthquakes. Although tremor (including LFEs) is observed along much of the Nankai trough, it is exceptionally active in western Shikoku.

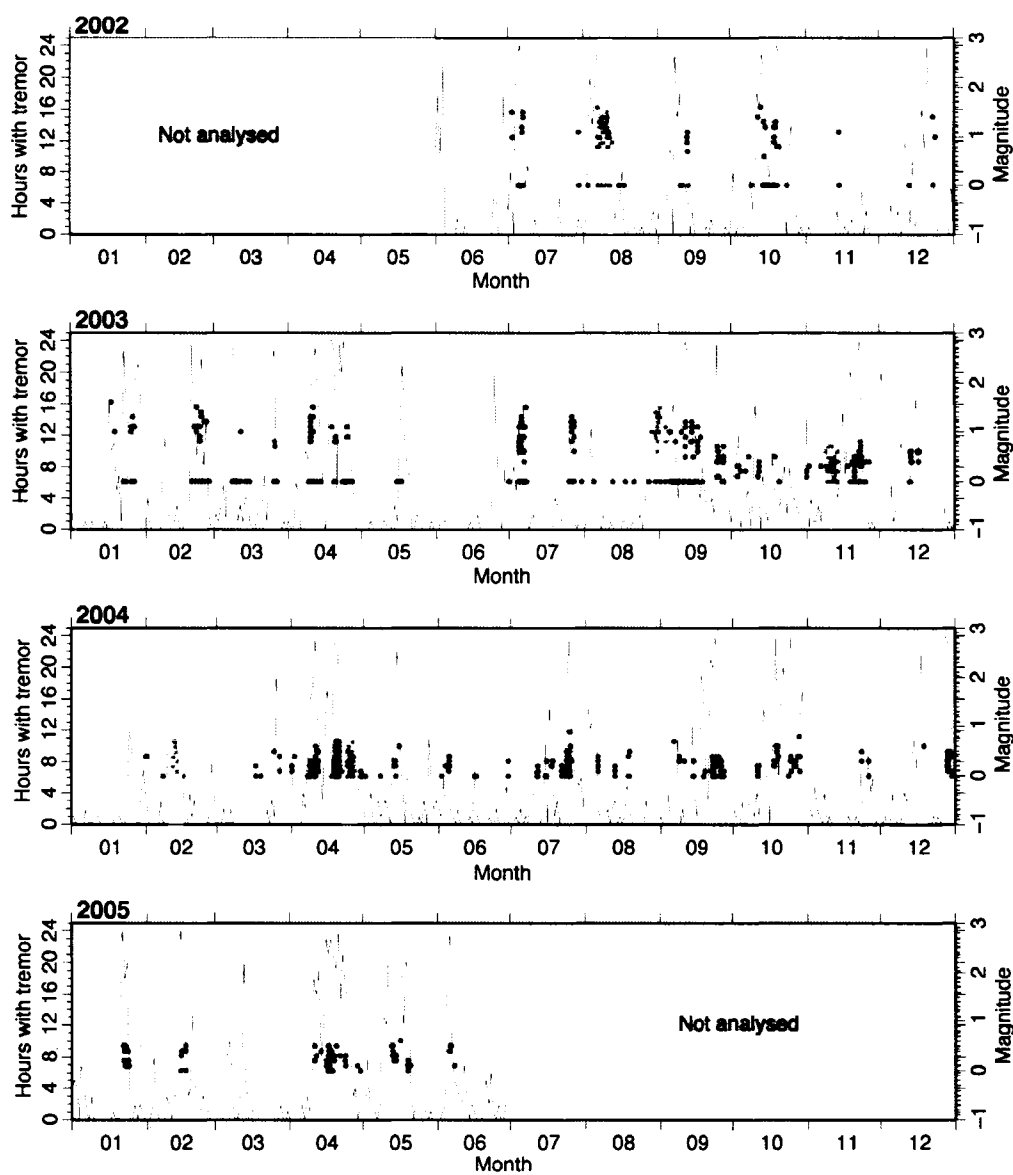


Figure 3.1. Comparison of temporal distribution of tremor activity and low-frequency earthquakes (LFEs) in western Shikoku. The horizontal axis indicates time, with each year a separate panel, beginning in 2002. Red dots denote LFEs with magnitude on the vertical axis. The black line indicates the number of hours containing tremor per day. Yellow bars indicate the period and duration of detected slow slip events [Obara et al, 2004; Hirose and Obara, 2005], which are modelled to occur near the plate boundary beneath western Shikoku. Events with an undetermined magnitude are plotted as magnitude=0. The magnitude determination method changes during September 2003.

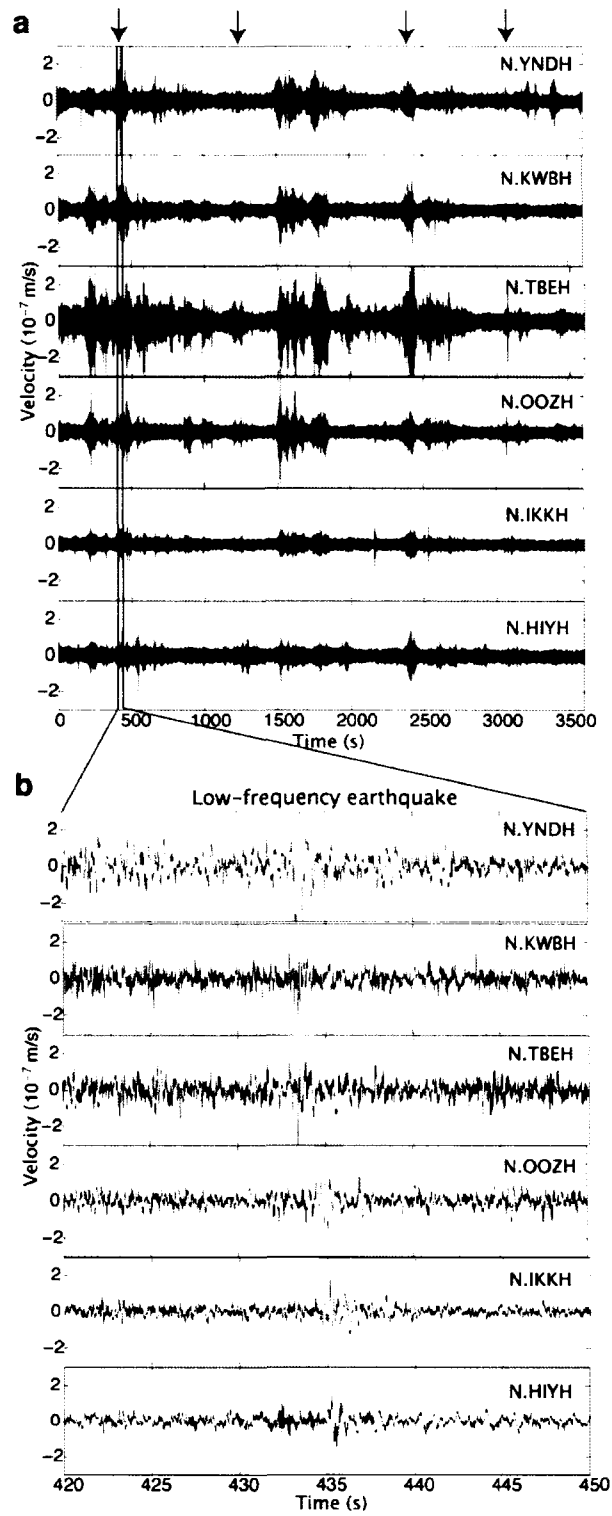


Figure 3.2. An extended period of tremor containing four identified LFEs. **a**, One hour of unfiltered east component velocity seismograms for August 29, 2005, beginning at 17:00 local time during a tremor sequence as recorded at six Hi-net borehole stations in western Shikoku. Arrows indicate times of LFEs. **b**, Expanded view of seismograms showing one LFE from part **a**. *S*-wave arrivals can be identified on these seismograms between 433 and 436 seconds and are highlighted in gray. Traces are ordered by the time of the *S*-wave arrival, with the earliest arrival on top. *P*-wave arrival is too weak to be obviously visible above the noise, even on vertical seismograms, but often can be measured for such events using cross-correlation.

Fig. 3.3 shows the events, stations, and the horizontal distribution of velocity inversion nodes used in this study. Vertically, the velocity node spacing is 5 km. In total, we relocate 6713 events occurring between June 2002 and June 2005, including 1180 LFEs, using waveforms from 112 seismic stations operated by the National Research Institute for Earth Science and Disaster Prevention (NIED), JMA, University of Tokyo, and Kochi University. This includes 77 stations from the recently installed NIED Hi-net high-sensitivity borehole network, which provides especially high quality, low noise waveforms [Obara et al., 2005]. In addition to these data, we use *P* and *S*-wave arrival time picks, provided by JMA for all stations. More details about the data and inversion process are included in the methods section.

We find that the waveforms of LFEs recorded at the same station often correlate with each other, suggesting a similar source location and mechanism for these events. Their waveform similarity is high enough for successful relocation using cross-correlation-derived differential times. Starting with only a rough estimate of the *P*- or *S*-wave arrival time, we obtain precise differential travel time measurements by cross-correlation waveform alignment. Figure 3.4 demonstrates the dramatic reduction in measurement error achieved by cross-correlation of LFE waveforms. Among the LFEs, *S*-wave correlations are particularly successful due to the greater amplitude and signal to noise ratio, of the *S*-waves compared with *P*-waves. However, despite the lack of *P*-wave arrival times in the catalogue, we are able to obtain *P*-wave differential arrival times for LFEs by correlating waveforms in a window centred on a theoretical *P* arrival time estimated from the *S*-wave arrival time and origin time (Fig. 3.5). We are also able to obtain successful *P*-wave and *S*-wave correlations between some LFEs and ordinary earthquakes (Fig. 3.6). These correlations are especially important because they demonstrate similarity of the LFEs with known shear sources, and because they help locate the LFEs relative to intra-slab seismicity. The correlations with regular seismicity along with the observed larger *S*-wave amplitudes suggest that the LFEs themselves represent shear failure.

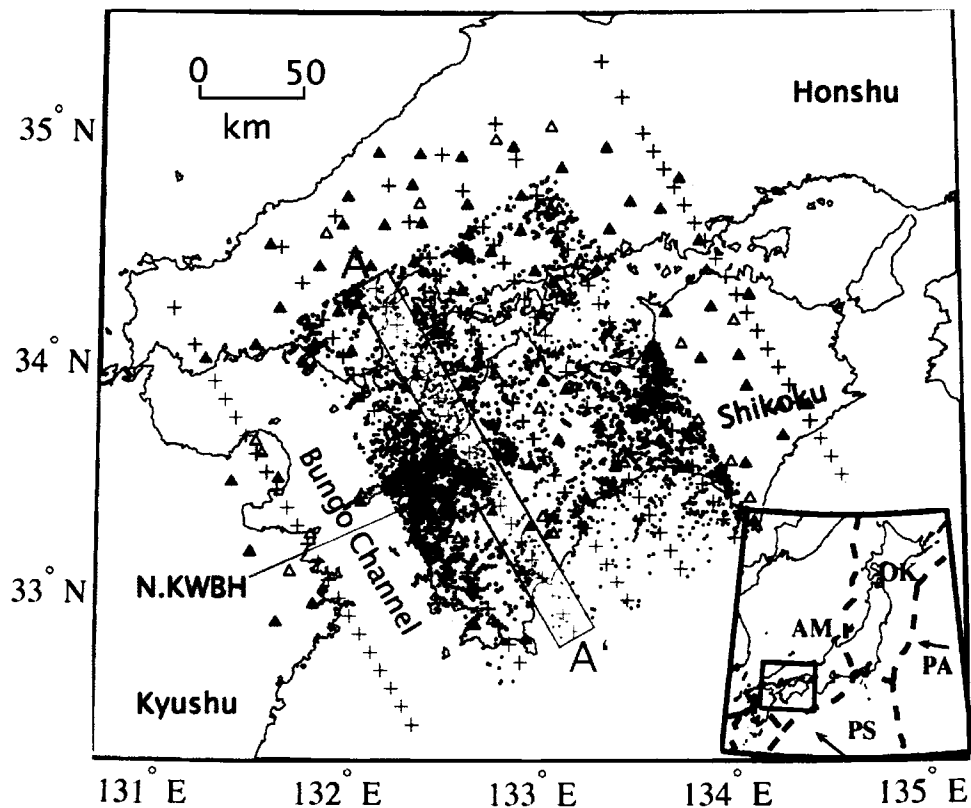


Figure 3.3. Area map with events, stations, and velocity nodes used in the inversion. Black dots indicate regular earthquakes and red dots indicate LFEs. Black triangles show seismic stations used in the inversion, filled triangles denote Hi-net borehole stations, and blue pluses indicate the horizontal locations of velocity nodes. The shaded yellow region shows the zone of earthquakes and LFEs plotted on cross-section A-A' in Fig. 3.7. Inset in the lower right shows the broader tectonics of the region, with the red box indicating the area shown in the main figure. Dashed lines indicate plate boundaries. PA=Pacific plate, PS=Philippine Sea plate, AM=Amur Plate, OK=Okhotsk plate. Plate model is PB2002 [Bird, 2003].

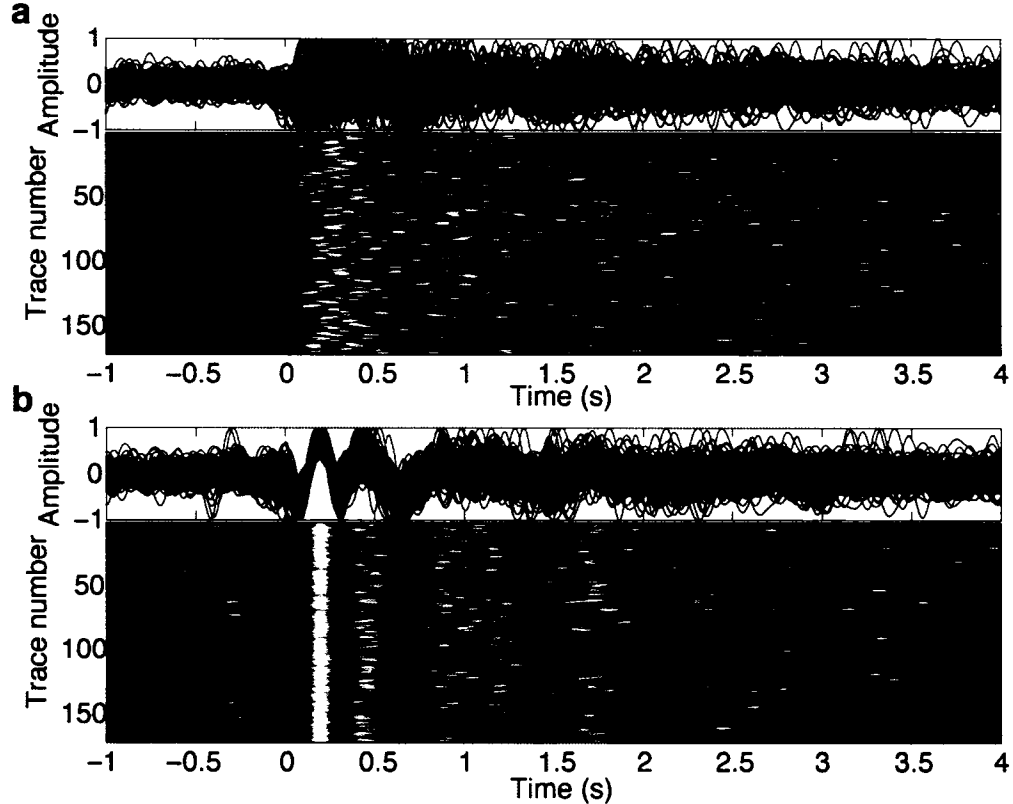


Figure 3.4. *S*-wave alignment for 172 correlated LFEs recorded at NIED Hi-net station N.KWBH, north component. **a**, Alignment using catalogue arrival time. **b**, Alignment using cross-correlation differential time. Waveforms are amplitude normalized and bandpass filtered between 1 and 8 Hz. The top portions of **a** and **b** show the waveforms plotted on top of each other; the grey trace is the “master event” with which the other events are correlated. The bottom portions show each trace with normalized amplitude indicated by shading, with black=-1 and white=+1 amplitude. Note the precisely aligned *S*-wave arrivals in part **b**, demonstrating the dramatic reduction in measurement error achieved using cross-correlation differential times. Waveforms are shifted by up to 0.85 seconds from the catalogue pick time in order to achieve this alignment. Time=0 corresponds to the approximate *S*-wave arrival time.

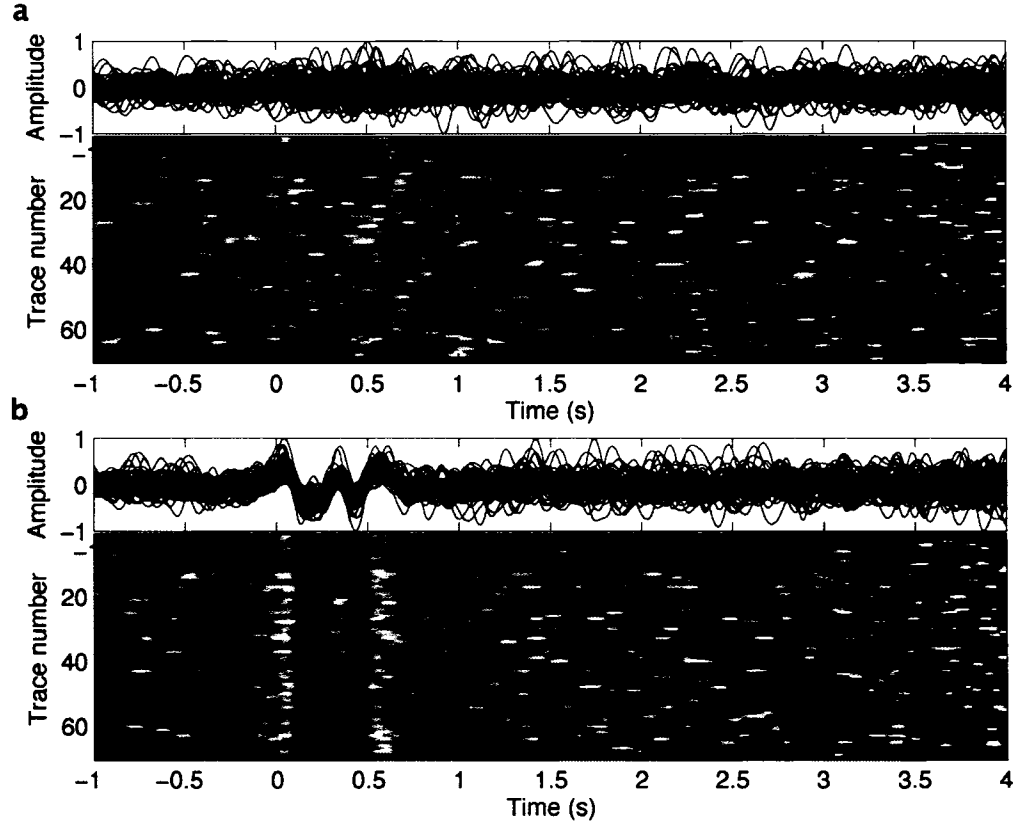


Figure 3.5. *P*-wave alignment for 70 correlated LFEs recorded at NIED Hi-net station N.KWBH, vertical component. **a**, Waveforms aligned by catalogue (or theoretical) *P*-wave arrival time. **b**, Waveforms aligned by cross-correlation differential time. The red trace in **a** and **b** is the “master” event, with which all others are correlated. Traces are shifted by up to 0.90 s to achieve the alignment as shown in **b**. If no *P*-wave arrival time is given in the catalogue (as is common for LFEs), we cross-correlate the waveforms in a window centred on the theoretical arrival time, calculated from the listed *S*-wave arrival and origin times. Thus, using cross-correlation, we are able to make differential *P*-wave measurements for many LFEs with *P*-wave arrivals too weak to be identified. Time=0 corresponds to the approximate *P*-wave arrival time. For more details on the figure, see the caption to Fig. 3.4.

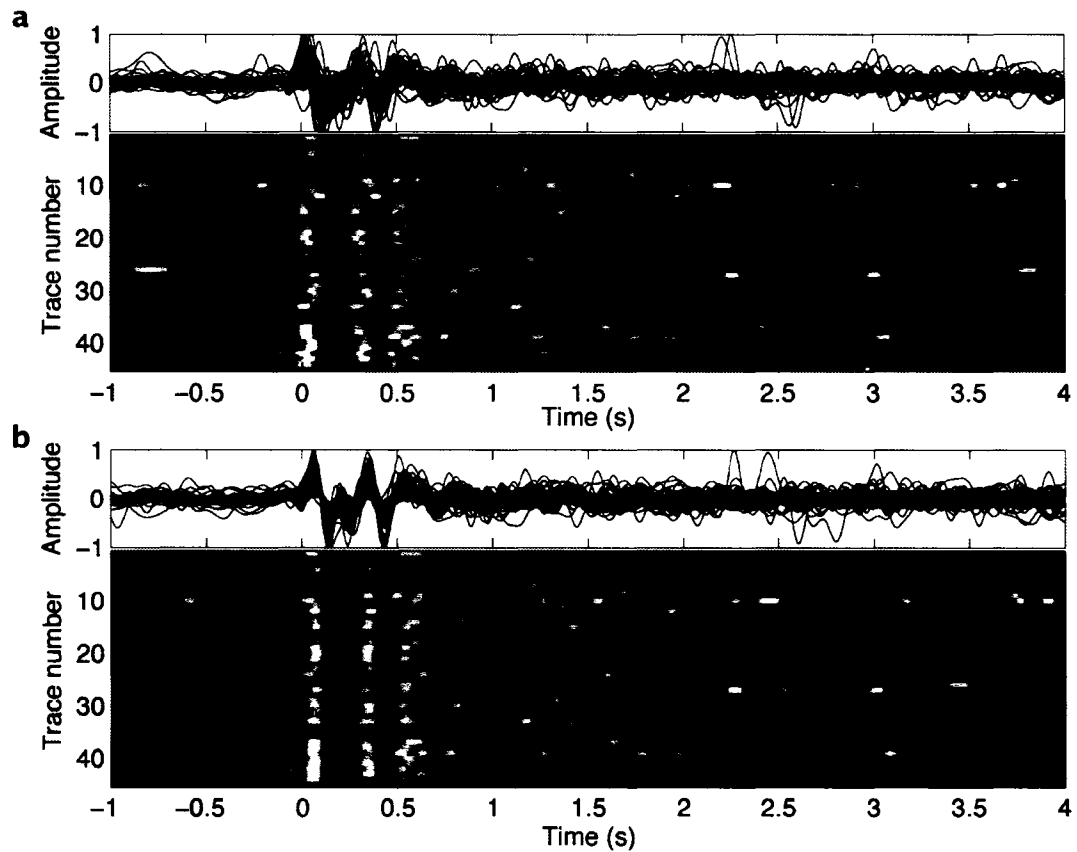


Figure 3.6. An example of the correlation of a LFE with 45 regular earthquakes recorded at NIED Hi-net station N.KWBH, vertical component. **a**, Traces aligned with the catalogue P -wave arrival time. **b** Traces aligned with cross-correlation differential time. The red “master” event in **a** and **b** is a LFE, while the other traces are from regular earthquakes that correlate with this LFE. Time=0 corresponds to the approximate P -wave arrival time. For more details, see the caption to Fig. 3.4.

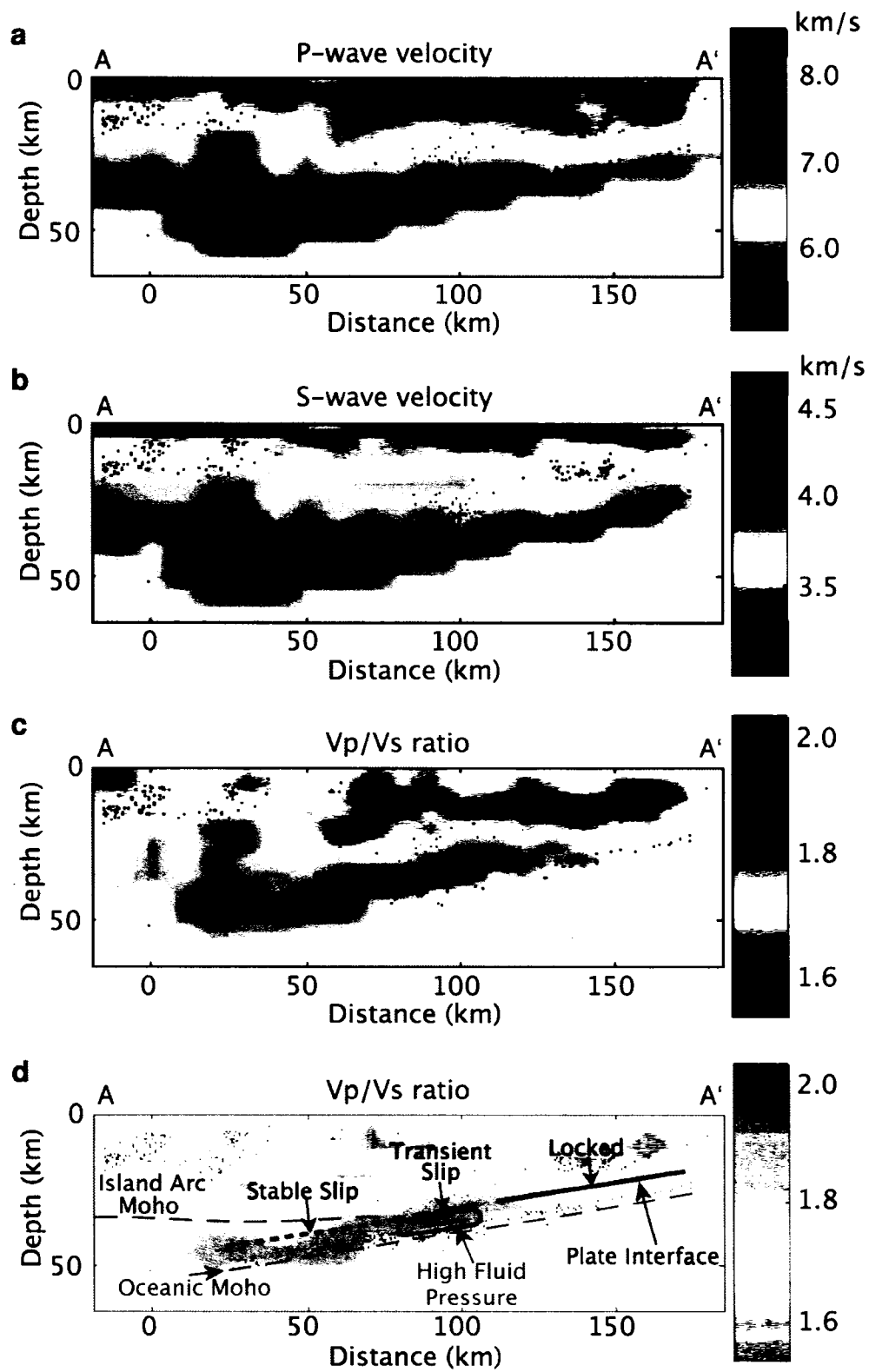


Figure 3.7. Seismic velocities and relocated hypocenters along cross-section A-A'. **a**, P -wave velocity. **b**, S -wave velocity. **c**, V_p/V_s ratio. This cross-section is selected because it cuts through the region of highest tremor and LFE activity (see Fig. 3.2). Relocated hypocenters are plotted for events within 9 km of the cross-section (the yellow highlighted region in Fig. 3.3), with black dots indicating regular earthquakes and the red dots indicating LFEs. Faded areas represent regions of poor resolution, where the derivative weight sum (DWS) value is less than 50. **d**, Schematic diagram of our interpretation overlaid on the V_p/V_s structure. We interpret the LFEs to occur on the plate interface, while the seismicity within the slab occurs primarily within the oceanic lower crust. The oceanic Moho is drawn based on an 8 km crustal thickness, which is consistent with observed P and S -wave velocities in **a** and **b**. Between the LFEs and slab seismicity, within the slab crust, is a distinct region of high V_p/V_s ratio (1.9-1.95), which we interpret as due to high fluid pressure. The plate interface updip of the LFEs is apparently locked, based on rupture models of the 1946 Nankai earthquake [Baba *et al.*, 2002; Tanioka and Satake, 2001] and the lack of current seismicity. Downdip of the LFEs, the plate interface may slip stably.

After relocation, the LFEs collapse onto a distinct plane 5-8 km above, and approximately parallel to, the dipping plane of seismicity within the subducting Philippine Sea slab (Fig. 3.7). In places, the plane of LFEs extends for nearly 20 km in the dip direction of the slab, and they are strongly clustered along-strike (Fig. 3.3). Although it was previously thought that these events occurred within the overriding plate [Katsumata and Kamaya, 2003], we believe they occur on the plate interface. This hypothesis is supported by an independent seismic refraction study, which finds that the plate interface is 3-5 km shallower than previous estimates [Baba *et al.*, 2002], with the top surface corresponding closely to our LFE locations.

Assuming average oceanic crustal thickness (8 km), the location of LFEs on the plate interface places the intra-slab seismicity primarily within the oceanic lower crust (Fig. 3.7D). An increase in P and S -wave velocities seen just below the slab seismicity (Fig. 3.7), as well as recent receiver function analysis [Shiomi *et al.*, 2004], further support this location of the oceanic Moho. The intra-slab seismicity appears to begin within the lowermost crust at shallower depths and expand upward within the crust as the slab subducts. Such behaviour is consistent with thermal-petrologic models for this region, which predict metamorphic reactions to occur first within the hotter lower crust [Peacock and Wang, 1999], but contrasts with expectations that intra-slab seismicity occurs primarily within the upper crust [Hacker *et al.*, 2003]. This issue remains an important subject of future research.

In the immediate vicinity of the LFEs, we find a zone of high V_p/V_s ratio (1.9-1.95), likely indicating high pore-fluid pressures [Christensen, 1984]. Fig. 3.7 shows the estimated P , S , and V_p/V_s velocity structure on a cross-section through an area of high LFE activity. A checkerboard test (Fig. 3.8) demonstrates that our model is well resolved. The most prominent area of high V_p/V_s is located between the LFEs and the intra-slab seismicity, within the subducting crust. The high V_p/V_s zone is most pronounced on the cross-section with the most LFE activity (Fig. 3.7) and is consistent with the hypothesis that these LFEs are enabled by the release of fluids in the subduction zone. A likely source of fluids is dehydration of hydrous minerals within

the subducting oceanic crust, a process also proposed to enable intra-slab seismicity [*Hacker et al.*, 2003; *Raleigh and Paterson*, 1965; *Kirby*, 1995].

High pore-fluid pressure on the plate interface has the potential to alter the mode of slip by extending the conditionally stable region, as proposed for the Tokai segment at the northeast end of the Nankai trough [*Kodaira et al.*, 2004] in order to explain a long-term slow-slip event on this segment [*Ozawa et al.*, 2002]. Interestingly, this region also experiences a high level of tremor activity [*Obara*, 2002], with epicentral locations of the tremor matching a region of high V_p/V_s within the subducting crust [*Kodaira et al.*, 2003]. This correspondence between active tremor and high V_p/V_s is strikingly similar to what we observe in western Shikoku.

Tremor has recently been discovered outside of a subduction environment under the San Andreas fault system south of Parkfield [*Nadeau and Dolenc*, 2005]. This tremor, estimated to occur below the seismogenic zone at depths of 20-40 km, shares many characteristics with that observed in Japan and Cascadia. Like tremor in subduction zones, tremor on the San Andreas occurs in a region previously thought to deform aseismically, however no associated deformation transient has yet been detected.

We propose that the coupled phenomena of tremor, LFEs, and episodic slow-slip events represent a mode of failure for a transition zone between a locked and continuously creeping fault. In a subduction zone, this corresponds to the transition between the locked megathrust source region up-dip and the continuously slipping region down-dip. In fact, models of co-seismic rupture for the 1946 M_w 8.2 Nankai earthquake [*Baba et al.*, 2002; *Tanioka and Satake*, 2001] terminate only a short distance up-dip of the observed band of LFEs. Some areas where tremor and LFEs occur, such as the Tokai (discussed above) and Bungo Channel regions, have also been observed to fail in longer duration slow-slip events [*Ozawa et al.*, 2002; *Hirose et al.*, 1999; *Miyazaki et al.*, 2003], demonstrating a tendency for transient slip in these areas.

Precise locations indicate that the LFEs analyzed in this study occur on the plate interface. The correlation between LFEs and regular seismicity, the fact that LFEs are primarily composed of shear waves, and the remarkable correspondence with slow-slip events⁵⁻⁷ argue that LFEs represent shear slip on this interface. We propose that LFEs may be generated by local slip accelerations at geometric or frictional heterogeneities that accompany large slow slip events on the plate interface. Long-duration tremor may result simply from a superposition of many concurrent LFEs. Alternatively, long-duration tremor might represent a combined signal of shear slip and fluid flow. We hypothesize that increasing fluid pressure may reduce the effective normal stress and enable slip on the plate interface; this slip could increase permeability and allow pressurized fluid to escape, possibly contributing to the tremor signal in the process. In either case, evidence discussed above suggests that fluids play a key role in the failure process. Remote triggering of tremor and LFEs [*Miyazawa and Mori, 2005*], reminiscent of earthquake triggering seen in hydrothermal regions, provides additional evidence for fluid enablement.

As noted by previous authors [*Rogers and Dragert, 2003; Hirose et al., 1999*], a slow slip event on the subduction interface would increase the stress up-dip on the locked portion, potentially elevating the probability of a large earthquake during or soon after the slow slip. The same concept applies to other fault settings with juxtaposed locked and creeping portions, like the San Andreas [*Nadeau and Dolenc, 2005*]. If LFEs are direct signals of episodic slow-slip, they would illuminate aseismic slip at depth with temporal and spatial precision well beyond that attainable with surface geodetic instruments. With proper instrumentation and analysis, we will likely detect similar events within tremor in regions beyond southwest Japan. Consequently, LFEs may provide critical information for monitoring the seismic hazard in a variety of tectonic settings.

METHODS

In order to resolve the velocity structure of the mantle wedge, we included catalogue difference times for events up to 75 km separation and attempted cross-correlations for events with up to 20 km horizontal and 50 km vertical separation. To attain the best correlations and reduce the likelihood of correlating noise, we bandpass filtered the data between 1 and 8 Hz before cross-correlating. We accepted a cross-correlation measurement if the sum of the maximum cross-correlation coefficient and the mean coherence was greater than 1.40. In total, we used 3.9 million cross-correlation differential times (64% of which were *S*-wave measurements), 200,000 absolute arrival times (55% *S*), and 6.6 million catalogue differential times (58% *S*).

For the inversion, we used an initial 1-D velocity model, approximating that used by the JMA since 2001 for routine earthquake locations. The velocity is interpolated linearly between nodes, and the slowness is regularized in each coordinate direction. The calculated V_p/V_s ratio is simply the quotient of the *P* and *S*-wave velocity models.

To examine the velocity structure resolution, we performed two checkerboard resolution tests in cross-section (Fig. 3.8). For these tests, we first calculated synthetic travel times using a velocity model with velocities +5% and -5% from our normal starting velocity model. We then performed the inversion using these synthetic times with parameters identical to those used in the actual inversion. To estimate resolution on multiple scales, we conducted this test using two different block sizes. Fig. 3.8a-d shows the results using a model with 20 km by 20 km blocks in cross-section (2 nodes horizontally by 4 nodes vertically), while Fig. 3.8e-h shows the same test with blocks 10 km (vertically) by 20 km (horizontally). In each case, to examine the resolution of our V_p/V_s model, we performed a separate test with a perturbed V_s model and unperturbed V_p model (Fig. 3.8d,h). The results of these tests demonstrate very good resolution in nearly all areas above the deepest slab seismicity, with excellent resolution in the central part of the model.

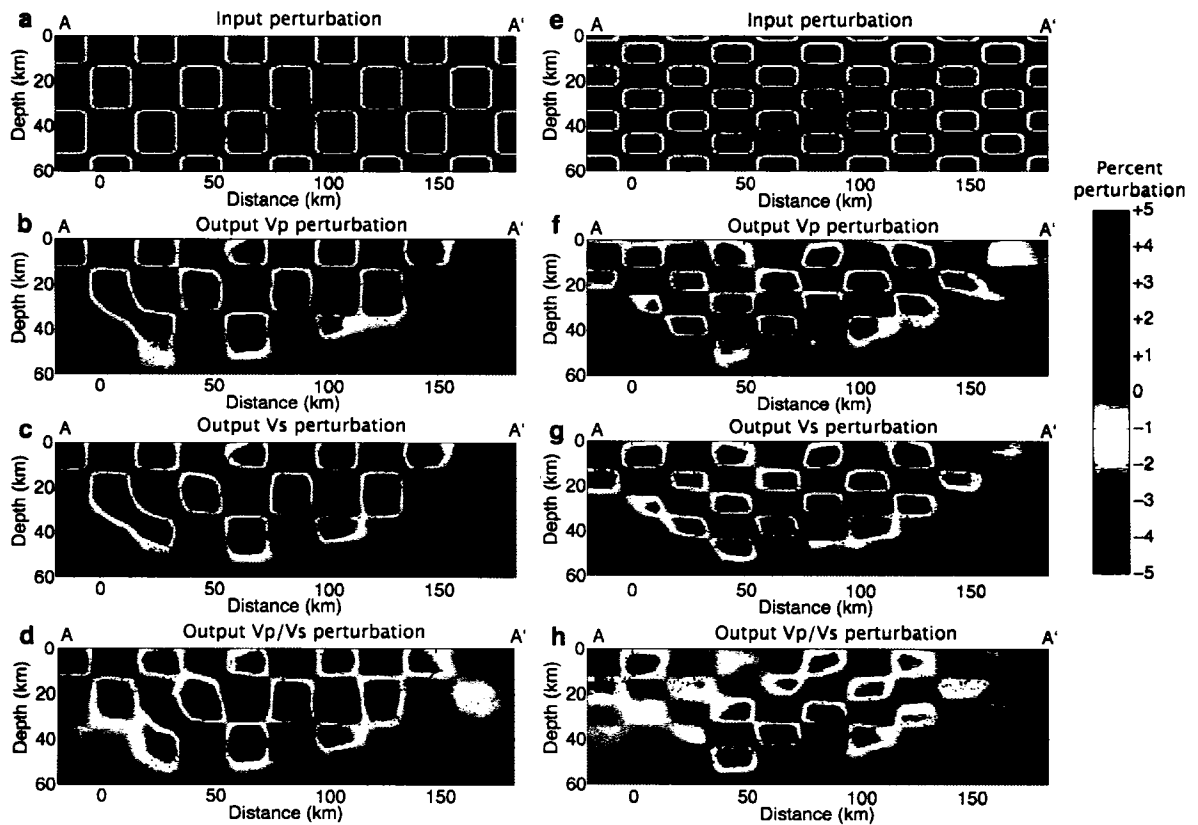


Figure 3.8. Two checkerboard resolution tests for cross-section A-A' shown in Fig. 3.3. Parts a-d show the test performed using 20 by 20 km blocks perturbed by $\pm 5\%$ relative to the normal starting model, while parts e-h show the same test using blocks 10 km (vertically) by 20 km (horizontally) a, Input perturbation for each output property shown in parts b, c, and d. b, Output P -wave model. c, Output S -wave model. d, Output Vp/Vs ratio. Parts b and c are produced in one test, while part d is produced in a separate test. Part d is generated with a perturbed input Vs model and unperturbed input Vp model, in order to produce a perturbed Vp/Vs model. Panels e-h are analogous to a-d but with the smaller block size. For the 20x20 km blocks (a-d), recovery of the input velocities and Vp/Vs ratios is very good in nearly all areas above the deepest seismicity. For the 10x20 km blocks (e-h), P and S -wave velocities are well recovered in these same areas. With the smaller blocks, the Vp/Vs ratios (h) are clearly resolved in the central region of the model, but the recovered perturbation amplitudes are reduced outside of this region.

ACKNOWLEDGEMENTS

This material is based upon work supported by National Science Foundation. We thank Dr. Kazushige Obara for allowing us to use his determinations of daily tremor activity. Much of this work was conducted while D.R.S. was a participant in the Summer Institute in Japan program, cosponsored by the Japan Society for Promotion of Science and the National Science Foundation. All data were obtained from the NIED Hi-net data server.

REFERENCES

- Baba, T., Tanioka, Y., Cummins, P. & Uhira, K. The slip distribution of the 1946 Nankai earthquake estimated from tsunami inversion using a new plate model. *Phys. Earth Planet. Inter.*, **132**, 59-73 (2002).
- Bird, P. An updated digital model of plate boundaries. *Geochem., Geophys., Geosyst.* **4**, 1027 (2003).
- Chouet, B. Resonance of a fluid-driven crack: Radiation properties and implications for the source of long-period events and harmonic tremor. *J. Geophys. Res.* **93**, 4375-4400 (1988).
- Christensen, N. I., Pore pressure and oceanic crustal seismic structure. *Geophys J. R. Astron. Soc.*, **79**, 411 (1984).
- Dragert, H., Wang, K. & James, T. S. A silent slip event on the deeper Cascadia subduction interface. *Science* **292**, 1525-1528 (2001).
- Hacker, B. R., Peacock, S. M., Abers, G. A. & Holloway, S. D. Subduction Factory 2. Are intermediated-depth earthquakes in subducting slabs linked to metamorphic dehydration reactions? *J. Geophys. Res.* **108**, doi:10.1029/2001JB001129 (2003).

- Hirose, H. & Obara, K. Repeating short- and long-term slow slip events with deep tremor activity around the Bungo channel region, southwest Japan. *Earth Planets Space* **57**, 961-972, 2005.
- Hirose, H., Hirahara, K., Kimata, F., Fujii, N. & Miyazaki, S. A slow thrust slip event following the two 1996 Hyuganada earthquakes beneath the Bungo Channel, southwest Japan. *Geophys. Res. Lett.* **26**, 3237-3240 (1999).
- Julian, B. R. Volcanic tremor: Nonlinear excitation by fluid flow. *J. Geophys. Res.* **99**, 11,859-11,878 (1994).
- Kao, H. *et al.*, A wide depth distribution of seismic tremors along the northern Cascadia margin. *Nature*, **436**, 841-844 (2005).
- Katsumata, A. & Kamaya, N. Low-frequency continuous tremor around the Moho discontinuity away from volcanoes in the southwest Japan *Geophys. Res. Lett.* **30**, 10.1029/2002GL015981 (2003).
- Kirby, S. H. Intraslab earthquakes and phase changes in subducting lithosphere. *Rev. Geophys.* **33**, 287-297 (1995).
- Kodaira, S. *et al.*, High pore fluid pressure may cause silent slip in the Nankai Trough. *Science* **304**, 1295-1298 (2004).
- Miller, M. M., Melbourne, T., Johnson, D. J. & Sumner, W. Q. Periodic slow earthquakes from the Cascadia subduction zone. *Science* **295**, 2423 (2002).
- Miyazaki, S., McGuire, J. J. & Segall, P. A transient subduction zone slip episode in southwest Japan observed by the nationwide GPS array. *J. Geophys. Res.* **108**, 10.129/2001JB000456 (2003).

- Miyazawa, M. & Mori, J. Detection of triggered deep low-frequency events from the 2003 Tokachi-oki earthquake. *Geophys. Res. Lett.* **32**, doi:10.1029/2005GL022539 (2005).
- Nadeau, R. M. & Dolenc, D. Nonvolcanic tremors deep beneath the San Andreas fault. *Science* **307**, 389 (2005); published online 9 December 2004 (10.1126/science.1107142).
- Obara, K. & Hirose H. Non-volcanic deep low-frequency tremors accompanying slow slips in the southwest Japan subduction zone. *Tectonophysics*, in press.
- Obara, K. Kasahara, K., Hori, S. & Okada, Y. A densely distributed high-sensitivity seismograph network in Japan: Hi-net by National Research Institute for Earth Science and Disaster Prevention. *Rev. Sci. Instrum.* **76**, doi:10.1063/1.1854197 (2005).
- Obara, K. Nonvolcanic deep tremor associated with subduction in southwest Japan. *Science*, **296**, 1679 (2002).
- Obara, K., Hirose, H., Yamamizu, F. & Kasahara, K. Episodic slow slip events accompanied by non-volcanic tremors in southwest Japan subduction zone. *Geophys. Res. Lett.* **31**, doi:10.1029/2004GL020848 (2004).
- Ozawa, S. *et al.*, Detection and monitoring of ongoing aseismic slip in the Tokai region, central Japan. *Science* **298**, 1009-1012 (2002); published online 3 October 2002 (10.1126/science.1076780).
- Peacock, S. M. & Wang, K. Seismic consequences of warm versus cool subduction metamorphism: examples from southwest and northeast Japan. *Science* **286**, 937-939 (1999).
- Raleigh, C. B. & Paterson, M. S. Experimental deformation of serpentinite and its tectonic implications. *J. Geophys. Res.* **70**, 3965-3985 (1965).

Rogers, G. & Dragert, H. Episodic tremor and slip on the Cascadia subduction zone: The chatter of silent slip. *Science* **300**, 1942-1943 (2003).

Seno, T. & Yamasaki, T. Low-frequency tremors, intraslab and interplate earthquakes in Southwest Japan – from a viewpoint of slab dehydration. *Geophys. Res. Lett.* **30**, doi:10.1029/2003GL018349 (2003).

Shiomi, K., Sato, H., Obara, K. & Ohtake, M. Configuration of subducting Philippine Sea plate beneath southwest Japan revealed from receiver function analysis based on the multivariate autoregressive model. *J. Geophys. Res.*, 109, doi:10.1029/2003JB002774 (2004).

Tanioka, Y. & Satake, K. Coseismic slip distribution of the 1946 Nankai earthquake and aseismic slips caused by the earthquake. *Earth Planets Space* **53**, 235-241 (2001).

Zhang, H. & Thurber, C. H. Double-difference tomography: The method and its application to the Hayward fault, California. *Bull. Seismol. Soc. Am.* **93**, 1875-1889 (2003).

Zhang, H. *et al.*, High-resolution subducting-slab structure beneath northern Honshu, Japan, revealed by double-difference tomography. *Geology* **32**, 361-364 (2004).

4. NON-VOLCANIC TREMOR AND LOW FREQUENCY EARTHQUAKE SWARMS

Non-volcanic tremor is a weak, extended duration seismic signal observed episodically on some major faults, often in conjunction with slow slip events [Obara, 2002; Rogers and Dragert, 2003; Nadeau and Dolenc, 2005; Obara et al., 2004]. Tremor may hold the key to understanding fundamental processes at the deep roots of faults and could signal times of accelerated slip and hence increased seismic hazard; however, the mechanism of tremor and its relationship to aseismic slip are as yet unresolved. Here we demonstrate that tremor beneath Shikoku, Japan can be explained as a swarm of small, low-frequency earthquakes, each of which occurs as shear faulting on the subduction zone plate interface. This suggests that tremor and slow slip are different manifestations of a single process.

Tremor is difficult to locate because it lacks the distinct impulsive, body wave arrivals used by traditional earthquake location methods; however, occasionally tremor in Japan contains relatively energetic and isolated pulses that have been identified as low-frequency earthquakes (LFEs) by the Japan Meteorological Agency [Katsumata and Kamaya, 2003]. Compared to nearby ordinary earthquakes, LFEs are enriched in low frequencies ($\sim 1-5$ Hz) and depleted at higher frequencies. Precise relocations of LFEs beneath western Shikoku reveal that they lie along the dipping subduction interface at depths of 30-35 km [Shelly et al., 2006]. Based on their locations and the character of their waveforms, LFEs were inferred to represent fluid-enabled shear slip on the plate boundary as part of concurrently observed slow slip events [Shelly et al., 2006], rather than fluid flow as previously proposed [Katsumata and Kamaya, 2003].

The material in this chapter is in press at *Nature*, with coauthors G. C. Beroza, and S. Ide.

To test this interpretation further, *Ide et al.* calculated the mechanism of LFEs using two independent methods that exploit waveform similarity between LFEs and regular earthquakes in the subducting slab: analysis of LFE *P*-wave first motions and an empirical moment tensor inversion of LFE *S*-waves [Ide et al., 2007]. As shown in Figure 4.1, these techniques each yield results consistent with the mechanisms of slow slip events as well as the most recent mega-thrust earthquake in this area. All these lines of evidence indicate that LFEs are generated by shear slip on the plate interface. Does a similar mechanism generate continuous tremor?

If the same shear-faulting source generates both LFEs and tremor, we might expect to see additional weaker events within tremor with waveforms similar to the previously identified LFEs [Shelly et al., 2006]. The spectra of tremor tracks that of LFEs, but with slightly smaller amplitude (Fig. 4.2), which supports the possibility of a common physical mechanism for the two phenomena.

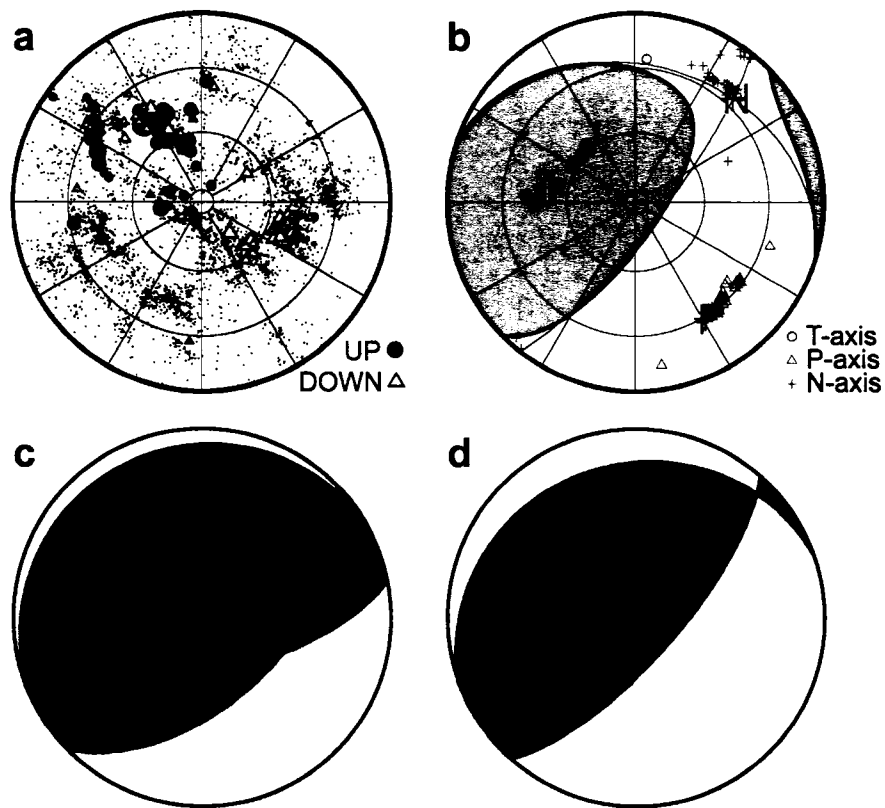


Figure 4.1. Comparison of LFE, slow slip event, and megathrust earthquake mechanisms. **a**, P-wave first motions determined by *Ide et al.* [2007] for low frequency earthquakes by cross correlation-based first motion determination. Solid circles and open triangles indicate compressional and dilatational first motions for LFE *P* waves, respectively. *SNR* for most observations (small dots) is too low to determine the polarity. **b**, Moment tensor inversion results from empirical Green's function analysis of LFE *S* waves. T-, P-, and N- axes are shown together with symbols showing uncertainty and corresponding *P*-wave first motion distribution. **c**, Overlay of the mechanism for three slow slip events near the study area [Hirose and Obara, 2005]. **d**, Mechanism of the 1946 Nankai earthquake [Ando, 1982], which is the most recent mega-thrust earthquake in this region and representative of relative plate motion between the Philippine Sea Plate and the over-riding plate on the dipping plate interface of the Nankai Trough subduction zone. All are shown in equal area projection of lower focal hemisphere.

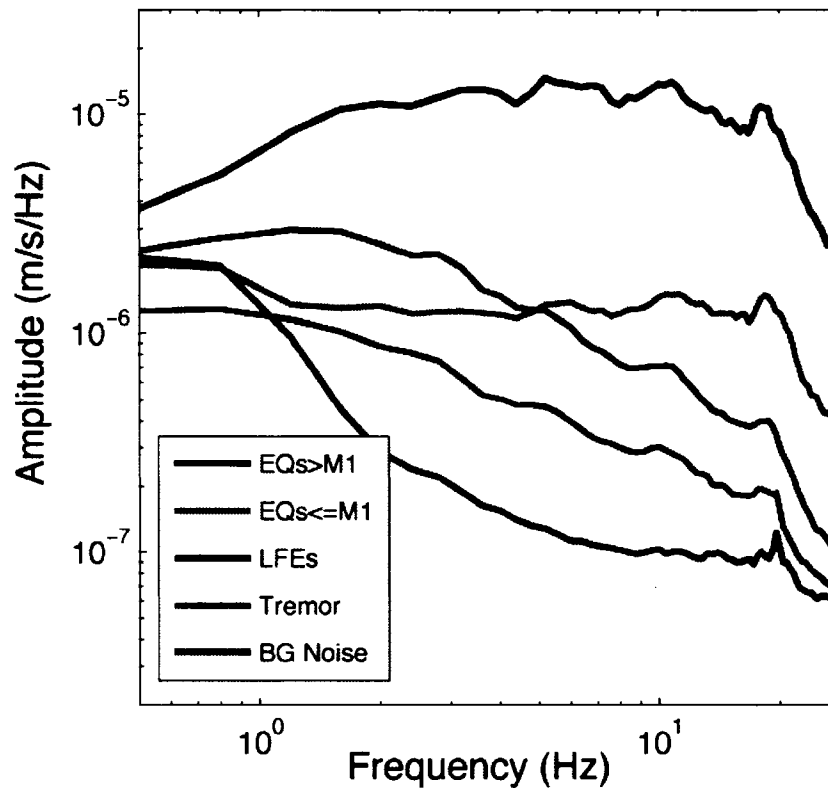


Figure 4.2. Comparison of Earthquake/LFE/Tremor Spectra. Comparison of stacked, uncorrected spectral amplitude from Hi-net velocity seismograms (horizontal components) from multiple nearby events of various kinds. LFEs and regular earthquakes (EQs) are selected from the same hypocentral region (33.4-33.6° N, 132.6-132.8° E, depths 25-45 km). Tremor is selected from approximately the same region. For LFEs and regular earthquakes, spectra are calculated for S-wave arrivals for a 2.5 second window, from 0.5 s before to 2.0 s after the catalog phase arrival. Noise is calculated from a 2.5s window, 2 s before to 0.5 s after the origin time of regular earthquakes. Tremor spectra are calculated from sequential 2.5 s windows over a 400 s time period. Earthquakes are separated by magnitude. We do not divide LFEs by size because their magnitude determination method changed during our study period. In this example, we use: 43 earthquakes with $M > 1$, 52 earthquakes with $M \leq 1$, and 233 LFEs. LFE (red) and tremor (pink) spectra are highly similar, but tremor has smaller amplitude. Small earthquake (dark blue) and very small (light blue) earthquake spectra are highly similar to each other, but lack the rapid decay of amplitude with increasing frequency that is characteristic of both tremor and LFE spectra.

To test this hypothesis, we used the waveforms of 677 of the best-recorded LFEs in this region as “template events” in a matched-filter technique to search tremor waveforms systematically for portions of the tremor that strongly resemble one or more template LFEs [Gibbons and Ringdal, 2006]. We require each template event to be recorded at a minimum of six, 3-component stations. Correlation coefficients from these stations/components are then stacked to produce an “array” correlation sum. We record a detection when this correlation sum peaks above a threshold value.

Since a detected event must possess the same pattern of waveforms across multiple stations and components as the template event, their locations must closely coincide. An example of a positive detection is shown in Figure 4.3, which plots the correlation sum as a function of time as well as waveforms and cross-correlation coefficients at the time of detection across the network. Additional examples of detections and non-detections are shown in Figure 4.4. Because we are working with complex, low signal-to-noise ratio waveforms, individual channels of data show relatively weak correlations and contain insufficient power to detect events when examined in isolation. The strength of the matched-filter approach comes from simultaneously considering waveforms across the network, which increases the detection power dramatically.

The ability to extract a weak signal from noisy data is demonstrated by the synthetic example discussed in the methods section (below) and shown in Figure 4.5. We use the correlation sum as our detection statistic and register a “strong” detection when a value of 8 times the median absolute deviation is exceeded. For a normally distributed random variable this corresponds to an exceedence probability of $\sim 3.3 \times 10^{-8}$. Based on synthetic tests such as the example shown in Figure 4.5, we estimate a location uncertainty for “strong” detections of approximately 3 km.

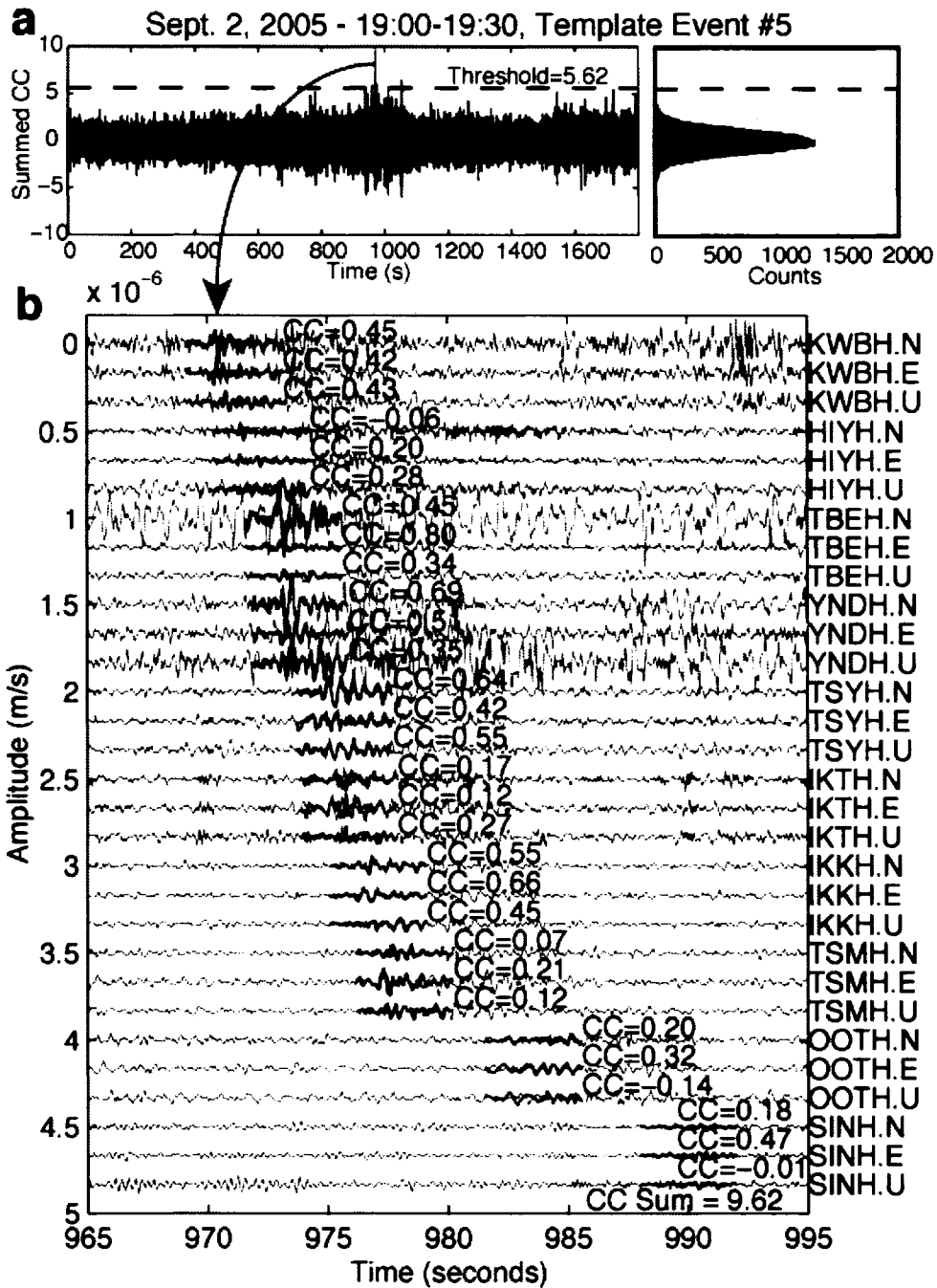
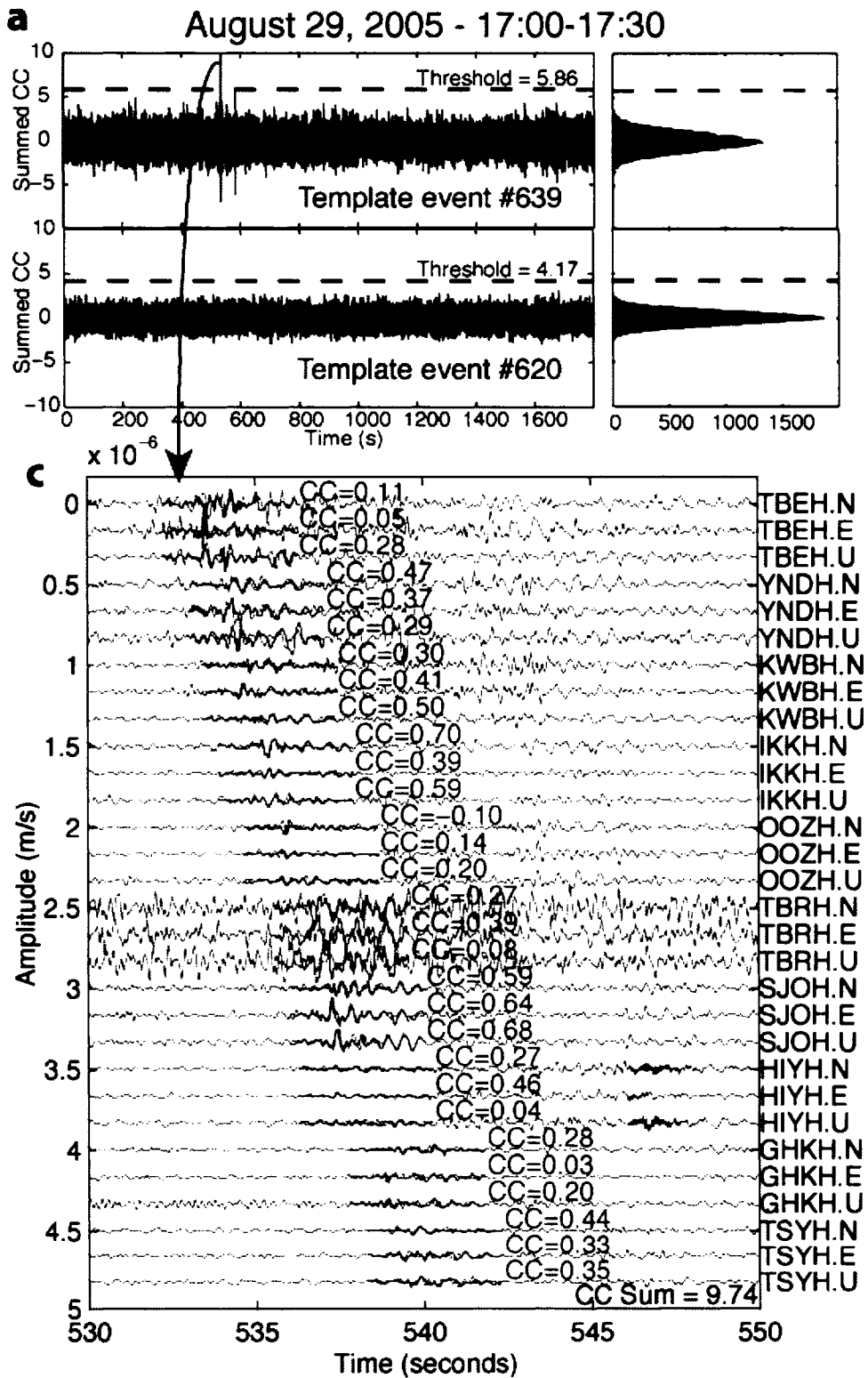


Figure 4.3. Example of a detected LFE. **a**, Correlation sum function for template event #5 during the same 30 minute period as highlighted in Fig. 4.6b. A histogram of correlation sum values is shown on the right. **b**, Continuous tremor waveforms are shown in gray and template event waveforms in black for each component of 10 Hi-net stations. The correlation coefficient (CC) for each trace is shown next to the

template event waveforms. Station names and components are given to the right of each trace. Additional detections (not shown) are also present during this time window. Waveforms are bandpass filtered between 1 and 8 Hz and template event amplitudes are scaled to match the continuous data. Although individual cross correlation coefficients are modest, they are overwhelmingly positive and extremely unlikely to have occurred by chance.



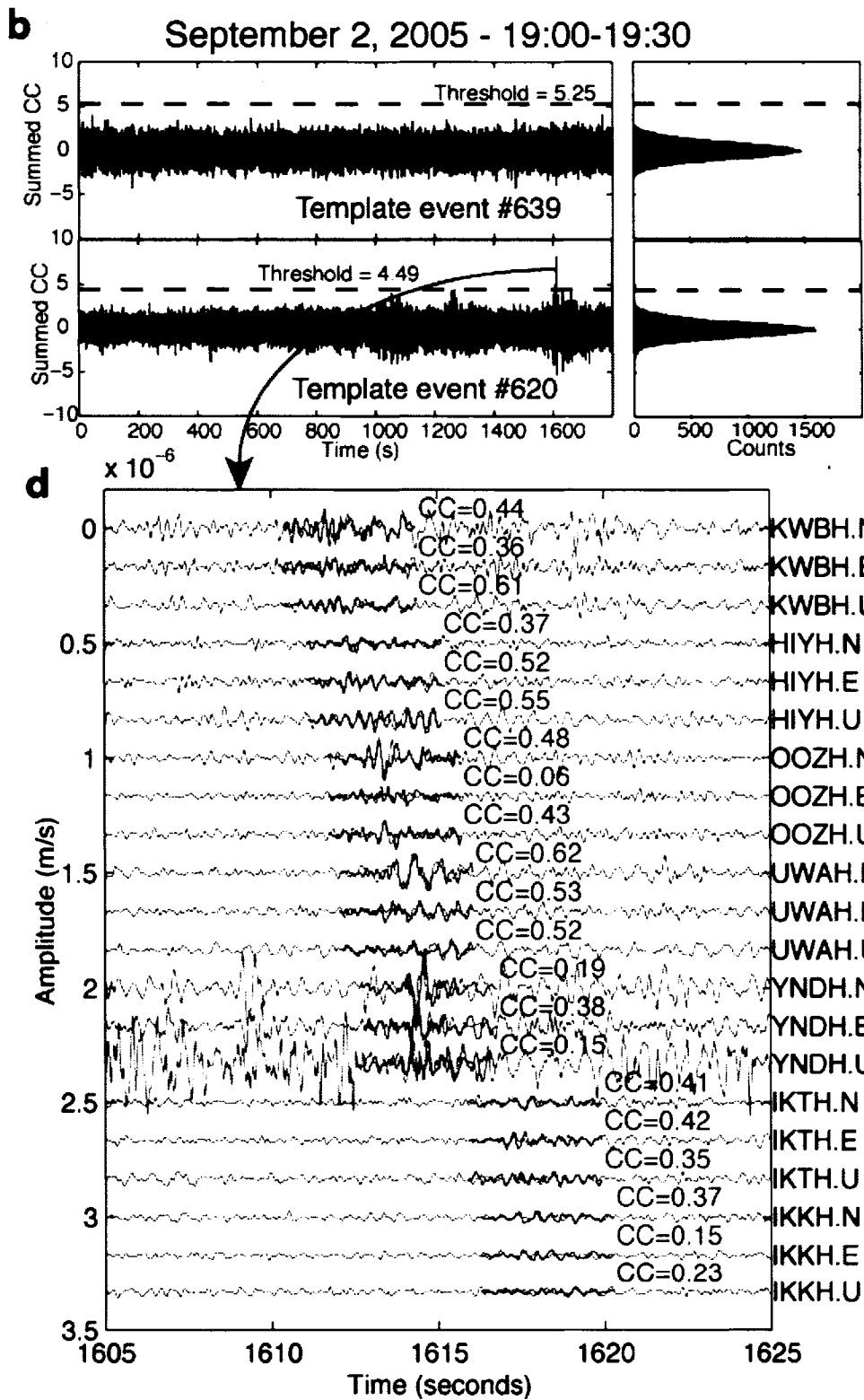


Figure 4.4. Correlation sum functions and detection examples for two template LFEs during two tremor episodes. **a**, Correlation sum functions for template events 639 (upper) and 620 (lower) for the tremor episode August 29, 2005, 17:00-17:30, with histogram of correlation sum values shown to the right. Event #639 has a clear detection while event 620 shows no activity. **b**, Same as **a**, but for the episode September 2, 2005, 19:00-19:30. Notice that in this case, it is event #620 (lower) that is active, while event 639 (upper) is quiet. **c**, Waveforms at the time detection for template event #639 on August 29, 2005 episode. Continuous tremor waveforms are shown in gray and template event waveforms in red for each component of 10 Hi-net stations. The correlation coefficient (CC) for each trace is shown next to the template event waveforms. The station names and components are given to the right of each trace. Additional detections (not shown) are also present during this time window. Waveforms are bandpass filtered between 1 and 8 Hz and template event amplitudes are scaled to match the continuous data. **d**, Same as **c**, but for the detection with template event #620 on September 2, 2005.

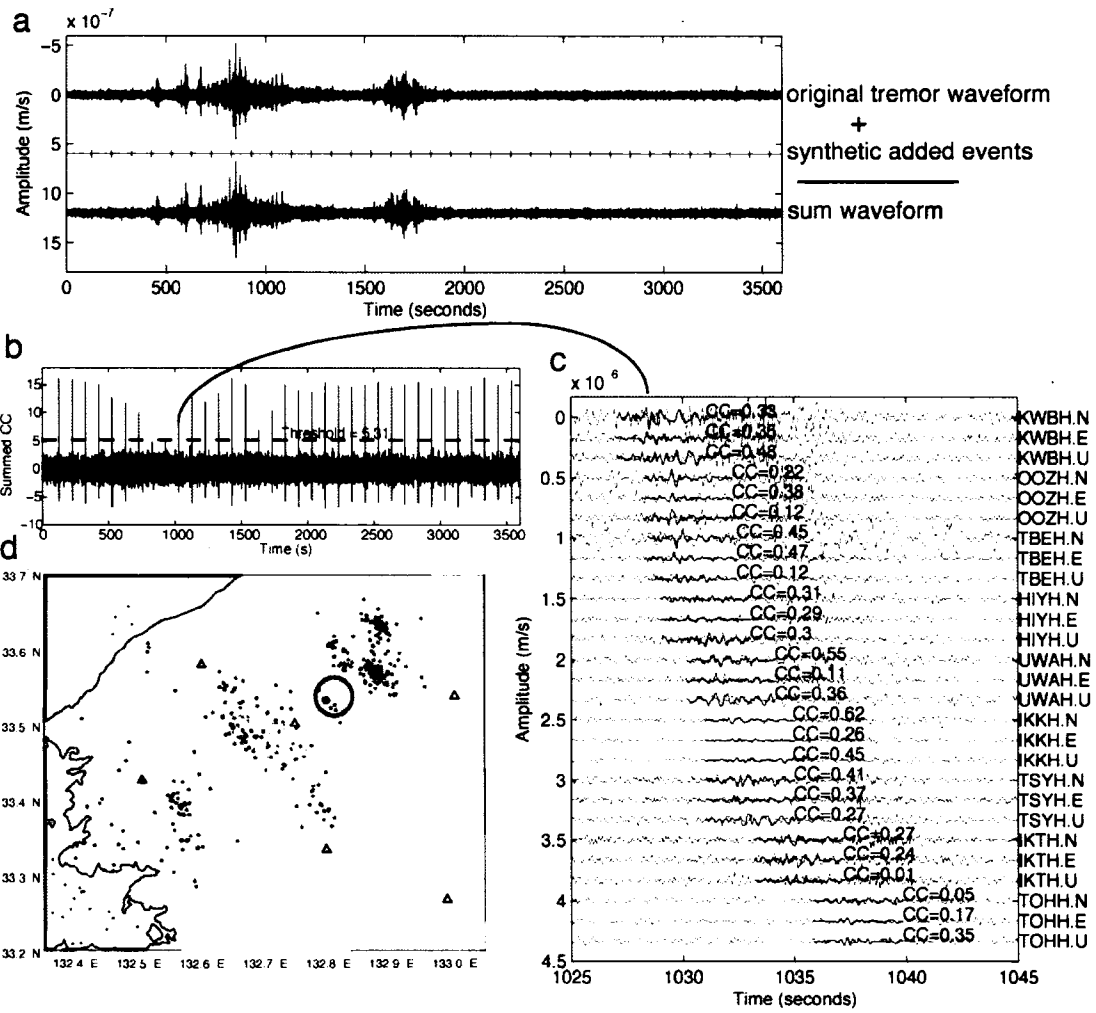


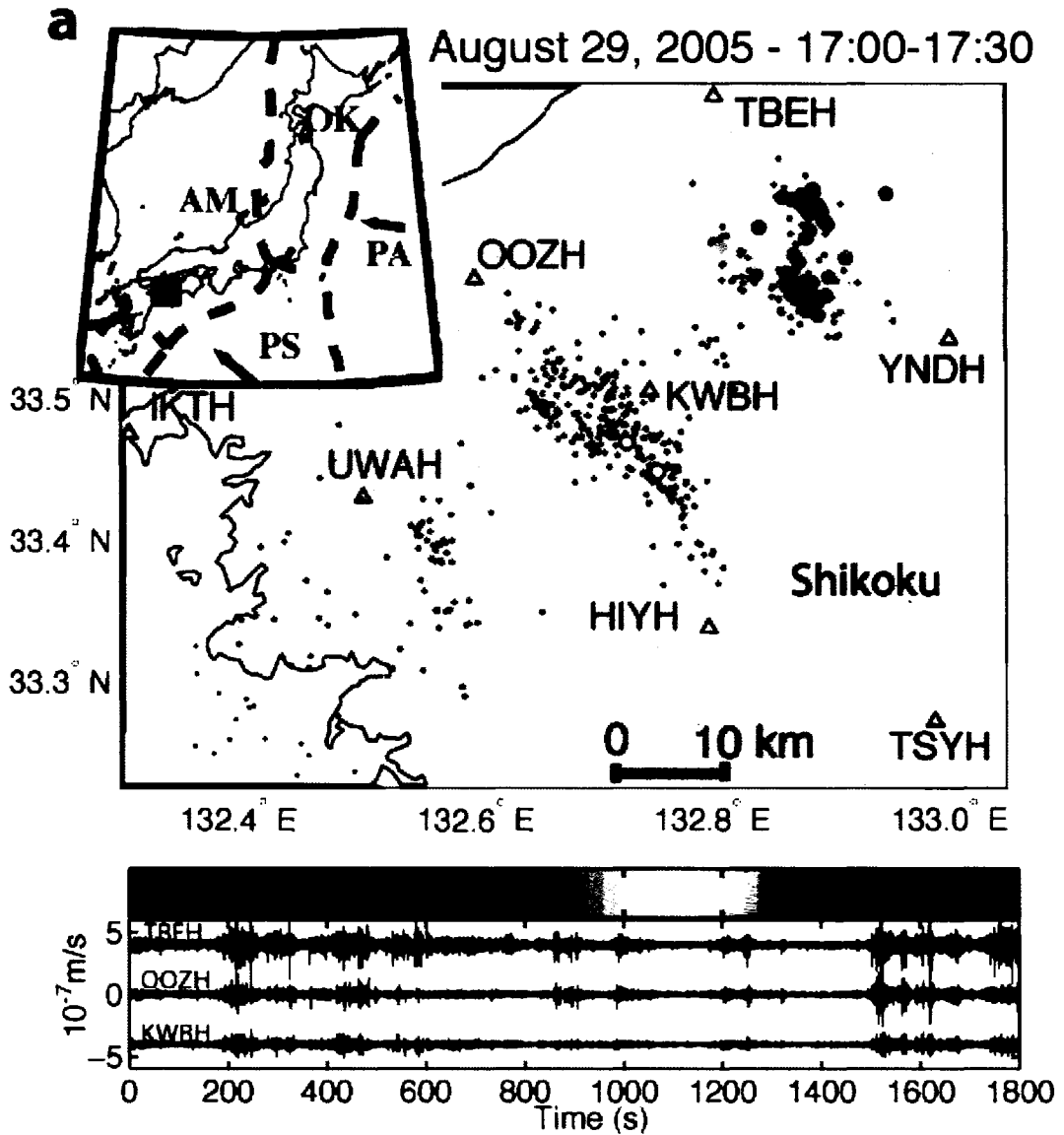
Figure 4.5. Synthetic test of LFE detection capability in the presence of noise and other events. **a**, Original tremor waveform (top, black), added test waveform consisting of a single template event (#83) scaled by 1/10 repeated every 100 s (middle, red), and the modified tremor that is the sum of these two signals (bottom, blue). The waveforms shown are unfiltered, east-component from station KWBH, September 2, 2005 19:00-20:00. Note that the maximum amplitude of the scaled event is smaller than the noise level and much smaller than the amplitude of the visible tremor. **b**, Correlation sum function showing the detections for the template event that was inserted into the real data. In this example, 34/35 instances of the scaled template events are recovered. A correlation peak from the undetected event is visible, but falls below the detection threshold due to the strong competing tremor at this time. **c**, Waveforms at the time of detection for the event inserted near $t=1030$. Gray waveforms are the modified tremor, while red waveforms are from the template event. The correlation coefficient (CC) for each trace is shown next to the template event waveforms. The station names and components are given to the right of each trace. **d**, Map view showing “strong” detected events for this synthetic example, with the color indicating number of detections from 1 (yellow) to 34 (red). Circle in map view shows added event (bright red) and a small amount of “leakage” to 3 nearby LFEs, two of which are located within 0.5 km. The third event is located approximately 3 km away, but has only a single detection compared with 34 for the inserted event. Events outside the circle are detections present in the unaltered tremor data.

In order to allow for the possibility that tremor is excited in the vicinity of, but not at exactly the same location as, a low frequency earthquake in our catalog, we also allow for “weak” detections. In this case, we take the maximum correlation coefficient from a 0.4-second window at each station before summing. For the weak detection, the threshold is set at 9 times the median absolute deviation of the distribution over the median, which corresponds to a probability of $\sim 6.4 \times 10^{-10}$, for the Gaussian case.

Our detection technique reveals a nearly continuous sequence of LFEs during periods of active tremor. Statistical considerations argue against random detections, but perhaps an even more compelling argument can be made based on the highly clustered nature of the positive detections. The detection statistic that we use is normalized, which means that it does not depend on absolute amplitudes. Therefore, there is nothing in the construction of the measurement to favor positive detections of one LFE over another if the tremor consists of incoherently radiated energy or noise. Thus, we expect that false positive detections should be geographically random.

Figure 4.6 shows that rather than being random, the distribution of positive detections is highly clustered. Not only are the detections spatially coherent during a tremor burst, they also show an interesting time progression. Figure 4.6 demonstrates the detailed evolution of two 30-minute episodes of active tremor on different portions of the plate interface. The second example (Fig. 4.6b) is notable in that it shows an episode of tremor migration, with the source moving approximately 15 km up-dip along the interface in just over 20 minutes. This is not a unique occurrence—similar episodes are observed at other times and sometimes propagate in the opposite direction. This along-dip migration rate of ~ 45 km/hr is much faster than along-strike migration rates of 5-17 km/day previously reported in this region¹ and in Cascadia [Dragert et al., 2004; Kao et al., 2006]. Although these slower rates may still govern the longer-term average migration, with the matched-filter technique we can resolve more complex behavior and faster migration rates along both strike and dip. Notably, we also find instances when multiple tremor sources, separated by up to ~ 20 km are

active simultaneously. This may explain some of the variation, particularly in depth, found in previous estimates of tremor location in Cascadia [Kao et al., 2005; 2006]. For a detailed look at tremor behavior during the periods shown in Figure 4.6, please see the movies in Quicktime format included on the enclosed CD (Figures 4.7 and 4.8).



b

September 2, 2005 - 19:00-19:30

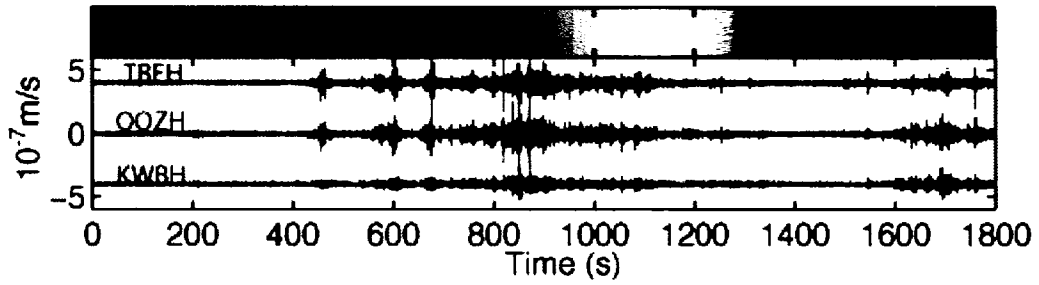
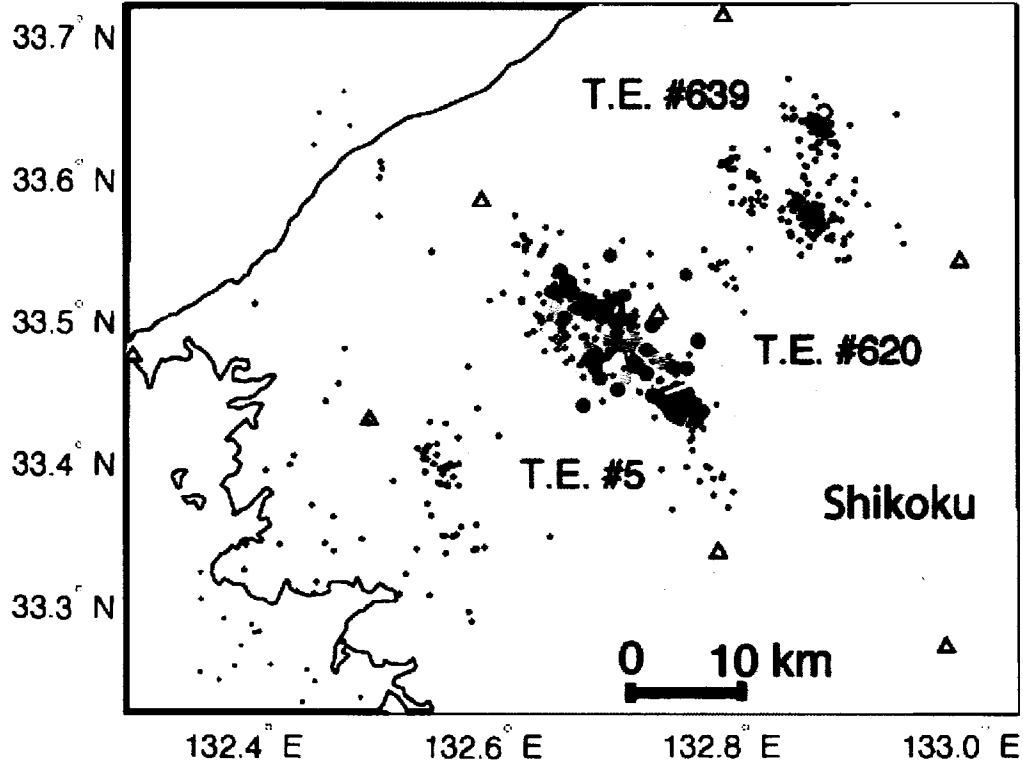


Figure 4.6. Detection of low-frequency earthquake swarms forming tremor. **a**, Map view of westernmost Shikoku showing areas active (colored circles) during the 30 minute period on August 29, 2005 beginning at 17:00, color coded with time. Only “strong” detections are shown. Note the clear spatial coherence of detected events with time. The spatial distribution of positive detections is not built into the detection algorithm, but emerges from the data. Black dots show epicentral locations of template LFEs used in this study. The depth of these events corresponds to the plate interface at 30-35 km⁶. Blue triangles denote station locations. Lower panel shows east-component waveforms at three Hi-net stations, bandpass filtered between 1 and 8 Hz. Portions plotted in red indicate times with a detected event (“strong or “weak”) similar to a template event. Inset at upper left shows the regional tectonics, with the red box indicating the area shown in the main figure. PA, Pacific plate; PS, Philippine Sea plate; AM, Amur plate; OK, Okhotsk plate. **b**, Same as **a**, but beginning September 2, 2005 at 19:00. In this episode, a clear up-dip migration of the tremor source can be seen. The locations of template events referred to in Figs. 4.3 and 4.4 are also labeled (T.E. #).

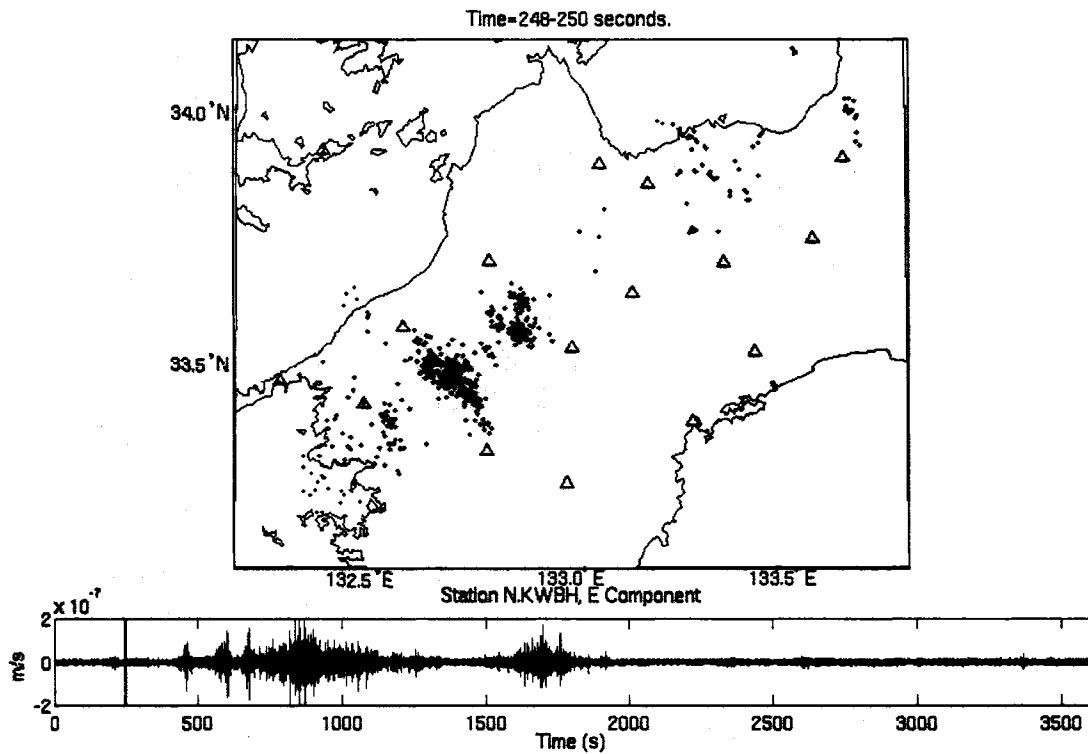


Figure 4.7. Animation showing detected events with time during non-volcanic tremor for the hour beginning September 2, 2005 at 19:00 (see enclosed CD for movie in Quicktime format). **Top panel:** Map view of western Shikoku region. Template events are plotted as small black crosses. Colored circles represent a detected event. Filled circles represent “strong” detection (no time shift allowed between stations relative to template event) while open circles represent a “weak” detection (time shift of up to 0.4 s allowed). The shade of the circle represents the robustness of the detection, with light orange a detection just above the threshold level and bright red a detection at 2 or more times the threshold. Each frame represents 2 seconds, with only the strongest detection per frame plotted. The symbols are plotted in reducing size and shading toward black for 3 frames beyond the detection time in order to guide the eye. Blue triangles show station locations; the filled triangle indicates the station with waveforms plotted in the bottom panel. The time listed at the top corresponds to the approximate time of the first S-wave arrival at any station. **Bottom panel:** A sample velocity waveform, one hour in duration, corresponding to the time-period of the animation. Waveform is bandpass filtered between 1 and 8 Hz. Portions plotted in red indicate times with a detected event similar to a template event. Note that nearly all high-amplitude segments of the waveform are matched by LFEs. The vertical blue bar indicates the point in time represented in the map view.

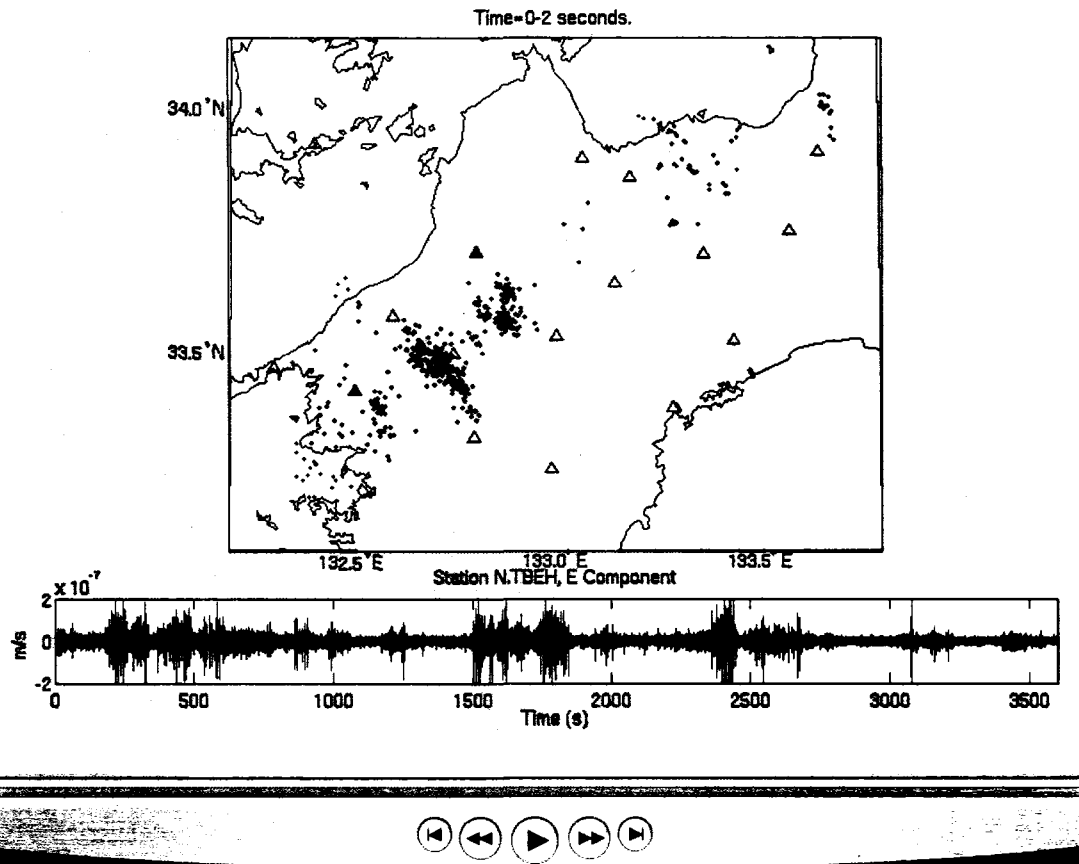


Figure 4.8. Same as Supplementary Movie 1 but for the hour beginning August 29, 2005 at 17:00 (see enclosed CD for movie in Quicktime format). In this case, tremor is active in a region distinct from that active in Supplementary Movie 1.

The dense coverage of LFE template sources in the region active in Figure 4.6b allows us to attribute the tremor source almost entirely to the sources of known LFEs. This is illustrated by the waveforms shown in Figure 4.6b, where portions explained by LFEs are plotted in red. In this case, the match between detected LFEs and tremor is nearly perfect. In the example of Figure 4.6a, previously recorded LFEs still explain the vast majority of the tremor, but occasionally weak tremor occurs without LFE detections. This likely reflects the main limitation of our technique – the uneven distribution of our LFE template sources. Since we only have template LFEs in places that, at least occasionally, rupture energetically enough to produce an identifiable phase across many stations, some areas of the fault may generate weak tremor without producing “template-strength” LFEs. In these instances, tremor may be generated too far from a template event to register as a positive detection, even though it may be occurring as a weak LFE. The relatively sparse coverage of the region active in Figure 4.6a by template LFE events supports this interpretation.

The heterogeneous distribution of LFEs (Fig. 4.6) likely reflects properties of the plate boundary. Clusters of relatively strong LFEs may occur in places of geometric or compositional variations where the fault sticks and slips as part of much larger scale slow slip transients - a process analogous to that proposed for some foreshock sequences [Dodge et al., 1996] or earthquake swarms [McGuire et al., 2005; Vidale and Shearer, 2006] in other environments. In this case, high fluid pressure on the plate boundary could allow slip to occur under low shear stress, resulting in relatively slow rupture and slip velocities (compared with ordinary earthquakes) and a corresponding deficit in high frequency energy (Fig. 4.2).

Using previously recorded and located LFEs as template events, we have established that tremor in Shikoku can be regarded as a swarm of LFEs and thus is generated by a series of small shear slip events on the plate boundary. Our approach allows us to track the source of tremor with unprecedented temporal and spatial resolution, and hence may provide similar precision in monitoring slow slip. Such behavior bears

careful watching, as slow slip transients can load adjacent locked portions of the fault and increase the probability of large damaging earthquakes.

METHODS

We search continuous waveform records during non-volcanic tremor activity for events similar to previously recorded and located LFE “template events” using a matched-filter technique. A matched filter is recognized as an effective means of detecting a known signal in the presence of noise and is extremely powerful when applied simultaneously across multiple stations [Gibbons and Ringdal, 2006]. For this study, we use waveforms from Japan’s Hi-net high sensitivity borehole seismic network operated by the National Research Institute for Earth Science and Disaster Prevention (NIED). As template events, we select 677 low-frequency earthquakes (LFEs) occurring between June 2002 and June 2005; these events represent the best recorded of those located by Shelly et al. [2006], with at least 6 three-component Hi-net stations (18 channels) recording each event. This criterion helps ensure that each template event is well located and maximizes our ability to detect any similar events within the continuous data in the presence of noise.

We search tremor episodes systematically for events resembling these template events by cross-correlating corresponding stations and components between the template events’ *S*-waves and continuous data. For each template event at each station, we use 4 seconds of the waveform, starting 1 second before the *S*-wave arrival time estimated by the Japan Meteorological Agency (JMA) at that station. We selected this waveform length and positioning in order to be sure to capture the main *S*-wave arrival (the strongest arrival) of the template LFE, without including too much of the waveform that may be dominated by noise or other sources. All waveforms are bandpass filtered between 1 and 8 Hz. We calculate the correlation coefficient as a function of time, shifting the window in increments of 0.05 seconds through the continuous waveforms (see Figs. 4.3 and 4.4). At each point we compute the sum of

the correlation coefficients across all channels. This provides a measure of waveform similarity that is insensitive to the absolute amplitude of the input signal. The same procedure is repeated for each template event.

When the correlation sum exceeds the threshold, we record a “strong” detection. Because all stations are considered simultaneously, the detected event must originate from nearly the same position as a given template event, with nearly the same source mechanism. At times, multiple nearby template events may detect the same event in the data; in this case we assign the location of the detected event to the location of the template event that registers the most robust detection. The detection robustness is calculated as the ratio between the correlation sum and the detection threshold.

We also attempt to detect events slightly offset from our template events by allowing a slight shift (0.4 s) in waveforms between stations compared to the pattern of the template event. In this case, we take the maximum correlation coefficient from the 0.4-second window at each station before summing. This scheme compromises noise tolerance in order to detect events over a slightly wider area. We maintain this “weak” detection separately from the “strong” detection (with no allowed shift) described above. For the weak detection, the threshold is set at 9 times the median absolute deviation of the distribution above the median.

Using these methods, we observe peaks in the correlation sum when the continuous tremor data exhibits similar waveforms across stations/components. We use the absolute value of the correlation sum as our detection statistic. To define a detection threshold we use the median absolute deviation (MAD), which is defined as the median of the absolute values of the deviations about the median [Rousseeuw and Leroy, 2003]. MAD is an estimator of the variability in a distribution that is robust with respect to outliers, which in this case would correspond to positive detections. For a normally distributed random variable the standard deviation is $1.4826 \times \text{MAD}$. We set a conservative threshold for a positive detection at 8 times MAD, which corresponds to approximately 5.4 sigma above the mean for the normal case. This

level was chosen to suppress spurious detections while retaining as many legitimate detections as possible. The probability of exceeding 5.4 sigma for a normally distributed random variable is approximately 3.3×10^{-8} . In a 1-hour period, we sample 72,000 time steps for each of 677 template events, giving an expectation of about 1 false detection of a “strong” event per hour. By contrast, we record 1288 “strong” detections during August 29, 2005 17:00-18:00 and 767 “strong” detections during September 2, 2005 19:00-20:00.

The correlation sums, which we use as the detection statistic, are not independent. Moreover, there may be other correlations in the data that lead to non-Gaussian behavior. For these reasons we use a synthetic test to examine the performance of the LFE detection algorithm under controlled conditions. This test works identically to our normal detection procedure, using the actual data but with stations and components randomized. Instead of correlating the template event waveforms among corresponding stations and components, waveforms are correlated with those from a different station. The stations are randomized among those recording the event, with the randomization different for each template event but kept the same during the time-period of interest. Using this procedure for ten complete runs of all 677 template events over a 1-hour period of tremor, we recorded an average of 0.4 “strong” detections and 1.2 “weak” detections per hour, thus confirming an extremely low level of spurious detections.

Applying these procedures, we detect events within continuous tremor many times weaker than our (already weak) template events and can tolerate some degree of interference from multiple, concurrent sources. To examine our detection capability, we perform another synthetic test. In this test, we take a template event not active during a particular hour of tremor and add a scaled-down version of it repeatedly over the 1-hour period. An important benefit of this technique is that it includes the noise of the real data and also tests the ability of the detection algorithm to register a detection when other events are present in the data. An example of such a test is

shown in Figure 4.5, where template event #83, located close to but not in the active region in this example, is scaled by 1/10 and then added into the real tremor sequence every 100 seconds. We then perform our normal detection procedure on the “modified” tremor. This test confirms a remarkable detection capability, with 34 of 35 of the events successfully detected – a type II error rate of less than 5%. Occasional “leakage” of detections to very nearby template events provides an estimate for our location uncertainty of ~3 km.

ACKNOWLEDGEMENTS

This material is based upon work supported by the National Science Foundation. We thank Sho Nakamura for assistance with the Hi-net data. All data were obtained from the NIED Hi-net data server.

REFERENCES

- Ando, M. A fault model of the 1946 Nankaido earthquake derived from tsunami data. *Phys. Earth Planet. Int.* **28**, 320–336 (1982).
- Dodge, D. A., Beroza, G.C. & Ellsworth W. L. Detailed observations of California foreshock sequences: implications for the earthquake initiation process, *J. Geophys. Res.*, **101**, 22,371-22,392 (1996).
- Dragert, H., Wang, K., & Rogers, G. Geodetic and seismic signatures of episodic tremor and slip in the northern Cascadia subduction zone, *Earth Planets Space*, **56**, 1143-1150 (2004).
- Gibbons, S. J. & Ringdal, F. The detection of low magnitude seismic events using array-based waveform correlation. *Geophys. J. Int.* **165**, 149-166 (2006).

- Hirose and Obara, K., Repeating short- and long-term slow slip events with deep tremor activity, around the Bungo channel region, southwest Japan, *Earth Planets Space*, **57**, 961–972 (2005).
- Ide, S., Shelly, D. R., & Beroza, G. C. The mechanism of deep low frequency earthquakes: further evidence that non-volcanic tremor is generated by shear slip on the plate interface. *Geophys. Res. Lett.*, in press.
- Kao, H. et al. Spatial-temporal patterns of seismic tremors in northern Cascadia. *J. Geophys. Res.*, **111**, doi:10.1029/2005JB003727 (2006).
- Kao, H., Shan, S.-J., Dragert, H., Rogers, G., Cassidy, J. F. and Ramachandran, K. A wide depth distribution of seismic tremors along the northern Cascadia margin, *Nature*, **436**, 841-844 (2005).
- Katsumata, A., and Kamaya, N., Low-frequency continuous tremor around the Moho discontinuity away from volcanoes in the southwest Japan, *Geophys. Res. Lett.* **30**, doi:10.1029/2002GL015981 (2003).
- McGuire, J. J., Boettcher, M. S., & Jordan, T. H. Foreshock sequences and short-term earthquake predictability on East Pacific Rise transform faults. *Nature* **434**, 457-461 (2005).
- Nadeau, R. M. & Dolenc, D. Nonvolcanic tremors deep beneath the San Andreas fault. *Science* **307**, 389 (2005); published online 9 December 2004 (10.1126/science.1107142).
- Obara, K. Nonvolcanic deep tremor associated with subduction in southwest Japan. *Science*, **296**, 1679 (2002).
- Obara, K., Hirose, H., Yamamizu, F. & Kasahara, K. Episodic slow slip events accompanied by non-volcanic tremors in southwest Japan subduction zone. *Geophys. Res. Lett.* **31**, doi:10.1029/2004GL020848 (2004).

Rogers, G. & Dragert, H. Episodic tremor and slip on the Cascadia subduction zone: The chatter of silent slip. *Science* **300**, 1942-1943 (2003).

Rousseeuw, P., and Leroy, A., *Robust Regression and Outlier Detection*, 360 pp., Wiley, (2003).

Shelly, D. R., Beroza, G. C., Ide, S., & Nakamura, S. Low-frequency earthquakes in Shikoku, Japan and their relationship to episodic tremor and slip. *Nature* **442**, 188-191 (2006).

Vidale, J. E. & Shearer, P. M., A survey of 71 earthquake bursts across southern California: Exploring the role of pore fluid pressure fluctuations, *J. Geophys. Res.* **111**, doi:10.1029/2005JB004034 (2006).

5. THE COMPLEX EVOLUTION OF TRANSIENT SLIP DERIVED FROM PRECISE TREMOR LOCATIONS IN WESTERN SHIKOKU, JAPAN

ABSTRACT

Transient slip events are increasingly being recognized as important components of strain release on faults and may substantially impact the earthquake cycle. Surface-based geodetic instruments provide estimates of the overall slip distribution in larger transients but are unable to capture the detailed evolution of such slip, either in time or space. Accompanying some of these slip transients is a relatively weak, extended duration seismic signal, known as non-volcanic tremor, which has recently been shown to be generated by a sequence of shear failures occurring as part of the slip event. By precisely locating the tremor, we can track features of slip evolution with unprecedented resolution. Here, we analyze two weeklong episodes of tremor and slow slip in western Shikoku, Japan. We find that these slip transients do not evolve in a smooth and steady fashion but contain numerous sub-events of smaller size and shorter duration. In addition to along-strike migration rates of ~ 10 km/day observed previously, much faster migration also occurs, usually in the slab dip direction, at rates of 25-150 km/hour. We observe such migration episodes in both the up-dip and down-dip directions. These episodes may be most common on certain portions of the plate boundary that generate strong tremor in intermittent bursts. The surrounding regions may slip more continuously, driving these stronger patches to repeated failures. Tremor activity exhibits a correlation with the tidal period, possibly reflecting the modulation of slow slip velocity by tidal stresses.

This chapter is in preparation for *G-Cubed* with co-authors G. C. Beroza and S. Ide.

INTRODUCTION

In recent years, advances in geodetic monitoring systems have led to the discovery of transient slip events in subduction zones, with durations ranging from days to years [*Hirose et al.*, 1999; *Dragert et al.*, 2001; *Ozawa et al.*, 2002]. With similar advances in seismic monitoring networks, a weak semi-continuous seismic signal, termed non-volcanic tremor, has been found to accompany some events on the shorter end of this duration range (days to weeks), with its activity approximately matching the duration and location of the slip event [*Rogers and Dragert*, 2003; *Obara et al.*, 2004]. Such “episodic tremor and slip” (ETS) events have been verified to occur in both the Cascadia and southwest Japan subduction zones. In each location, tremor and slip is concentrated down-dip of the main seismogenic zone in a region believed to be transitional between velocity weakening (stick-slip) behavior up-dip and velocity strengthening (stable sliding) down-dip.

Initially, a variety of mechanisms were proposed to explain the tremor signal, often invoking fluid flow as the tremor generating mechanism [*Obara*, 2002; *Katsumata and Kamaya*, 2003; *Seno and Yamasaki*, 2003]. Such a mechanism arose from analogies with volcanic tremor, which is thought to be generated by the movement of volcanic fluids and from the fact that fluids are expected to be liberated from the subducting slab near where the tremor is occurring. However, it is unclear how such a mechanism would account for the close correspondence now observed with transient slip events.

More recently, precise locations of relatively distinct and energetic portions of tremor, classified as low-frequency earthquakes (LFEs), revealed that these LFEs occurred on the plate interface, coincident with the estimated zone of slow slip [*Shelly et al.*, 2006]. Based on the LFE locations and the character of their waveforms, the authors of this study proposed that LFEs may be generated directly by shear slip as part of the slip transients. This interpretation is supported by *Ide et al.*, [2007a], who used stacked LFE waveforms to constrain the LFE’s mechanism. They found that LFE P-

wave first motions and an empirical moment tensor inversion using LFE S-waves both yielded mechanisms supporting shear slip on the plate interface in the direction of plate convergence. Meanwhile, *Shelly et al.*, [2007] demonstrated that tremor could be explained as a swarm-like sequence of LFEs occurring on the plate interface. This study established that tremor itself is generated by shear slip on the plate interface and in doing so demonstrated a method to locate much of the tremor activity with high precision.

An intriguing type of slip event was recently discovered to occur coincident with ETS activity in southwest Japan. These events, called very low frequency earthquakes (VLFEs), are detected in broadband data at periods of 20-50 seconds [*Ito et al.*, 2007]. They also have mechanisms consistent with shear slip in the plate convergence direction, and are intermediate between slow slip events and LFEs, both in duration and magnitude.

We now recognize that tremor/LFEs, VLFEs, and slow slip events are all members of a family of slow shear slip events occurring together in the transition zone on the subduction interface, down-dip of the seismogenic zone [*Ide et al.*, 2007b]. This family appears to exhibit scaling of moment proportional to duration, unlike regular earthquakes, which have a moment proportional to the cubed duration.

This new understanding of tremor allows us to use precise tremor locations to examine the evolution of slow slip events. Although geodetic measurements can now resolve average properties of larger slow slip events, they cannot provide information on detailed temporal or spatial evolution of slip. Because of this, the slip in these events has often been assumed to evolve in a relatively steady fashion. We find that in western Shikoku, slow slip is a complex occurrence, likely influenced by variable frictional properties on the plate interface. Precise tremor locations give us the ability to resolve slip on a time scale of seconds, rather than days, and a spatial scale of ~ 1 km, rather than 10s of kilometers. Although we are limited by the locations of our LFE template sources, we can locate tremor (and thus slip) in these zones very

precisely and can infer the behavior of surrounding regions. Such information could greatly assist our understanding of the physical processes controlling slow slip.

METHODS

In this study, we use the method described in *Shelly et al.* [2007] to examine the detailed evolution of slip during two, weeklong ETS episodes in western Shikoku that occurred during January and April 2006. This method uses the waveforms of previously located LFEs [*Shelly et al.*, 2006] as “template events” and systematically searches continuous tremor for instances where the tremor waveforms strongly resemble the waveforms of a previously recorded LFE. The similarity is measured by the sum of the correlation coefficients across all available channels of data. By utilizing multiple stations and components in the network simultaneously this matched-filter approach becomes extremely powerful for detecting a known signal in noisy data [*Gibbons and Ringdal*, 2006; *Shelly et al.*, 2007].

We adjust the template event selection and detection threshold parameters used in *Shelly et al.* [2007] slightly. For this study, we use continuous data from eight, three-component Hi-net stations in western Shikoku. As “template events”, we select each LFE [*Shelly et al.*, 2006] recorded by at least five of these eight stations, giving a minimum of 15 channels of data for each template event. This selection criterion gives 609 LFE template events and ensures both that these are well located and that they have sufficient data to allow detection of similar events within the continuous tremor waveforms.

As in *Shelly et al.* [2007], we adopt a detection threshold based on the median absolute deviation (MAD) of the distribution of correlation sums. Our standard detection threshold is set at $8 \times \text{MAD}$ and is set independently for each template event and each day of continuous seismic data. At this threshold, based on statistical arguments supported by synthetic tests [*Shelly et al.* 2007], we estimate the false detection rate to be about 1 per hour (total over all 609 template events). Sometimes, we consider a

“very robust” detection threshold of $9 \times \text{MAD}$. This very high detection threshold (probability of exceedance of $\sim 6.4 \times 10^{-10}$ for a Gaussian distribution) sacrifices many legitimate detections but virtually eliminates spurious detections. With this detection threshold, we expect our false detection rate to be less than one event per day.

RESULTS AND DISCUSSION

We examine two ETS episodes occurring in western Shikoku during January and April 2006. Figure 5.1 shows the regional tectonics and location of our study area, as well as the epicenters of our template LFEs. Tilt data and the associated slip model for the April event, as determined by *Sekine and Obara* [2006], are shown in Figure 5.2. For this event, they estimate a moment magnitude $M_w = 6.0$, and an average of 1.2 cm of slip, based on the tilt change at multiple stations during a three-day period from April 17-20. However, no geodetic-based slip model is currently available for the January event, as it apparently did not generate a sufficient tilt signal to enable modeling of a fault plane. This may be due to the fact that, based on our tremor locations, the January 2006 event ruptured a smaller area than the April event, extending a shorter distance to the southwest.

Figures 5.3-5.9 and 5.10-5.16 demonstrate the complex evolution of tremor and slip during the episodes of January 15-21 and April 15-21, 2006, respectively, based on precise tremor locations. For a different perspective on these episodes, please see Figures 5.17 and 5.18 and the associated Quicktime format movies included on the enclosed CD. In total, we detect 7,297 events during the January episode and 3829 events during the April episode. Of these, 3924 and 1905 events in January and April, respectively, correspond to “very robust” detections, exceeding the threshold of $9 \times \text{MAD}$ (see methods). Since these events have been shown to represent shear failure on the plate interface, we believe the locations accurately reflect portions of the plate boundary slipping at any given time. Although potential locations are limited to places where we have LFE template sources (Figs. 5.3-5.16), we can use these

locations to infer the behavior of the surrounding region as well. In fact, the locations of the LFEs themselves with their often-clustered distribution may contain information about the properties of the plate boundary.

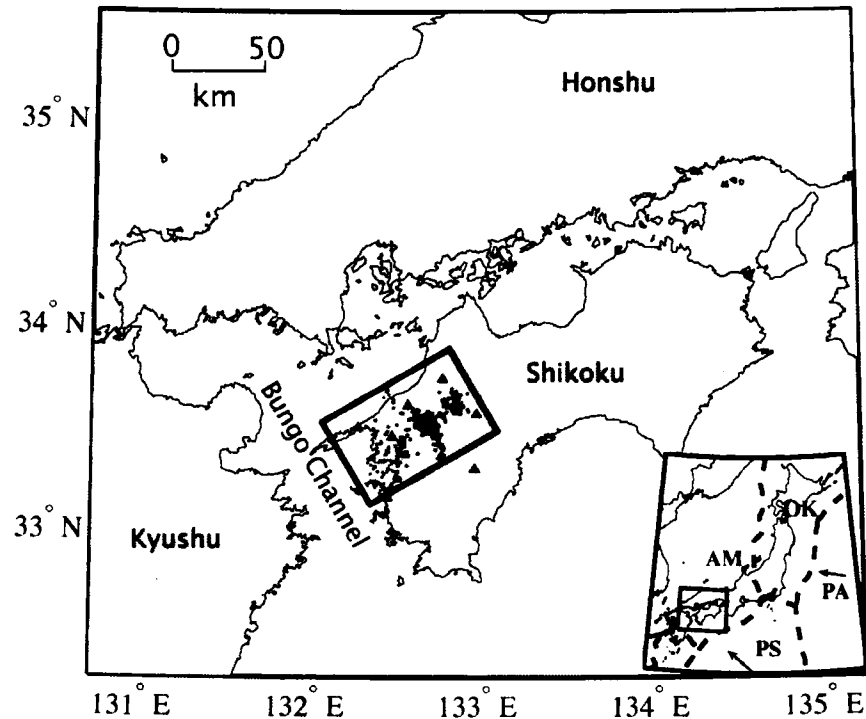


Figure 5.1. Tectonic setting and location of study area. Red box in main figure shows location of study area and denotes the region shown in Figures 5.3-5.16, parts A and B. Black dots indicate LFE template events. Blue triangles show the locations of the eight Hi-net stations used in this study. Inset shows the regional tectonics with the red box indicating the region shown in the main figure. Dashed lines indicate approximate plate boundaries. PA, Pacific plate; PS, Philippine Sea plate; AM, Amur plate; OK, Okhotsk plate.

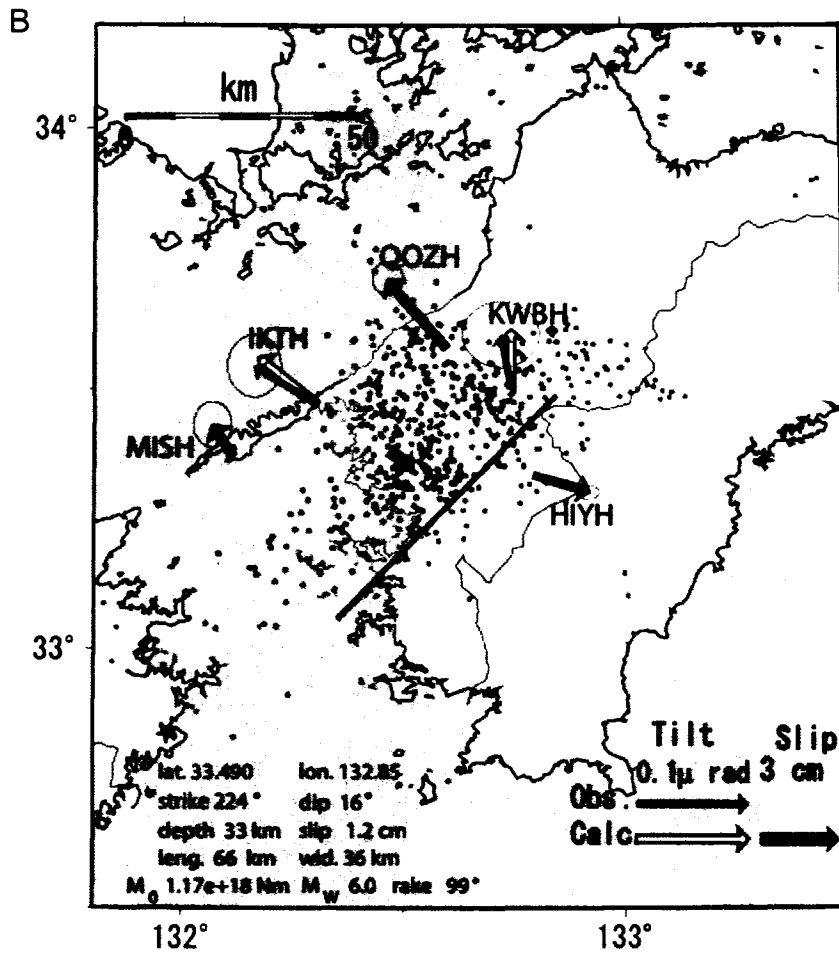


Figure 5.2. The April 2006 tremor and slip event. **A**, (from top to bottom) Time series of tiltmeter records, daily tremor counts, atmospheric pressure, and precipitation from April 10-24, 2006. Station names and components are given next to each tiltmeter record. The records are plotted after removing their linear trend and estimated tidal and atmospheric components [from *Sekine and Obara, 2006*]. **B**, Tilt change vectors (blue arrows; ground downward direction), the estimated short-term slow slip model (red rectangle area and arrow) from these tilt change data, and the calculated tilt changes due to this short-term slow slip event model (open arrows) for the western Shikoku region. Epicenters of deep low-frequency tremor activity are also plotted during the same time period (April 17-20, 2006) [from *Sekine and Obara, 2006*].

One of the characteristics obvious from Figures 5.3-5.16 is the repeated tremor (and thus slip) activity on portions of the plate interface covered by template LFEs during a given ETS episode. The repeat time of such ruptures is not regular but may be related to stresses applied from slip on neighboring portions of the fault. Such episodes often appear to rupture through an entire LFE cluster, but individual clusters rupture more or less independently. Even closely-space “subclusters” of LFEs in the northeast part of our study area (along-strike position ~60 km) often display out of phase slip from one another, while concurrently active. This behavior suggests a scenario where these LFE clusters are driven to failure by steadier slip in the surrounding region. These clusters may be places with frictional properties different from those of the surrounding material or may represent some sort of geometrical heterogeneity. Under this scenario, these clusters may be analogous to repeating earthquake patches, which are believed to be portions of the fault that exhibit unstable slip surrounded by a stably slipping region [Schaff *et al*, 1998]. As in the case for repeating earthquakes, the repeat time of rupture may be related to slip rates in the surrounding region [Nadeau and McEvilly, 1999]. However, the slip episodes in this case proceed over a matter of minutes, rather than seconds as for a comparable earthquake.

MIGRATION OF TREMOR AND SLIP:

We observe two classes of migration of ETS activity: a relatively slow migration along-strike and a much faster migration usually observed in the dip direction of subduction. Previous investigators have observed that ETS episodes often exhibit along-strike migration rates of approximately 5-20 km/day [Obara, 2002; Dragert *et al.*, 2004; Kao *et al.*, 2006]. We observe a similar migration trend, although somewhat sporadic, in both the January and April events. In January the along-strike migration is mostly unilateral, whereas in April migration occurs bilaterally. However, overprinted on this slow average migration is much more complex short-term

behavior, where we see the portions of the fault that generate strong tremor (LFEs) rupturing repeatedly.

Using precise tremor locations, we can now resolve much higher rates of migration of tremor and slip than those previously observed. The clearest of these migrations occur in approximately the dip direction at $\sim 20\text{-}150$ km/hour, as highlighted in Figures 5.3-5.16. Occasionally, migration at similar rates can also be seen in the along-strike direction. These rates are 40-300 times faster than a typical long-term along-strike migration rate of ~ 12 km/day. However, they are still approximately 3 orders of magnitude slower than ordinary earthquake rupture velocities. These migrations are easiest to observe in the LFE cluster located at an along-strike position of ~ 40 km, where rupture commonly propagates ~ 15 km along-dip in ~ 15 minutes. If the scaling relationship proposed by *Ide et al.* [2007b] is applicable to these events, such episodes would be expected to have a moment magnitude of approximately $M_w=4.3$, falling between VLFES and slow slip events in size and duration.

In different along-dip episodes, the migration direction can be up-dip, down-dip, or bilateral. The down-dip migration examples, combined with very high migration rates, make it unlikely that fluids migrate with this slip. Instead, the events are most likely triggered by stresses accumulating from slower, steadier slip in the surrounding region. This larger-scale, more-continuous slip appears to grow slowly in size, controlling the along-strike migration, while the smaller-scale events grow much more quickly, consistent with the scaling relationship proposed by *Ide et al.* [2007b].

We rarely observe clear examples of fast migration along strike. Although gaps in our distribution of template LFEs often make it difficult to recognize along-strike migration if it propagates for less than 10 km, we can conclude that larger-scale episodes are rare. For example, even though the large LFE cluster near the center of our study area (along-strike position of ~ 40 km), sometimes ruptures its entire length of nearly 20 km, such episodes do not generally propagate to neighboring LFE clusters along strike, even though they may be quite nearby.

A notable exception occurred on April 19, 2006 and is shown in Figure 5.14, part E. This particular example migrates to the northeast 50 km along strike over a period of 2.5 hours, an average rate of 20 km/hour. If this episode did not extend significantly outside our study region, the scaling relationship of *Ide et al.* [2007b] would suggest a magnitude near $M_w=5.0$. This fast along-strike migration episode is superimposed on top of a slowly migrating tremor front and likely represents a propagating pulse of faster slip within the larger transient slip event. Although the physical dimensions of the event may play a role [*Ide et al.*, 2007b], the processes controlling these two very different migration rates are not well understood.

Segmentation of the fault may inhibit extensive propagation of “fast” pulses of slip along strike. This segmentation could be due to small geometrical irregularities, which would be expected to align in the direction of slip (similar to the slab dip direction) over time. In fact, a corrugation of the fault may also influence the distribution of LFE template sources, which are sometimes located in clusters approximately aligned with the plate convergence direction. This phenomenon could be related to streaks of seismicity aligned in the slip direction observed on creeping faults elsewhere [*Rubin et al.*, 1999; *Waldhauser et al.*, 2004]. In the case of our study area, the plate boundary appears more strongly segmented to the northeast than the northwest. Apparently, only the larger, slower “main event” is readily capable of overcoming this segmentation.

For both slow and fast migration, the onset of activity is usually much sharper than the ceasing of activity on a given portion of the fault. These trailing events could be considered “aftershocks” of the major sequence of activity - they may be due to residual stresses or simply indicate a fault weakened immediately after rupture that heals over time.

RELATIONSHIP TO VERY LOW FREQUENCY EARTHQUAKES

Ito et al. [2007] found VLFES coincident with ETS activity in southwest Japan and identified four such events occurring as part of the ETS episodes examined here. All

four occurred on April 18, 2006; their reported locations and timing relative to our tremor locations are shown by the open circles in Figure 5.13. The magnitudes of these four events were estimated to range from $M_w=3.2$ to $M_w=3.5$, with durations on the order of 10 seconds. Although we clearly see tremor activity in the vicinity of the reported VLFs before and after their occurrence, such activity is unremarkable compared to other times when VLFs were not reported. The relatively small size and short duration of these events combined with somewhat sparse template LFE coverage in the vicinity of the VLFs probably explain this lack of signal.

TIDAL TRIGGERING OF TREMOR AND SLIP

Tremor activity observed in the January 2006 event exhibits a strong periodicity at slightly more than 12 hours, very similar to the average tidal period of 12.4 hours. The effect is so strong it can be seen visually in Figures 5.3-5.9. Figure 5.19 evaluates this periodicity statistically based on Schuster's test, which is often used to test statistical significance of tidal triggering of earthquakes [i.e. *Tanaka et al.*, 2002; *Cochran et al.*, 2004]. For each event, Schuster's test assigns a unit vector in the direction defined by its phase angle. The squared length of the vectorial sum for all events, D^2 , is given by

$$D^2 = \left(\sum_{i=1}^N \cos \theta_i \right)^2 + \left(\sum_{i=1}^N \sin \theta_i \right)^2$$

where θ_i is the phase angle of the i th event and N is the total number of events. Assuming the events occur randomly and independently, the probability of obtaining a vectorial sum equal to or greater than D is

$$P = \exp\left(-\frac{D^2}{N}\right)$$

Therefore, $1-P$ represents the significance level to reject the hypothesis that the events occur randomly. Assuming a period of 12.4 hours, we obtain P values of 2×10^{-655}

and 6.7×10^{-66} for the January and April events respectively. In our case, because of the strong clustering of events in time, their occurrence is not independent and P likely overestimates the significance somewhat. However, these incredibly small numbers are some indication of the strong tidal effects in this dataset supported by relatively large numbers of events in our dataset. For comparison, P values of 10^{-4} have been considered extremely significant for tidal triggering of earthquakes [Cochran *et al.*, 2004].

Figure 5.19 plots D^2/N , the argument of the exponential in Schuster's test, versus tested period. For both episodes, phase angles are assigned starting with 0 and ranging to 2π , repeating with the period to be tested. Figure 5.19 shows an incredibly strong peak at just over 12 hours for the January event. The actual peak occurs at 12.2 hours, slightly shorter than an average tidal period of 12.4 hours, but consistent with the average tidal period during this particular time span, as evidenced by nearby sea-tide records. Peaks in tremor activity levels correspond to during and shortly after the high tide recorded on the Pacific coast of Shikoku. The April episode also exhibits a strong peak near a period of 12 hours, although the effect is subtler than for the January event. Figure 5.20 shows histograms of event abundance versus phase angle for the two episodes, assuming a period of 12.4 hours.

Although we do not attempt to calculate the tidally induced stress, previous studies have emphasized the importance (and often domination) of ocean tide loading effects relative to solid earth tides when near ocean basins [Tsuruoka *et al.*, 1995, Cochran *et al.*, 2004]. Ocean loading probably plays an important role in this case, with high tide likely serving to reduce the coupling force between the subducting and overriding plates by exerting a downward force on the subducting plate. The depth of the triggered events in this study (generally 30-35 km) means that the tidal stress is extremely small compared with the confining pressure, although near-lithostatic pore pressures may serve to mitigate the effects of this depth by greatly reducing the effective normal stress on the fault. Tidal triggering of tremor has also been reported

in eastern Shikoku [Nakata *et al.*, 2006], indicating that this behavior may be relatively common. A likely scenario is that tidal forces modulate the slip velocity in the region surrounding the LFE clusters, generating an increased LFE/tremor activity level during times when the slip rate in the surrounding region is accelerated.

The lunar period may also have the potential to affect tremor and slip activity. The January and April events apparently begin on the 15th of the month (90 days apart), while another minor tremor episode in this region has been reported to begin approximately the same time of the month in February [Obara *et al.*, 2006], about 30 days after the January event and 60 days before the April event. Although only suggestive, these intervals correspond closely with the 29.5-day lunar cycle.

IMPLICATIONS FOR THE MECHANICS OF TREMOR AND SLIP

Although tremor appears to be generated by shear slip, fluids may play an important role in enabling such slip. This idea is supported by tomographic and seismic reflection studies suggesting high fluid pressures may be present in the tremor and slow slip zone [Shelly *et al.*, 2006; Kodaira *et al.*, 2004]. Kodaira *et al.* [2004] proposed that high fluid pressure could enable transient slip by extending the conditionally stable region between zones of velocity weakening up-dip and velocity strengthening down-dip.

Modeling studies also indicate that near-lithostatic fluid pressures may promote transient slip behavior [Liu and Rice, 2007], even without time-varying properties [Liu and Rice, 2005]. An alternate possibility is the existence of a transition in friction properties from velocity weakening behavior at very low slip speeds to velocity strengthening at higher velocities as modeled by Shibasaki and Iio [2003]. Observed triggering of tremor, both by seismic waves from distant earthquakes [Miyazawa and Mori, 2005; 2006] and by tidal forces, further suggests that fluids play a role in this process, and that the system may be sensitive to small perturbations in fluid pressure.

CONCLUSIONS

Strong evidence supports the notion that non-volcanic tremor, at least in western Shikoku, is generated by shear slip on the plate interface. These micro-slips do not generally occur in isolation but rather in swarms as a cascade of shear failure along the plate boundary. The slip from these events clearly contributes the geodetically detected slip and thus slow slip and tremor can be considered essentially different manifestations of a single process. However, strong tremor activity is concentrated at certain areas of the plate boundary, where some heterogeneity in fluids, mineral properties, and/or geometry likely exists. As a result, these zones stick and slip as they are driven by slip in the surrounding region. Activity within one tremor cluster often propagates through the cluster, but takes a matter of minutes, rather than seconds as for a comparable earthquake rupture. Areas of the plate boundary between these strong tremor patches may slip while generating only weak (and possibly undetectable) tremor.

Slow slip does not evolve smoothly, but rather contains of a series of sub-events. These sub-events are pulses of more rapid slip, such as the VLFs reported by *Ito et al.* [2007]. We also infer somewhat larger, slower sub-events from precise tremor locations, propagating primarily in the along-dip direction at velocities of 20-150 km/hr. The relative scarcity of these sub-events extending a significant distance along strike may be due to fault segmentation, possibly reflecting a “grain” of the plate interface oriented in the dominant slip direction. In addition, tremor activity often demonstrates strong tidal periodicity, possibly reflecting the modulation of overall slip velocity of the transient event by tidal forces. This observation suggests that the high confining pressure expected at this depth is mitigated by near-lithostatic fluid pressure, resulting in very low effective normal stress on the plate interface.

Figures 5.3-5.9. Space-time progression of tremor during January 15-21, 2006. Date is given by figure heading. **a**, Map view showing active LFE template events (colored circles) during the first half of each day (0:00-12:00 JST). The color scale indicates the along-strike position, for reference when comparing with part c. Only very robust detections exceeding $9 \times \text{MAD}$ (see text) are plotted. If multiple detections are present, the strongest in each 2-second window is plotted. Black dots show epicentral locations for LFE template sources. Blue triangles indicate the locations of Hi-net stations used in this study, with the solid triangle showing station N.KWBH referred to in part d. The black line is the coastline of Shikoku. **b**, Same as part a, but for the second half of each day (12:00-24:00 JST). **c**, Down-dip position of tremor versus time. Events are color-coded by along-strike position as in parts (a) and (b). Arrows and labels indicate the direction and approximate migration velocity for some of the clearest examples of migration. Notice the migration of tremor that can be seen in both the updip or downdip directions. **d**, Seismic waveform from station N.KWBH, north component (location shown in part a). Portions of the waveform plotted in red indicate times of very robust detections (exceeding $9 \times \text{MAD}$) while portions plotted in pink indicate times with standard detections (exceeding $8 \times \text{MAD}$ or 0.4 second time shift between stations allowed with $9 \times \text{MAD}$ - see text for details). A relatively steady, low-amplitude signal seen around mid-day and uncorrelated with LFEs does not appear to be non-volcanic tremor, as neighboring stations do not record a similar signal.

Figures 5.10-5.16. Same as figures X, but for April 15-21, 2006. Open circles in parts b and c during April 18 (Fig. 5.13) indicate the occurrence of VLFs, as reported by Ito et al. [2006]. **e**, (Fig. 5.14 only) Along-strike position of tremor versus time.

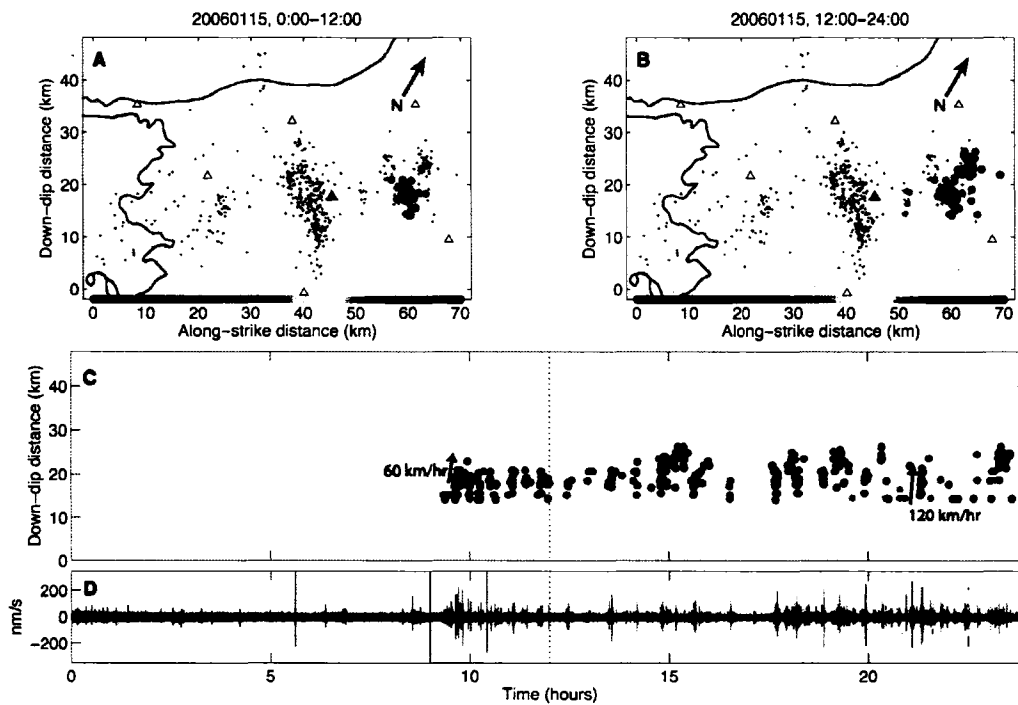


Figure 5.3

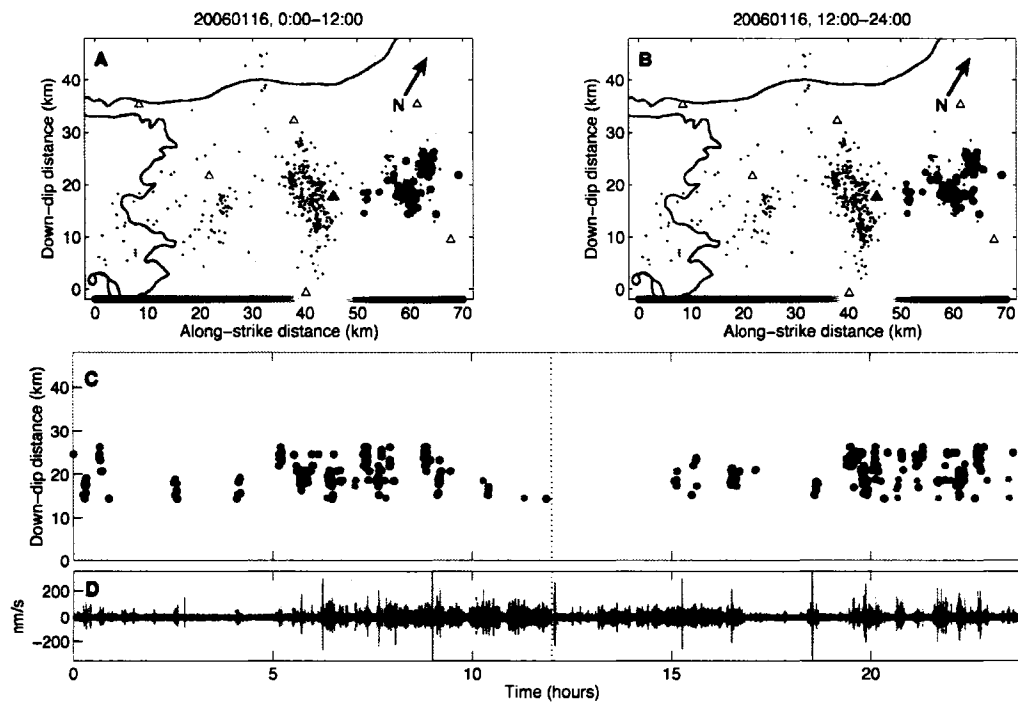


Figure 5.4

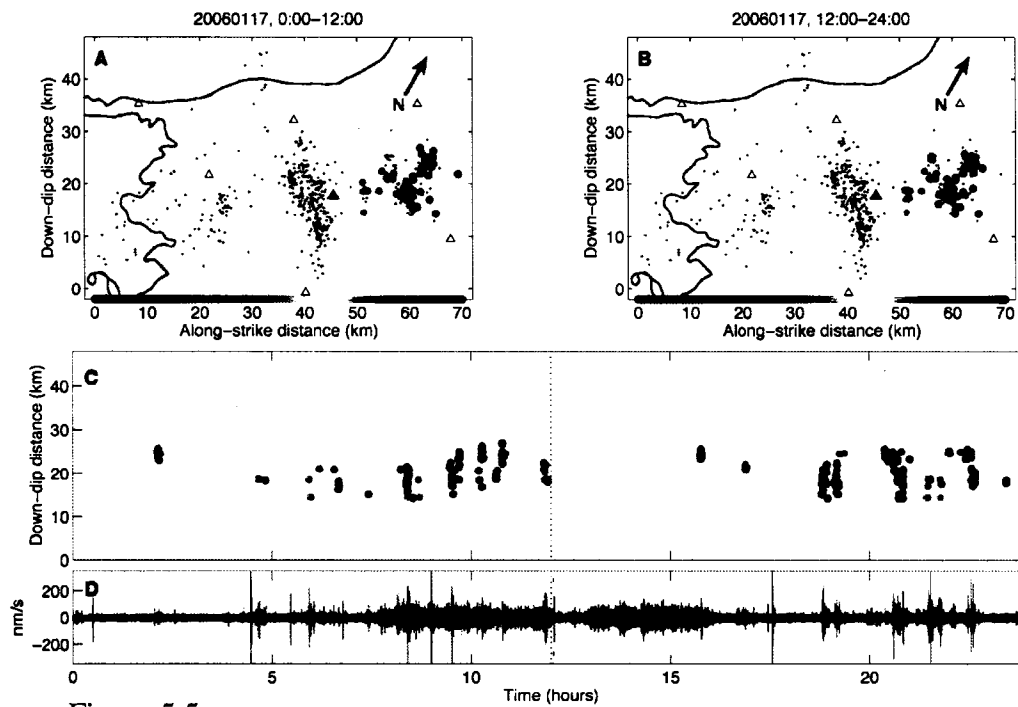


Figure 5.5

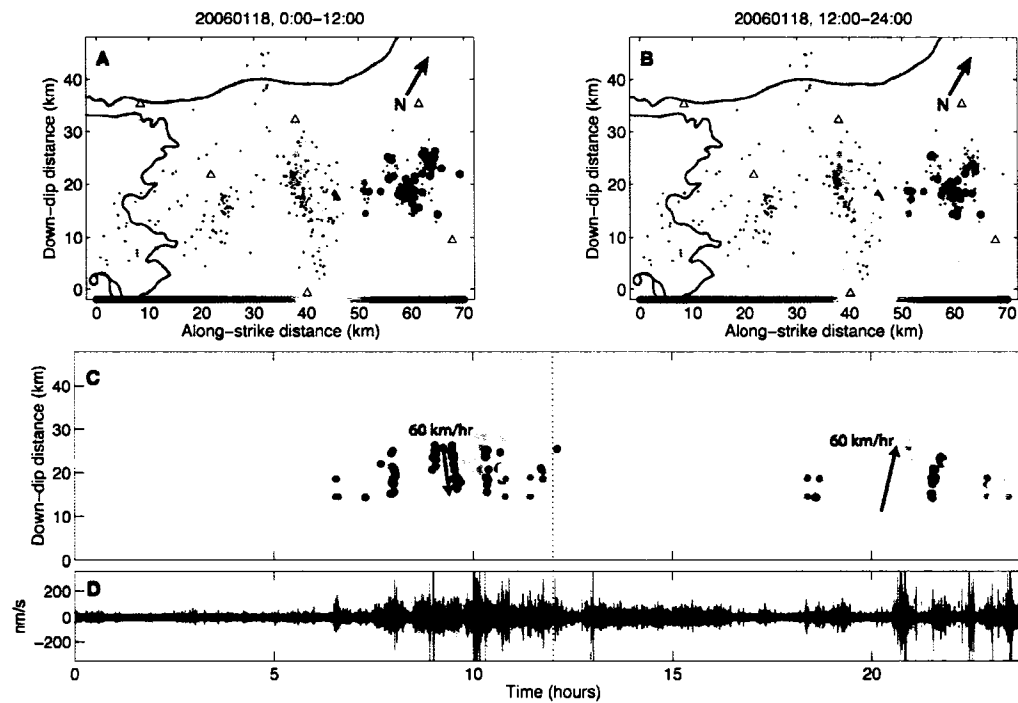


Figure 5.6

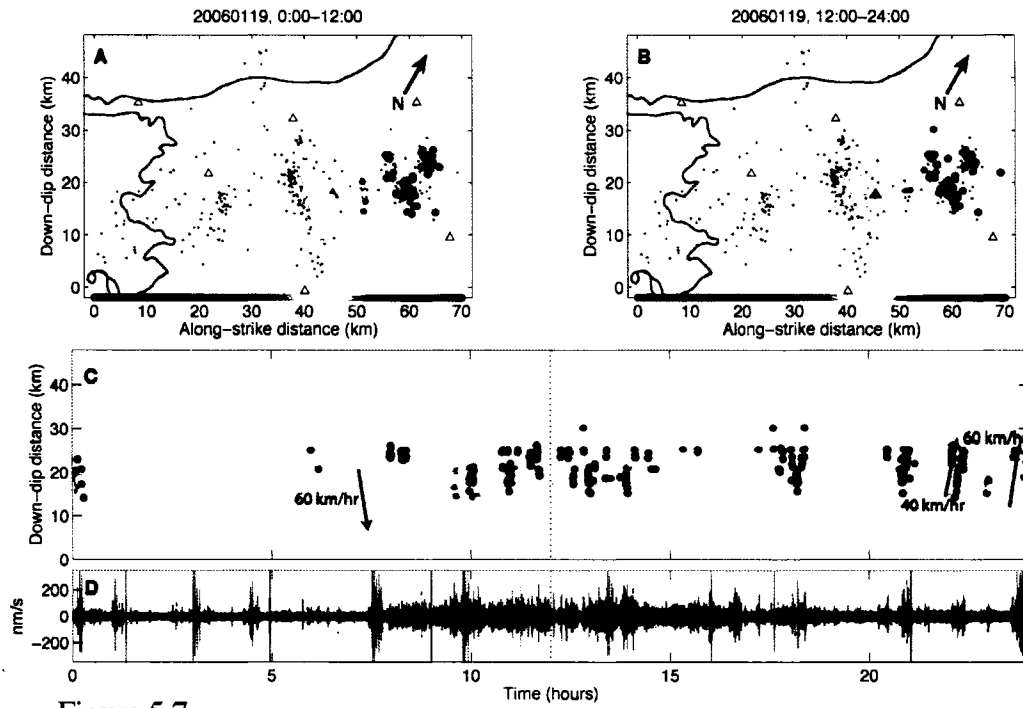


Figure 5.7

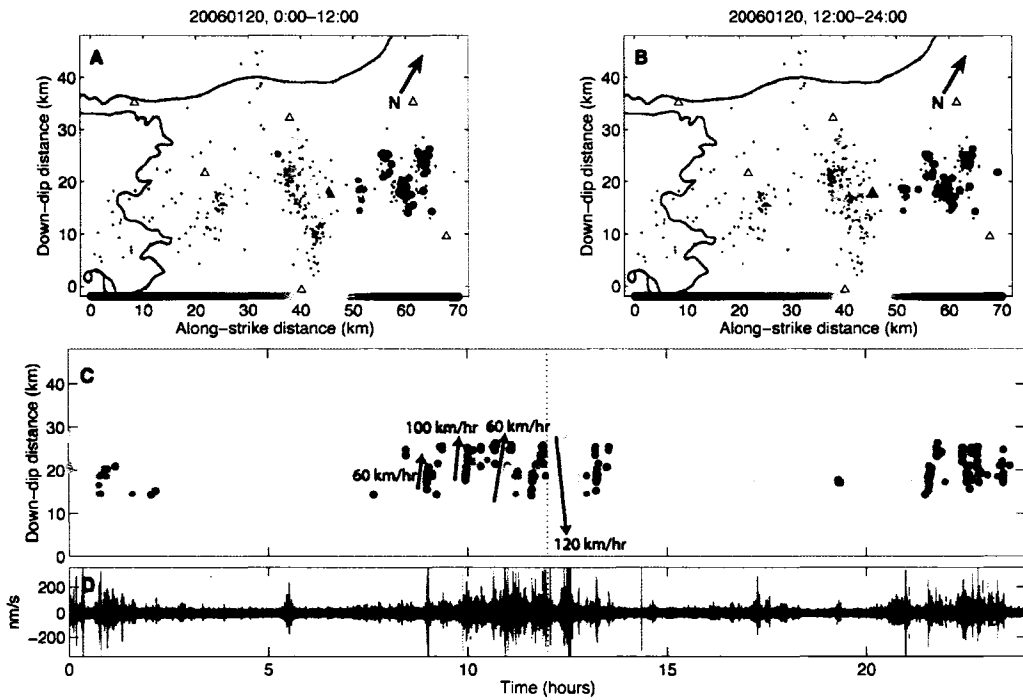


Figure 5.8

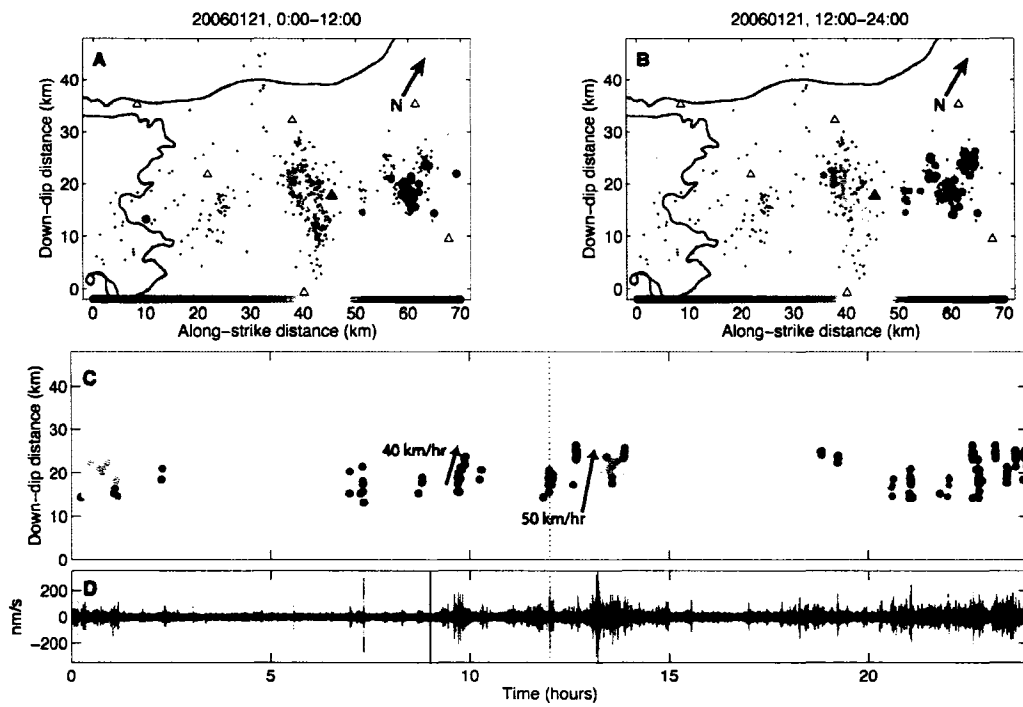


Figure 5.9

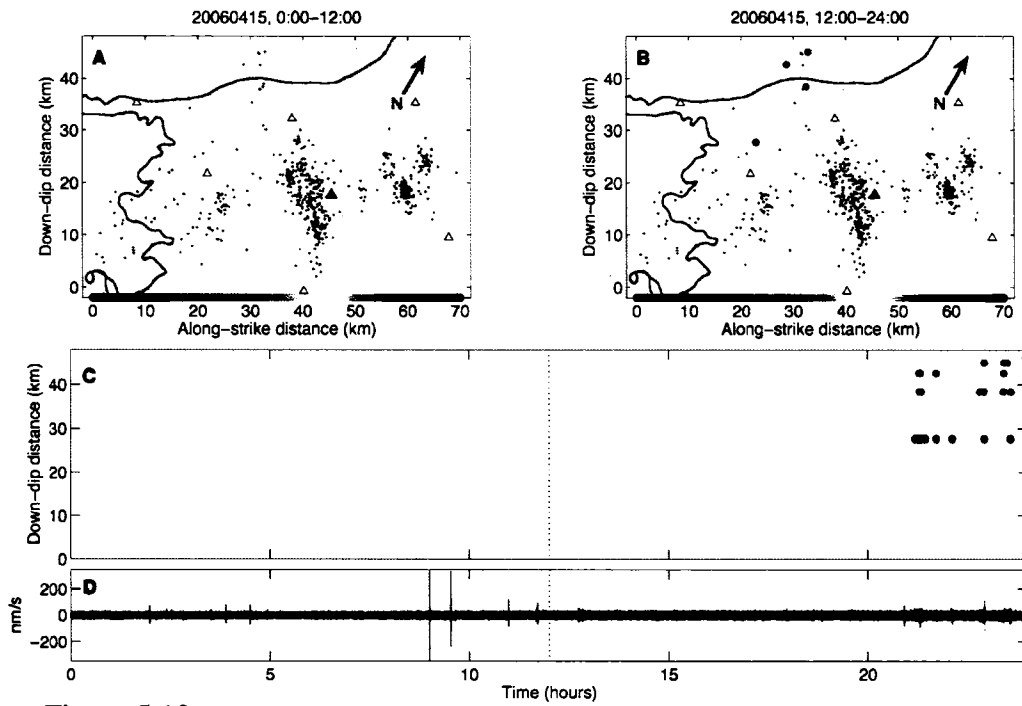


Figure 5.10

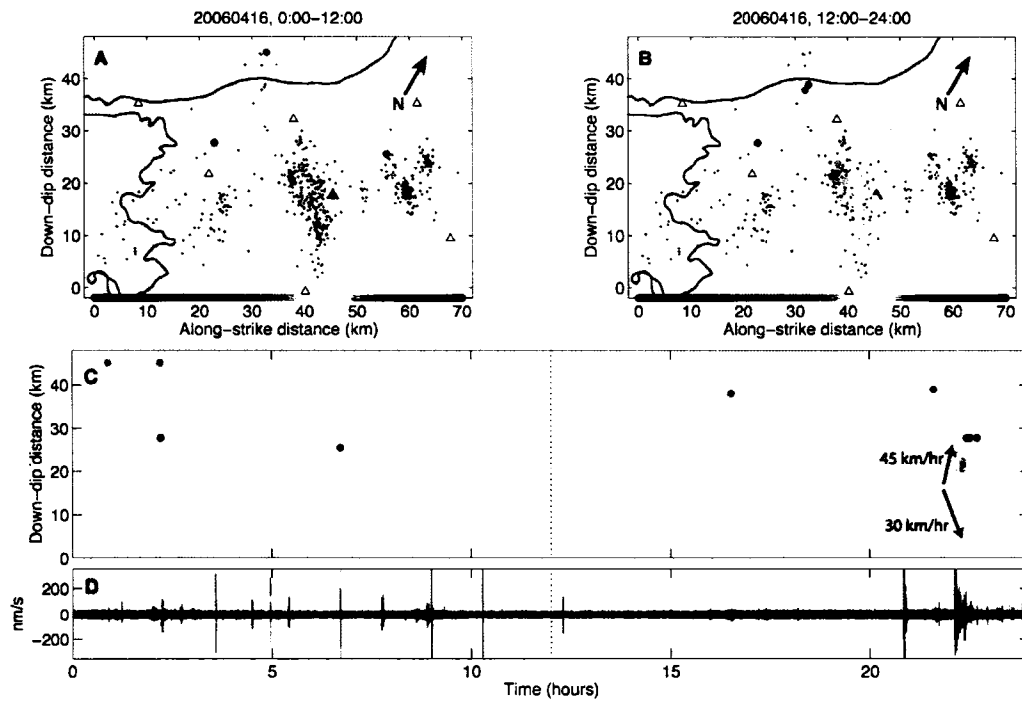


Figure 5.11

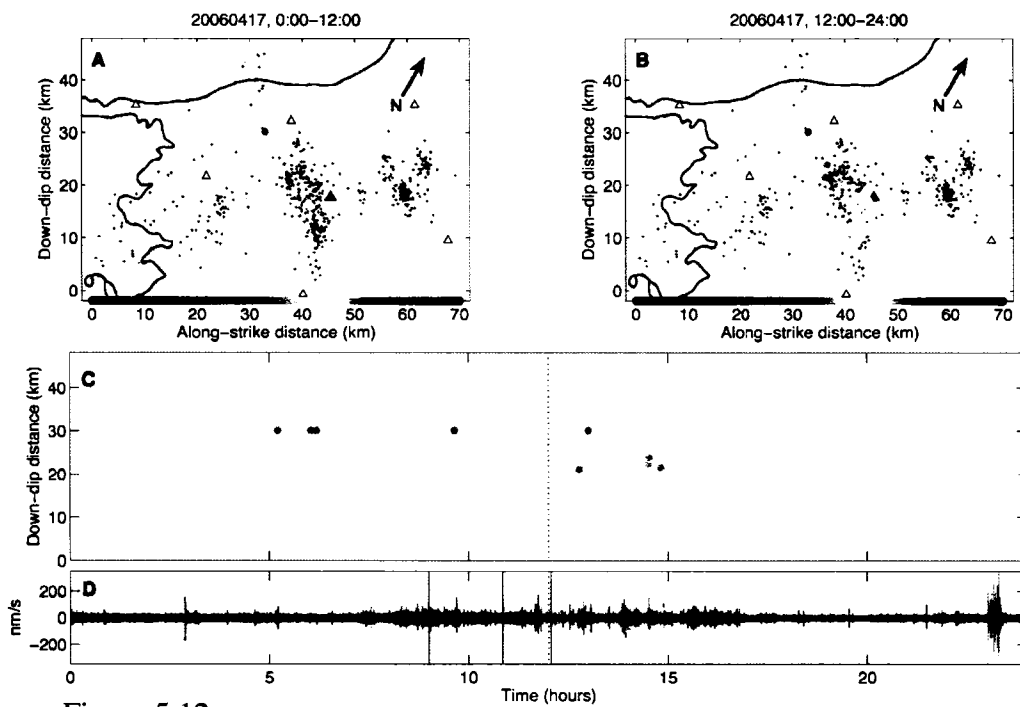


Figure 5.12

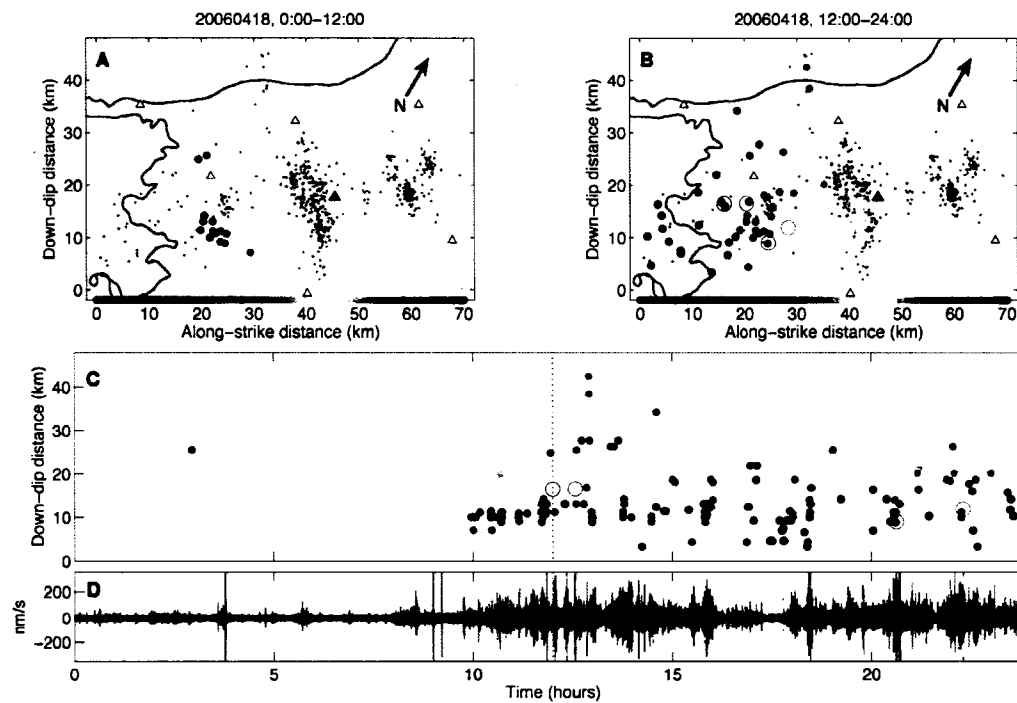


Figure 5.16

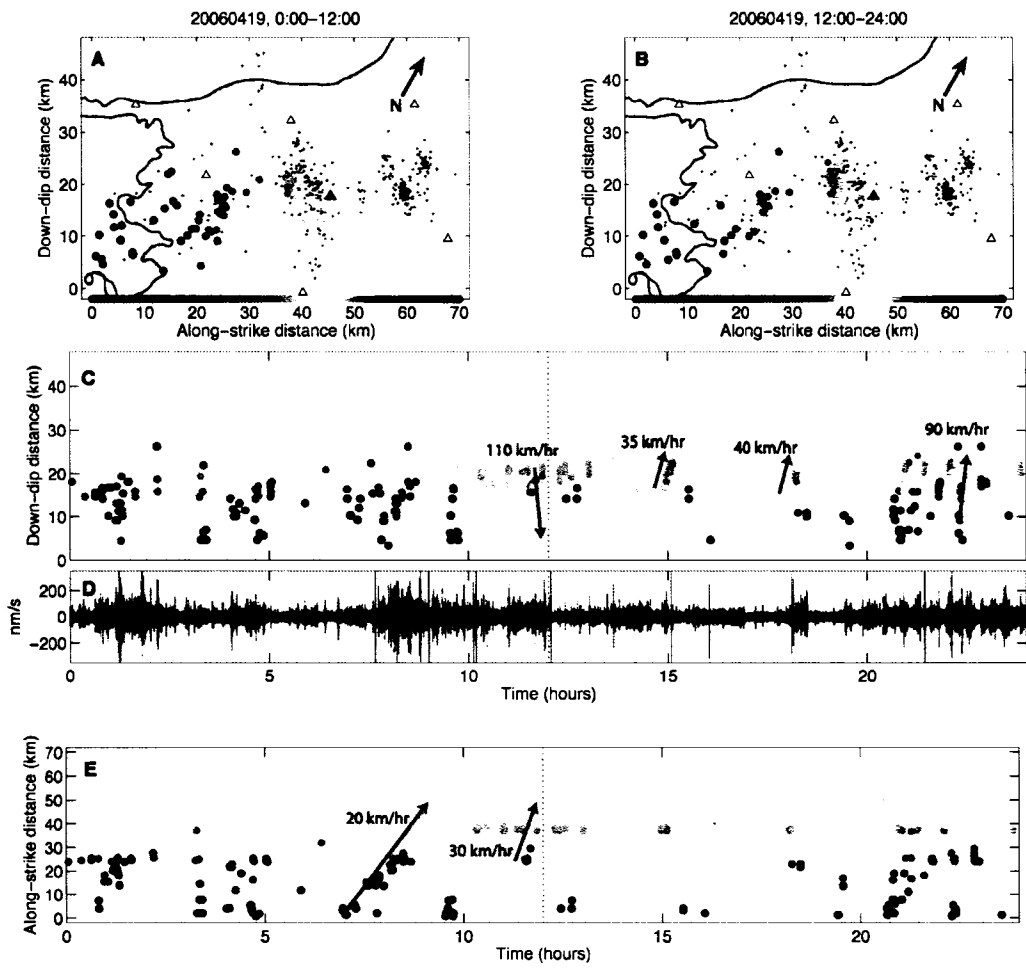


Figure 5.14

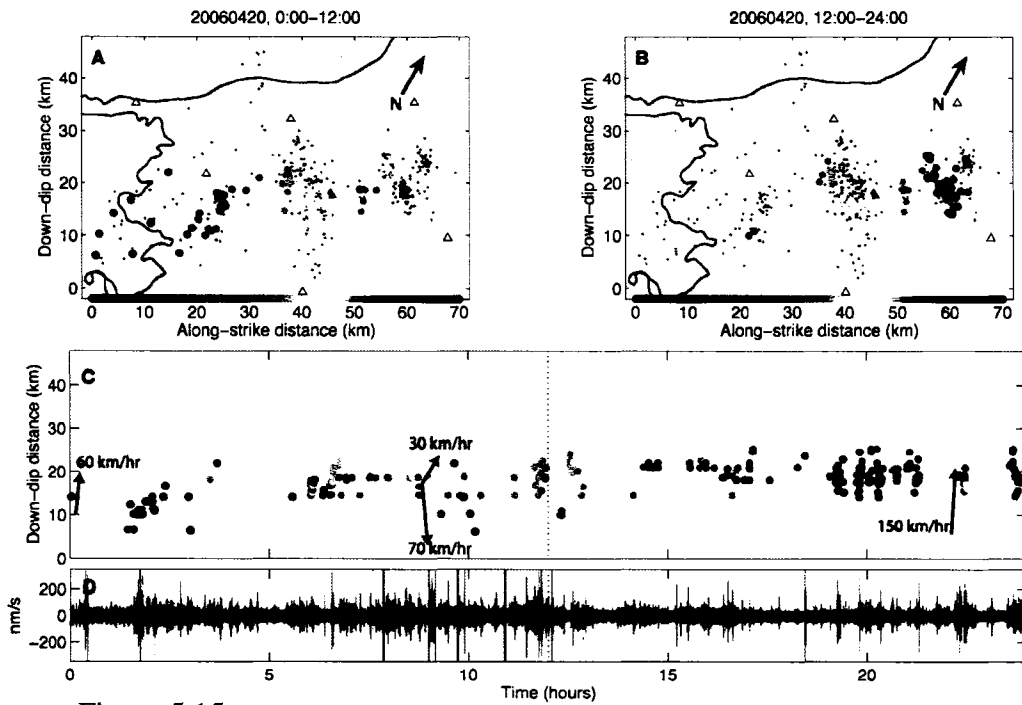


Figure 5.15

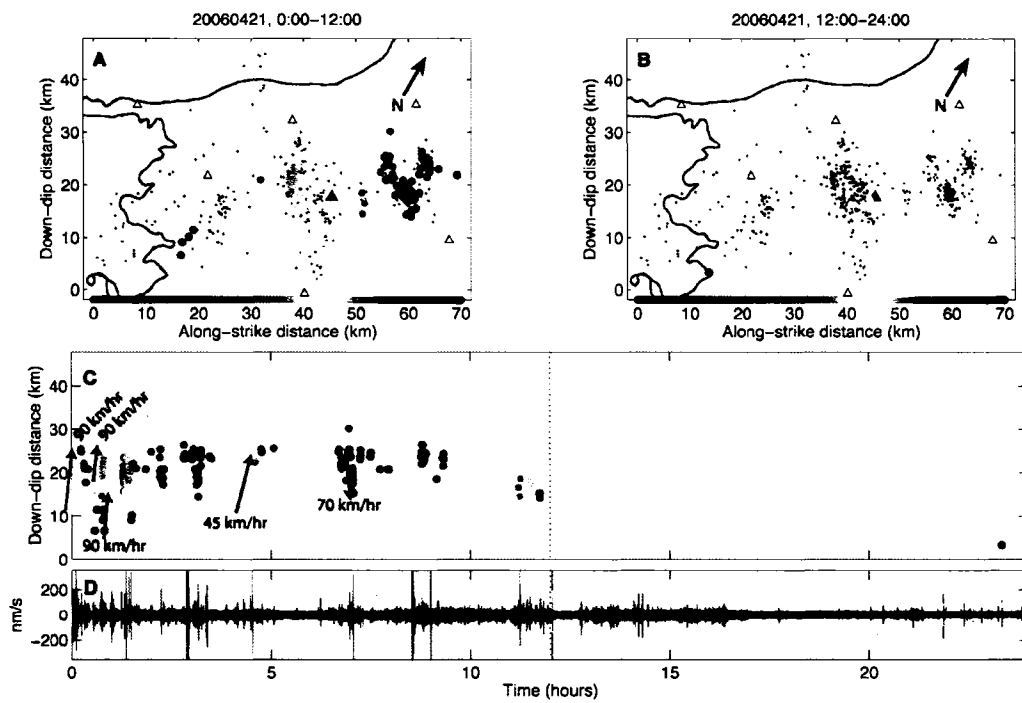


Figure 5.16

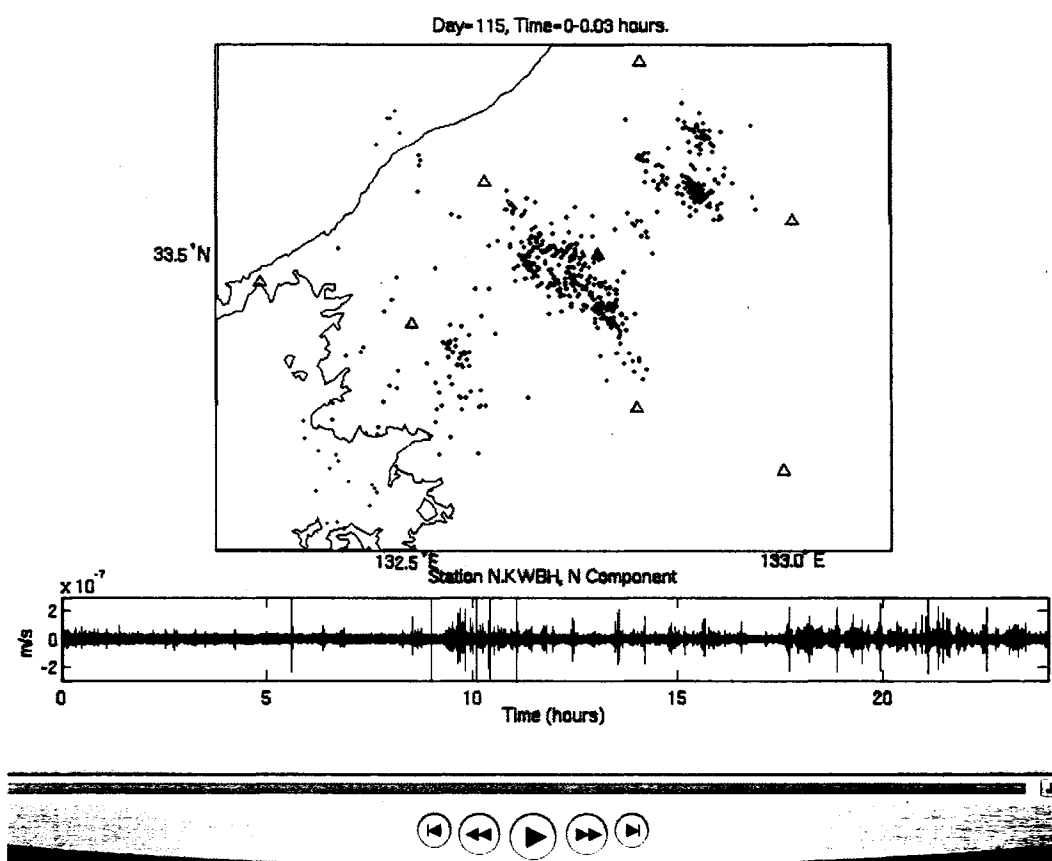


Figure 5.17. Animation showing detected events with time during non-volcanic tremor for 7 days, January 15-21, 2006 (see enclosed CD for movie in Quicktime format). **Top panel:** Map view of western Shikoku region. Template events are plotted as small black crosses. Colored circles represent a detected event, using the normal threshold of 8 times the median absolute deviation of the distribution of correlation sums for each template event. The shade of the circle represents the robustness of the detection, with light orange indicating a detection just above the threshold level and bright red indicating a detection at 2 or more times the threshold. Each frame represents 2 minutes, with strongest detection from each 2-second window plotted. The symbols are plotted in reducing size and shading toward black for 3 frames beyond the detection time in order to guide the eye. Blue triangles show station locations; the filled triangle indicates the station with waveforms plotted in the bottom panel. The time listed at the top corresponds to the approximate time of the first S-wave arrival at any station. **Bottom panel:** A sample velocity waveform, one hour in duration, corresponding to the time-period of the animation. Waveform is station N.KWBH, north component, bandpass filtered between 1 and 8 Hz. Portions plotted in red indicate times with a detected event similar to a template event. The vertical blue bar indicates the point in time represented in the map view.

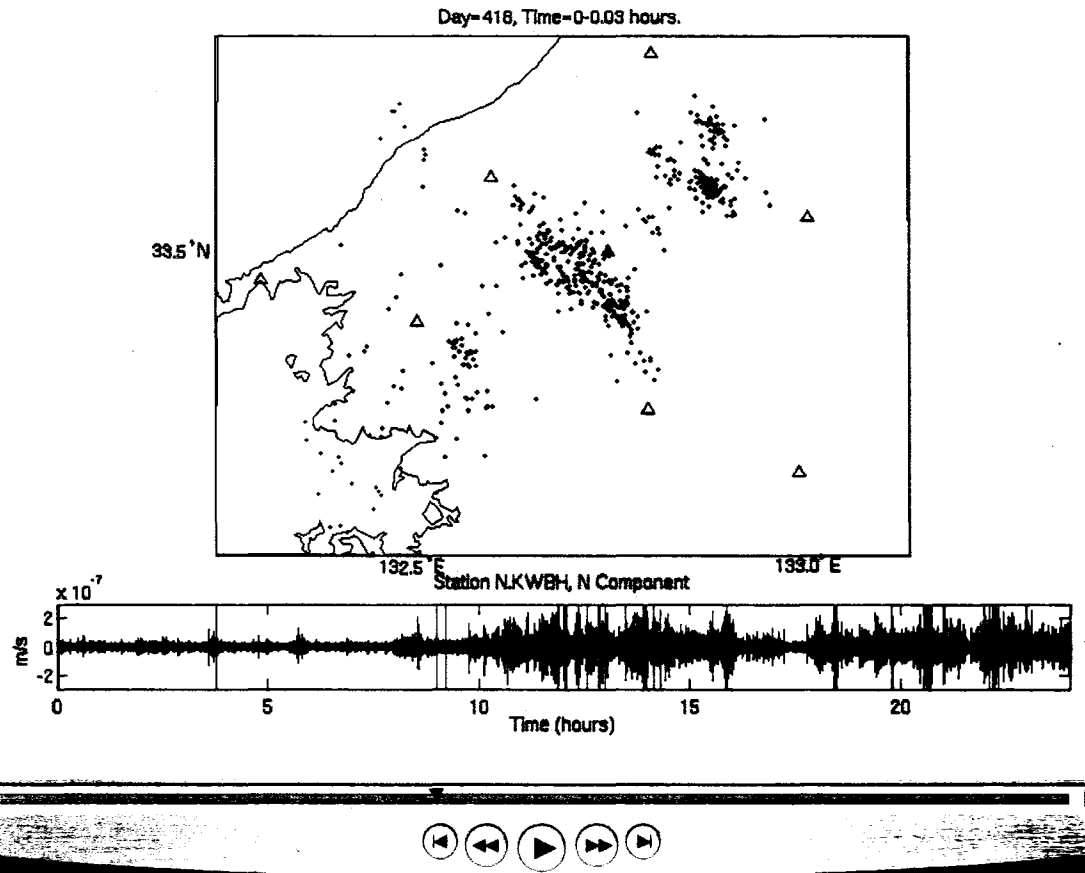


Figure 5.18. Same as Figure 5.17, but for the period from April 15-21, 2006 (see enclosed CD for movie in Quicktime format).

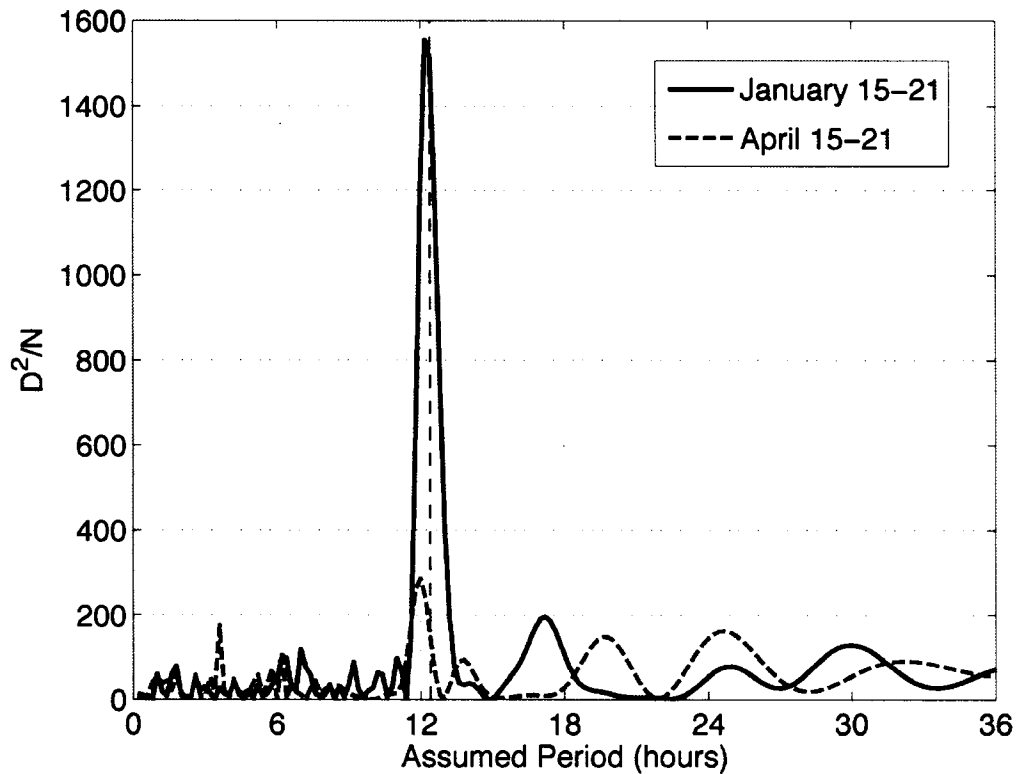


Figure 5.19. Evidence for tidal triggering of LFE activity. The population of detected LFEs during each tremor and slip episode is analyzed for non-randomness at periods from 0.2 to 36 hours. The quantity D^2/N relates to the statistical significance of the non-randomness in Schuster's test (see text). The January event (solid blue line) exhibits an extremely strong periodicity near the average tidal period of 12.4 hours (dashed black line). Tidal triggering in the April event (dashed red line) is less obvious, but this episode still shows a periodicity very close to the average tidal period.

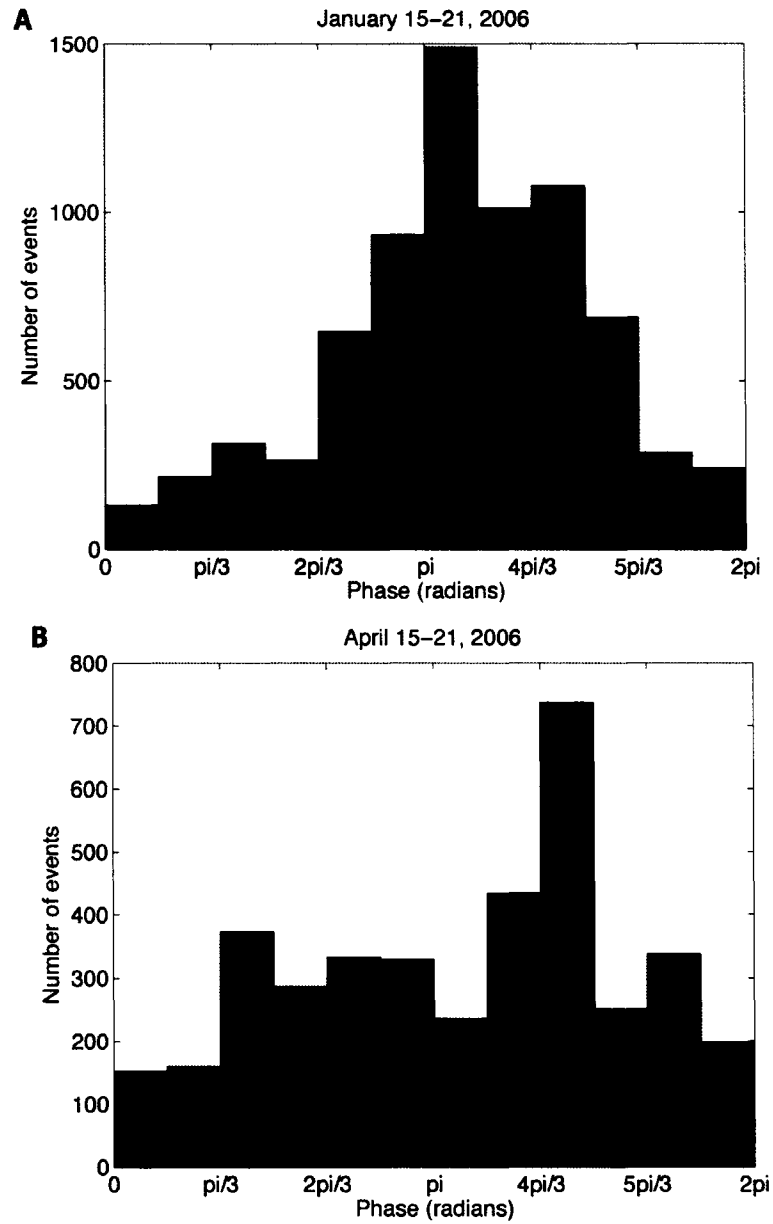


Figure 5.20. Histograms of LFE numbers versus phase angle, assuming a period of 12.4 hours (the average tidal period). (A) January 15-21, 2006. (B) April 15-21, 2006. The phase angle is assigned to be zero at the beginning of each episode (i.e. at 0:00 on January 15 and April 15) and is repeated every 12.4 hours. The January event exhibits a very clear tidal triggering, while the tidal effect in the April event is less obvious.

ACKNOWLEDGEMENTS

This material is based upon work supported by the National Science Foundation grant No. EAR-0409917. All data were obtained from the NIED Hi-net data server. This work utilized the Stanford Center for Computational Earth and Environmental Science.

REFERENCES

- Cochran, E. S., J. E. Vidale, and S. Tanaka (2004). Earth tides can trigger shallow thrust fault earthquakes, *Science*, 306, 1164-1166.
- Dragert, H., K. Wang, and T. S. James (2001), A silent slip event on the deeper Cascadia subduction interface. *Science*, 292, 1525-1528.
- Dragert, H., K. Wang and G. Rogers (2004), Geodetic and seismic signatures of episodic tremor and slip in the northern Cascadia subduction zone, *Earth Planets Space*, 56, 1143-1150.
- Gibbons, S. J. and F. Ringdal (2006), The detection of low magnitude seismic events using array-based waveform correlation. *Geophys. J. Int.* 165, 149-166.
- Hirose, H. and K. Obara (2005), Repeating short- and long-term slow slip events with deep tremor activity, around the Bungo channel region, southwest Japan, *Earth Planets Space*, 57, 961-972.
- Hirose, H., K. Hirahara, F. Kimata, N. Fujii, and S. Miyazaki (1999), A slow thrust slip event following the two 1996 Hyuganada earthquakes beneath the Bungo Channel, southwest Japan. *Geophys. Res. Lett.* 26, 3237-3240.
- Ide, S., D. R. Shelly, and G. C. Beroza (2007a), Mechanism of deep low frequency earthquakes: Further evidence that deep non-volcanic tremor is generated by shear

- slip on the plate interface, *Geophys. Res. Lett.*, 34, L03308, doi:10.1029/2006GL028890.
- Ide, S., G. C. Beroza, D. R. Shelly, and T. Uchide (2007b), A new scaling law for slow earthquakes, *Nature*, submitted.
- Ito Y., K. Obara, K. Shiomi, S. Sekine, and H. Hirose (2007), Slow Earthquakes Coincident with Episodic Tremors and Slow Slip Events, *Science*, 315, 503-506, doi:0.1126/science.1134454.
- Kao, H. et al. (2006), Spatial-temporal patterns of seismic tremors in northern Cascadia. *J. Geophys. Res.*, 111, doi:10.1029/2005JB003727.
- Katsumata, A., and N. Kamaya (2003), Low-frequency continuous tremor around the Moho discontinuity away from volcanoes in the southwest Japan, *Geophys. Res. Lett.* 30, doi:10.1029/2002GL015981.
- Kodaira, S., T. Iidaka, A. Kato, J.-O. Park, T. Iwassaki, and Y. Kaneda (2004), High pore fluid pressure may cause silent slip in the Nankai Trough, *Science*, 304, 1295-1298.
- Liu, Y. and J. R. Rice (2007), Spontaneous and triggered aseismic deformation transients in a subduction fault model, *J. Geophys. Res.*, submitted.
- Liu, Y. and J. R. Rice (2005), Aseismic slip transients emerge spontaneously in three-dimensional rate and state modeling of subduction earthquake sequences, *J. Geophys. Res.*, 110, doi:10.1029/2004JB003424.
- Miyazawa, M. and J. Mori, (2005), Detection of triggered deep low-frequency events from the 20032005 Tokachi-oki earthquake, *Geophys. Res. Lett.*, 32, doi:10.1029/2005GL022539.

- Miyazawa, M. and J. Mori (2006), Evidence suggesting fluid flow beneath Japan due to periodic seismic triggering from the 2004 Sumatra-Andaman earthquake, *Geophys. Res. Lett.*, 33, doi:10.1029/2005GL025087.
- Nadeau, R.M. and T. V. McEvilly (1999), Fault Slip Rates at Depth from Recurrence Intervals of Repeating Microearthquakes, *Science* 285, 718-721, DOI: 10.1126/science.285.5428.718.
- Nakata, R., N. Suda, & H. Tsuruoka (2006), Tidal Synchronicity of the Low-Frequency Tremor in Eastern Shikoku, Japan, *Eos Trans. AGU*, 87(52), Fall Meet. Suppl., Abstract V41A-1700.
- Obara, K. (2002), Nonvolcanic deep tremor associated with subduction in southwest Japan. *Science*, 296, 1679-1681.
- Obara, K., H. Hirose, F. Yamamizu, and K. Kasahara (2004), Episodic slow slip events accompanied by non-volcanic tremors in southwest Japan subduction zone. *Geophys. Res. Lett.* 31, doi:10.1029/2004GL020848.
- Obara, K., Y. Ito, S. Sekine, H. Hirose, & K. Shiomi (2006), Phenomenology of non-volcanic deep tremor, slow slip and the third slow earthquake in southwest Japan subduction zone. *Eos Trans. AGU*, 87(52), Fall Meet. Suppl., Abstract T41A-1532 (2006).
- Ozawa, S., M. Murakami, M. Kaidzu, T Tada, T. Sagiya, Y. Hatanaka, H. Yarai, and T. Nishimura (2002), Detection and monitoring of ongoing aseismic slip in the Tokai region, central Japan, *Science*, 298, 1009-1012.
- Rogers, G. and H. Dragert (2003), Episodic tremor and slip on the Cascadia subduction zone: The chatter of silent slip. *Science*, 300, 1942-1943.
- Rubin, A.M., D. Gillard, & J.-L. Got (1999), Streaks of microearthquakes along creeping faults. *Nature*, 400, 635-641.

- Schaff, D. P., G. C. Beroza, and B. E. Shaw (1998), Postseismic response of repeating aftershocks, *Geophys. Res. Lett.*, *25*, 4549-4552.
- Sekine, S. and K. Obara (2006), A short-term slow slip event with deep low-frequency tremors at western part of Shikoku (April, 2006), *Report of the coordinating committee for earthquake prediction*, *75*, 555-556.
- Seno, T. and T. Yamasaki (2003), Low-frequency tremors, intraslab and interplate earthquakes in Southwest Japan – from a viewpoint of slab dehydration. *Geophys. Res. Lett.* *30*, doi:10.1029/2003GL018349.
- Shelly, D. R., G. C. Beroza, and S. Ide (2007), Non-Volcanic Tremor and Low Frequency Earthquake Swarms, *Nature*, in press.
- Shelly, D. R., G. C. Beroza, S. Ide, and S. Nakamura (2006), Low-frequency earthquakes in Shikoku, Japan and their relationship to episodic tremor and slip. *Nature* *442*, 188-191.
- Shibazaki, B., and Y. Iio (2003), On the physical mechanism of silent slip events along the deeper part of the seismogenic zone, *Geophys. Res. Lett.*, *30*(9), 1489, doi:10.1029/2003GL017047.
- Tanaka, S., M. Ohtake, and H. Sato (2002), Evidence for tidal triggering of earthquakes as revealed from statistical analysis of global data, *J. Geophys. Res.*, *107*(B10), 221, doi:10.1029/2001JB001577.
- Tsuruoka, H., M. Ohtake, and H. Sato (1995), Statistical test of the tidal triggering of earthquakes: contribution of the ocean tide loading effect, *Geophys. J. Int.*, *122*, 183-194.
- Waldhauser, F., W. L. Ellsworth, D. P. Schaff, and A. Cole (2004), Streaks, multiplets, and holes: High-resolution spatio-temporal behavior of Parkfield seismicity. *Geophys. Res. Lett.*, *31*, doi:10.1029/2004GL02069.